

**THERMODYNAMIC PROPERTIES  
OF  
MESOSCOPIC SYSTEMS**

Thesis Submitted for the degree of  
Doctor of Philosophy (Science)  
in  
Physics (Theoretical)  
by  
**SREEMOYEE MUKHERJEE**

Department of Physics  
UNIVERSITY OF CALCUTTA  
2014

## ABSTRACT

In last few decades mesoscopic physics has emerged as an prominent area of research and development. It deals with the interface between the microscopic world of atoms and molecules and the macroscopic bulk samples that are in the thermodynamic limit. Hence it deals with many basic issues like how quantum phenomena evolves into thermodynamic properties. It also promises to give rise to a new generation of electronic devices that work on quantum principles. Although devices working on quantum principles can revolutionize the electronic industry, they have not been achieved yet as it is difficult to control their stability. We show that one can use evanescent modes to build stable quantum switches. The physical properties that make this possible is explained in detail. Demonstrations are given using a multichannel Aharonov-Bohm interferometer. We propose a new  $S$  matrix for multichannel junctions to solve the scattering problem. Quantum tunneling of an electron through a classically forbidden regime has no classical analogue and several aspects of it is still not understood. In another work we analyze a situation where electronic current under the barrier can be measured without disturbing the states under the barrier. For this we consider a multichannel Aharonov-Bohm ring and develop the correct formalism to calculate the currents inside the ring when the states are evanescent. We also show unlike other proposed quantum devices that such currents are not very sensitive to changes in material parameters and environment and thus the system can be used to build stable devices that work on magnetic properties. We start from microscopic approach to many body physics and show the analytical steps and approximations required to arrive at the concept of quantum capacitance. These approximations are valid only in the semi-classical limit and the quantum capacitance in that case is determined by Lindhard function. The effective capacitance is the geometrical capacitance and the quantum capacitance in series, and this too is established starting from a microscopic theory.

The organization of my thesis is as follows. In Chapter 1, we give a brief description of the background of the subject, the brief details of characteristic length scales and the fabrication of mesoscopic samples. There are few prominent mesoscopic effects which are never observed in the bulk. In this chapter we briefly present few of them.

In Chapter 2, we give a brief review of transport formalisms used in mesoscopic systems. First, we give a brief idea of transport regime. In 1957 R. Landauer gave a physical argument for calculating the conductance of a mesoscopic scatterer where leads are accounted for. In quantum waveguide theory section we show explicitly how the leads can act as an electron wave guide. We describe in detail the general

Landauer conductance formula where the conductance is effectively determined by the transmission probabilities of propagating modes. M. Büttiker extended Landauer approach to describe multi-terminal measurements in presence of magnetic field. We describe briefly the Büttiker's formula in next section.

Before going into the core analysis and results of this thesis, it is necessary to mention about the most important basic theory we are using for description of Chapter 5 and Chapter 6, i.e., the Aharonov - Bohm effect. This is the effect in which wavefunctions acquire some additional phase when travelling through space with no electromagnetic fields, but only potentials. In this Chapter 3, we describe in detail the theoretical aspects of Aharonov - Bohm effect in open system and in isolated (or closed) system as well. We have taken a one dimensional ring connected to two electron reservoirs via perfect leads in both sides as an example of open system and give a detail description of Aharonov - Bohm effect in Section 3.1 of this chapter. Again we have taken a one dimensional ring threaded by a magnetic field and the field is confined to the central region of the ring, as an example of an isolated system. Electrons in this ring can support a current around the ring which depends on the magnetic field and cannot decay dissipatively, which is known as persistent current. We give a brief idea of this phenomenon in Section 3.2 of this Chapter 3.

In Chapter 4, we describe quantum capacitance. Starting from microscopic theory to many body physics we show the analytical steps required to arrive at the concept of quantum capacitance. We use some approximations which are valid in the semi-classical limit and derive the quantum capacitance which is determined by Lindhard function. We show in this chapter that our analysis is independent of model in any dimension.

The Chapter 5 describes the possibility of building stable switch based on quantum interference effect. In this chapter we consider a multi-channel Aharonov-Bohm interferometer connected to two electron reservoirs of different chemical potentials to understand the quantum interference effect. We propose a  $S$  matrix for multi-channel junctions to solve the scattering problem and give a detailed theoretical analysis including channel mixing and evanescent modes. We show in this chapter that our work contradicts Landauer's claim that devices based on quantum interference effect cannot be achieved.

In Chapter 6 we describe a situation where electronic current under the barrier can be measured without disturbing the states under the barrier. We develop the correct formalism to calculate the currents inside the ring when the states are evanescent. We discuss various transport phenomena like conductance current, circulating current, persistent current etc as well as thermodynamic property like magnetiza-

tion. We propose that stable devices can be build based on magnetic response using evanescent modes.

In the final chapter (Chapter 7), we draw our conclusions. Thereafter we present our future plans.

*TO MY PARENTS*

# ACKNOWLEDGMENTS

*“If I have seen so far,  
it is only because I have stood on the shoulder of giants.”*

–Issac Newton.

Ph.D. stands for Doctor of Philosophy, but it has meant to me as a process to learn Patience and Persistence, Humbleness and Humility through Devotion and Dedication. Not to mention ruminate metaphysical questions over and over like who I am, where my ways go, and where the truth resides. I admit that I have been extremely blessed to walk this long journey with wonderful, supportive, precious people together. These people have helped in various aspects make this thesis possible. This is the moment I have been dreaming to express my deep gratitude in words to cherish individuals from the bottom of my heart.

First, I am deeply indebted to my research advisor, Professor Prosenjit Singha Deo, for his excellent guidance, caring, patience, and providing me with an excellent atmosphere for doing research. Recently, I realized that to do research is like to plant various seeds. Sometimes, you do know what the fruits or flowers of the seeds you plant are at the very beginning. But sometimes, you plant them since they are seeds and see what the fruits or flowers would be after gardening. From time to time, you thought you know what the seeds are, but they turns out to be different than what you thought. Prof. Deo has been a limitless source of research ideas and has been granting me freedom how to garden seeds of research. His big picture and unique approach of physics have always amazed me, and his tremendous patience and diligence have been exemplifying.

I thank Professor Arup Kumar Raychaudhuri, director, S. N. Bose National Centre for Basic Sciences, Kolkata for providing a vibrant research atmosphere. I express my gratitude to all the deans and registrars who held the chair during this period. I also thank all the academic as well as non-academic staff members of this centre for their assistance and active co-operation. I would likely to thank our librarian and all the members of our library, I would like to thank our system administrator and all the members of computer service cell for their excellent technical support, I thank all the staff members of our centre’s accounts section to handle all accounts related problem and finally, I would like to thank all staff members of our academic programme’s office for efficient handling of all bureaucratic procedures.

My heartiest thanks go to my all friends and colleagues of S. N. Bose National Centre for Basic Sciences whose active support and fruitful help drove my research up to the present mark. We shared very precious moments together and the joys are beyond to express in a few words. The unconditional support and love of my seniors, batch mates and juniors have enriched my last few years of life with good experiences. I particularly mention: Biswajit da (B.D), Kinshuk da, Tamal, Ashutosh, Subhajit, Arghya, Sutapa, Snehasish (sishu), Sankar and Anita. All the unforgettable moments I shared with them will remain cherishable in my memory forever. They have helped me in various occasions both academic and non-academic.

My family is the source of all my strength and inspiration. No words are sufficient to convey my sense of gratitude to my parents. I deeply thank my father (babai), Mr. Kalyan Kumar Mukherjee and my mother (maa), Mrs. Alpana Mukherjee for their unconditional trust, timely encouragement, and endless patience. It was their love that raised me up again when I got weary. My elder brother (dadai), Mr. Samrat Mukherjee has also been generous with his unconditional love and encouragement. He is the person with whom I share the same passion for sports, literature, art, theatre and music. I thank with love to Dr. Abhigyan Sengupta, my caring husband who came forward to share my dreams, and not only insisted but also ensured that I put my research above anything else. He has been my best friend and great companion. His unconditional love, support, encouragement helped me to get through the agonizing period in the most positive way. Together, it has been a wonderful journey all the way. Last but not the least, a very special thanks to my mother-in-law for being so caring and understanding of my study and research. This thesis is for them.

Teachers are next to our parents. I have learnt a lot from them during my entire student life. I am grateful to all my school teachers who arouse my love and interest for learning science, all teachers in Bethune College, Kolkata, Dr. Hrishikesh Chatterjee, professor of Ramkrishna Mission, Narendrapur, Kolkata who gave me the feel and essence of physical chemistry in my college days and finally the faculties of the department of Chemistry, Scottish Church College, Kolkata whose wonderful teaching helped to shape my thoughts and future plans.

I would like to thank Prof. Arun M. Jayannavar for granting me a visit to Institute of Physics, Bhubaneswar in December, 2013. I am deeply indebted to Prof. A. M. Jayannavar for his constant support, guidance, patience and encouragement. I appreciate the opportunity to learn from his expertise and dedication to mesoscopic physics.

I would like to thank Institute of Physics, Bhubaneswar, where I carried out some part of my research work on “Current carried by evanescent modes and possible

device application”, for providing me local hospitality.

Finally, I would like to thank the Department of Sciences and Technology, Government of India (DST-India) and S. N. Bose National Centre for Basic Sciences not only for providing the funding which allowed me to undertake this research, but also for giving me the opportunity to attend conferences and meet so many interesting people. I would like to thank the following organizations/ organizer/ conveners for warm hospitality and pleasant stay during the respective conferences/ workshops etc.:

- (i) The International Conference on Mesoscopic Physics and Spectroscopy, 22nd - 24th Nov, 2010, S. N. Bose National Centre for Basic Sciences, Salt Lake City, Kolkata.
- (ii) The workshop on “Low Dimensional Quantum System”, 10th - 13th Oct, 2011, HarishChandra Research Institute, Allahabad, India.
- (iii) Solid State Physics Symposium (DAE-SSPS), 3rd - 7th Dec, 2012, Indian Institute of Technology - Bombay, India.
- (iv) International workshop on “Nano-Technology and Functional Materials”, 22nd - 24th July, 2013, National Chemical Laboratory - Pune, India.
- (v) National workshop on “Condensed Matter Days” (CMDAYS 2013), 29th Aug - 31st Aug, 2013, NIT- Rourkela, India.

**Sreemoyee Mukherjee**

## **PUBLICATIONS IN REFEREED JOURNAL**

1. **Quantum capacitance: A microscopic derivation**,  
Sreemoyee Mukherjee, Matti Manninen and P. Singha Deo,  
**Physica E.**, **44**, 62-66 (2011).
2. **Stable switch action based on quantum interference effect**,  
Sreemoyee Mukherjee, A. Yadav and P. Singha Deo,  
**Physica E.**, **47**, 86-94 (2013).
3. **Current carried by evanescent modes and possible device applications**,  
Sreemoyee Mukherjee, P. Singha Deo and A. M. Jayannavar, Submitted (2014).

## **PUBLICATION IN PROCEEDING**

1. **Evanescent mode transport and its application to nano-electronics**,  
Sreemoyee Mukherjee and P. Singha Deo,  
**AIP Conference Proceedings**, Vol: **1512**, page: 944-945 (2013).

# Contents

<b>1</b>	<b>INTRODUCTION</b>	<b>3</b>
1.1	Some Basic Concepts . . . . .	5
1.1.1	Characteristic Lengths . . . . .	5
1.1.2	Fabrication of Mesoscopic Samples . . . . .	7
1.2	Prominent Mesoscopic Effects . . . . .	10
1.2.1	Aharonov-Bohm Oscillations in Magnetoresistance . . . . .	10
1.2.2	The Quantized Hall Effect . . . . .	11
1.2.3	Universal Conductance Fluctuations . . . . .	14
1.2.4	Quantized Conductance in Quantum Point Contacts . . . . .	16
1.2.5	Violation of Onsager's Symmetry Relation . . . . .	18
1.2.6	Persistent Current . . . . .	18
<b>2</b>	<b>TRANSPORT FORMALISMS USED IN MESOSCOPIC SYSTEM</b>	<b>21</b>
2.1	Transport regime . . . . .	22
2.2	The Landauer-Büttiker Formalism . . . . .	22
2.2.1	General Landauer Conductance Formula . . . . .	23
2.2.2	Büttiker Formula . . . . .	35
2.3	Summary . . . . .	36
<b>3</b>	<b>AHARONOV - BOHM EFFECT</b>	<b>37</b>
3.1	Aharonov - Bohm Effect in Open One Dimensional Ring . . . . .	38
3.2	Aharonov - Bohm Effect in Closed One Dimensional Ring . . . . .	45
3.3	Summary . . . . .	48
<b>4</b>	<b>QUANTUM CAPACITANCE: A MICROSCOPIC DERIVATION</b>	<b>49</b>
4.1	Introduction . . . . .	49
4.2	Model for Numerical Verification and Illustration . . . . .	51
4.3	Analytical Derivation . . . . .	52
4.4	Conclusion . . . . .	61

<b>5</b>	<b>STABLE SWITCH ACTION BASED ON QUANTUM INTER-FERENCE EFFECT</b>	<b>63</b>
5.1	Introduction . . . . .	64
5.2	Theoretical Analysis . . . . .	65
5.3	Results and Discussions . . . . .	73
5.4	Conclusion . . . . .	83
<b>6</b>	<b>CURRENT CARRIED BY EVANESCENT MODES AND POSSIBLE DEVICE APPLICATIONS</b>	<b>85</b>
6.1	Introduction . . . . .	86
6.2	Theoretical Analysis . . . . .	87
6.3	Results and Discussions . . . . .	97
6.3.1	Conductance of a multi-channel A-B ring . . . . .	97
6.3.2	Circulating current in a multi-channel A-B ring . . . . .	98
6.3.3	Magnetization of a multi-channel A-B ring . . . . .	102
6.4	Conclusions . . . . .	111
<b>7</b>	<b>CONCLUSIONS AND FUTURE PLAN</b>	<b>113</b>
	<b>Bibliography . . . . .</b>	<b>117</b>

# List of Figures

1.1	Zone of macroscopic, mesoscopic and microscopic systems. . . . .	4
1.2	Line-up of conduction and valence band at a junction between an <b>n</b> -type <i>AlGaAs</i> and intrinsic <i>GaAs</i> , (a), (b) before and (c) after charge transfer has taken place. This is a cross-sectional view. Figure taken from [6]. . . . .	8
1.3	Transmission electron micrograph of a ring-shaped resistor made from a 38 nm film of polycrystalline gold. The diameter of the ring is 820 nm and the thickness of the wires is 40 nm. . . . .	9
1.4	Schematic diagram of a circular ring connected to semi-infinite leads. The conductor exhibits periodic oscillations in its conductance as a function of enclosed magnetic flux $\phi$ . . . . .	11
1.5	The Hall effect. A current $I$ flows in a direction orthogonal to crossed electric and magnetic fields. The Hall resistivity is defined as $\rho_{xy} = V/I$ . The conventional resistivity $\rho_{xx}$ can be obtained by measuring the voltage drop along the direction of the current. [16] . . . . .	12
1.6	Quantized Hall effect: Schematic representation of experimental data.	13
1.7	Possible paths of an electron through a disordered wire, with elastic scattering processes at impurities. The interference of such paths is influenced by a magnetic field or the value of the Fermi wave vector, leading to fluctuations of the conductance in the mesoscopic regime. .	15
1.8	QUANTUM POINT CONTACT scheme. . . . .	16
1.9	Schematic representation of experimental data. The conductance through a quantum point contact as a function of the gate voltage. The conductance exhibits clear steps of height $\frac{2e^2}{h}$ (from [24]). . . . .	17

2.1	(a) A conductor having a transmission probability of $T$ is connected two large contacts through two leads (LEAD 1 and LEAD 2). ‘Zero’ temperature is assumed such that the energy distributions of the incident electrons in the two leads can be assumed to be step functions.	
	(b) Dispersion relations $E(k)$ vs. $k$ for the different transverse modes (or subbands) in the leads. Figure is taken from [6]. . . . .	23
2.2	A rectangular conductor assumed to be uniform in the $x$ -direction, extending from $x = -\infty$ to $x = \infty$ and having some transverse confinement potential $V(y)$ . . . . .	25
2.3	Scattering phenomena in three dimension. . . . .	29
2.4	Mesoscopic transport problem in quasi one-dimension. Mesoscopic sample (blue region) connected to two electron reservoirs characterized by chemical potential $\mu_1$ and $\mu_2$ , respectively, by ideal leads (Lead1 and Lead2). A potential difference, $\mu_1 - \mu_2$ , drives a current $I$ through the sample. . . . .	30
2.5	(a) A four-probe arrangement designed to measure the potential drop across a scatterer. (b) If the probes are bent as shown here they could show an apparent negative resistance if $T > 0.5$ . Figure is taken from [6]. . . . .	33
3.1	Schematic diagram of a quantum ring made up of normal metal or semiconductor in one dimension. The ring is attached to perfect leads (quantum wire) in both sides. On the left there is source reservoir having chemical potential greater than the chemical potential of the drain reservoir. Current will flow from source to drain. The wave functions of the electron in different regions have been shown in the figure at their respective places. . . . .	39
3.2	An ideal one dimensional ring of circumference $L$ pierced by magnetic flux $\phi$ . . . . .	45
3.3	Schematic diagram of the electron energy levels as a function of the flux $\phi/\phi_0$ in a one-dimensional ring with and without impurities (solid and dashed curves respectively). Figure is taken from [54]. . . . .	47
4.1	Schematic diagrams of some mesoscopic geometries used in this work as examples and also for numerical verifications. The dot represents sites. Nearest neighbour sites are marked $i$ and $j$ . . . . .	52

- 4.2 A three-dimensional mesoscopic ring pierced by a magnetic flux  $\phi$ . The flux can polarize the ring. The ring can also be polarized by a voltage probe (without making a contact) at site  $r$  at a given voltage  $V$ . Another voltage probe (without making contact) whose voltage is allowed to vary can measure the voltage at the site  $r$ . A solenoid around the ring, as shown in the figure, can measure the induced charge in a segment of the ring due to polarization. The idea of quantum capacitance is valid only when the polarized charge is uniformly distributed in the rest of the ring, apart from the region at  $r$ . . . . . 53
- 4.3 The figure shows that for the geometries shown in Fig. 4.1, the Kohn-Hohenberg theorem is valid. In this figure we have used only Fig. 4.1 (d). It consists of 11 sites ( $N = 11$ ), with 4 spin up electrons and 4 spin down electrons. The on-site Hubbard  $U_1 = 2$ , the nearest neighbour Hubbard  $U_2 = 1$ . The hopping parameter  $t = 1$ . The solid line is the charge on the 6th site as a function of the flux in units of  $Q_0$  which is just electronic charge taken to be 1. The dashed line is  $\frac{\partial E}{\partial V_6}$  in units of  $Z_0 =$  electronic charge taken as 1.  $E$  is the ground state eigen-energy of the many body system found by exact diagonalization using Lanczos algorithm. The dimension of the matrix being of the order  $10^5 \times 10^5$ . Here  $\phi_0 = hc/e$ . . . . . 54
- 4.4 The figure shows that a mesoscopic ring can be polarized by an Aharonov-Bohm flux alone. We have used the geometry of Fig 4.1 (d) here. The graphs for other geometries is qualitatively similar and so not shown here.  $Q_8$  is the charge density at the 8th site, in units of  $Q_0$  which is electronic charge. At zero flux we expect the system to be neutral. As the flux changes, strong dispersion of  $Q_8$  suggests polarization of the system wherein the positive charge in the system can be taken to be uniform and independent of flux. Here  $\phi_0 = hc/e$ . 55
- 4.5 Here we are considering a ring in the semi classical limit. That is the potential in the ring varies very slowly compared to de-Broglie wavelength. In particular we have taken a 11 site ring with a single defect,  $\epsilon_1 = 0.3$  and rest of the site energies are 0. The solid line is  $\frac{\partial Q_1}{\partial V_1}$  and the dashed line is  $-\sum_{j \neq 1} \frac{\partial Q_j}{\partial V_j}$ . Both quantities are in units of electronic charge taken as 1. Here  $U_1 = 2$  and  $U_2 = 1$  with 4 spin up and 4 spin down electrons in the ring. Here  $\phi_0 = hc/e$ . . . . . 58

4.6	The figure shows a plot of $\eta_8 = \partial Q_8 / \partial V_8$ as a function of flux. Here $\eta_8^0 = e/t$ where $e$ is electronic charge. $\phi_0 = hc/e$ . This is for an eleven site disordered ring with site energies varying from $-0.5t$ to $+0.5t$ . In this case $U_1 = 0$ and $U_2 = 0$ . Here $\phi_0 = hc/e$ . . . . .	60
4.7	The figure shows a plot of $\eta_8 = \partial Q_8 / \partial V_8$ as a function of flux. Here $\eta_8^0 = e/t$ where $e$ is electronic charge. $\phi_0 = hc/e$ . This is for an eleven site disordered ring with site energies varying from $-0.5t$ to $+0.5t$ . In this case $U_1 = 2$ and $U_2 = 0$ . Here $\phi_0 = hc/e$ . . . . .	61
5.1	A finite thickness quantum ring of width $a$ made up of normal metal or semiconductor is indicated by the red region. On either sides the quantum ring is attached with quantum wires made up of normal metal or semiconductor (stripped region). On the left of the above system there is the source reservoir and On the right there is the drain reservoir. . . . .	66
5.2	Cylindrical Aharonov-Bohm set up . . . . .	69
5.3	A three-legged two-channel junction that exists at J1 and J2 of Fig. 5.1. . . . .	70
5.4	The figure shows a plot of $\frac{G}{2e^2/h}$ as a function of $\phi/\phi_0$ . Here $\phi_0 = hc/e$ . The incoming electrons have energy $E = \frac{55\hbar^2}{m^*a^2}$ and the constant potential $V_0$ of the ring is 0. We are considering in this case two propagating modes. The solid line is $\sum_{i,j}  t'_{ij} ^2$ for $l_1/a = 5, l_2/a = 5$ and the dashed line is $\sum_{i,j}  t'_{ij} ^2$ for $l_1/a = 4, l_2/a = 6$ . . . . .	74
5.5	We use same parameters as in Fig. 5.4 and plot individual scattering cross sections. (a) shows a plot of $ t'_{11} ^2$ as a function of $\phi/\phi_0$ . (b) shows a plot of $ t'_{12} ^2$ as a function of $\phi/\phi_0$ . $ t'_{21} ^2$ as a function of $\phi/\phi_0$ is identical to $ t'_{12} ^2$ as a function of $\phi/\phi_0$ due to Onsager reciprocity relation, so $ t'_{21} ^2$ is not shown. (c) shows a plot of $ t'_{22} ^2$ as a function of $\phi/\phi_0$ . Here $\phi_0 = hc/e$ . The solid lines are for $l_1/a = 5, l_2/a = 5$ and the dashed lines are for $l_1/a = 4, l_2/a = 6$ . . . . .	75
5.6	The figure shows a plot of $\frac{G}{2e^2/h}$ as a function of $\phi/\phi_0$ . Here $\phi_0 = hc/e$ . The incoming electrons have energy $E = \frac{45\hbar^2}{m^*a^2}$ , the constant potential $V_0$ of the ring is such that $V_0 = \frac{10\hbar^2}{em^*a^2}$ . With this choice $q_1$ is real and $q_2$ is imaginary. Thus, we are considering in this case one propagating mode and one evanescent mode. The solid (black) line is $\frac{G}{2e^2/h}$ for $l_1/a = 5, l_2/a = 5$ and the dashed (red) line is $\frac{G}{2e^2/h}$ for $l_1/a = 3, l_2/a = 7$ . . . . .	76

- 5.7 We use same parameters as in Fig. 5.5 and plot individual scattering cross sections. (a) shows a plot of  $|t'_{11}|^2$  as a function of  $\phi/\phi_0$ . (b) shows a plot of  $|t'_{12}|^2$  as a function of  $\phi/\phi_0$ .  $|t'_{21}|^2$  as a function of  $\phi/\phi_0$  is identical to  $|t'_{12}|^2$  as a function of  $\phi/\phi_0$  due to Onsager reciprocity relation, so  $|t'_{21}|^2$  is not shown. (c) shows a plot of  $|t'_{22}|^2$  as a function of  $\phi/\phi_0$ . Here  $\phi_0 = hc/e$ . The solid (black) lines are for  $l_1/a = 5$ ,  $l_2/a = 5$  and the dashed (red) lines are for  $l_1/a = 3$ ,  $l_2/a = 7$ . . . . . 77
- 5.8 The figure shows a plot of  $\frac{G}{2e^2/h}$  as a function of  $\phi/\phi_0$ . Here  $\phi_0 = hc/e$ . The incoming electrons have energy  $E = \frac{47\hbar^2}{m^*a^2}$ , the constant potential  $V_0$  of the ring is such that  $V_0 = \frac{10\hbar^2}{em^*a^2}$ . With this choice  $q_1$  is real and  $q_2$  is imaginary. Thus, we are considering in this case one propagating mode and one evanescent mode. The solid line is  $\frac{G}{2e^2/h}$  for  $l_1/a = 5$ ,  $l_2/a = 5$  and the dashed (red) line is  $\frac{G}{2e^2/h}$  for  $l_1/a = 4$ ,  $l_2/a = 6$ . . . . . 78
- 5.9 The figure shows a plot of  $\frac{G}{2e^2/h}$  as a function of  $\phi/\phi_0$  for different arm lengths. Here  $\phi_0 = hc/e$ . The incoming electrons have energy  $E = \frac{49\hbar^2}{m^*a^2}$ . The constant potential  $V_0$  of the ring is such that  $V_0 = \frac{40\hbar^2}{em^*a^2}$ . With this choice  $q_1$  and  $q_2$  are both imaginary. Thus, we are considering in this case two evanescent modes. The exact value of  $l_1$  and  $l_2$  are given in the figure inset. For all arm length  $\frac{G}{2e^2/h}$  as a function of  $\phi/\phi_0$  have the same nature. That means switching action is independent of  $l_1 : l_2$ . . . . . 79
- 5.10 We use same parameters as in Fig. 5.9 and plot individual scattering cross sections. (a) shows a plot of  $|t'_{11}|^2$  as a function of  $\phi/\phi_0$ . (b) shows a plot of  $|t'_{12}|^2$  as a function of  $\phi/\phi_0$ .  $|t'_{21}|^2$  as a function of  $\phi/\phi_0$  is identical to  $|t'_{12}|^2$  as a function of  $\phi/\phi_0$  due to Onsager reciprocity relation, so  $|t'_{21}|^2$  is not shown. (c) shows a plot of  $|t'_{22}|^2$  as a function of  $\phi/\phi_0$ . Here  $\phi_0 = hc/e$ . The solid lines are for  $l_1/a = 0.1$ ,  $l_2/a = 0.1$ . 80
- 5.11 The figure shows a plot of  $\frac{G}{2e^2/h}$  as a function of  $\phi/\phi_0$  for different incoming energy. Here  $\phi_0 = hc/e$ . The constant potential  $V_0$  of the ring is such that  $V_0 = \frac{40\hbar^2}{em^*a^2}$ . With this choice  $q_1$  and  $q_2$  are both imaginary. Thus, we are considering in this case two evanescent modes. The solid (black) line is  $\frac{G}{2e^2/h}$  for  $E = \frac{45\hbar^2}{m^*a^2}$ . The dashed (red) line is  $\frac{G}{2e^2/h}$  for  $E = \frac{46\hbar^2}{m^*a^2}$ . The dotted (blue) line is  $\frac{G}{2e^2/h}$  for  $E = \frac{47\hbar^2}{m^*a^2}$ . For all energy values  $\sum_{i,j} |t'_{ij}|^2$  as a function of  $\phi/\phi_0$  have the same nature. That means switching action is independent of incident energy. 81

- 5.12 The figure shows a plot of  $\frac{G}{2e^2/h}$  as a function of  $\phi/\phi_0$  for two choice of total ring lengths. Here  $\phi_0 = hc/e$ . The incoming electrons have energy  $E = \frac{45\hbar^2}{m^*a^2}$ , the constant potential  $V_0$  of the ring is 0. With this choice  $q_1$  and  $q_2$  are both real. Thus, we are considering in this case two propagating modes. The solid line is  $\frac{G}{2e^2/h}$  for  $L/a = 10$  ( $l_1/a = 5$ ,  $l_2/a = 5$ ) and the dashed line is  $\frac{G}{2e^2/h}$  for  $L/a = 8$  ( $l_1/a = 4$ ,  $l_2/a = 4$ ). 82
- 5.13 The figure shows a plot of  $\frac{G}{2e^2/h}$  as a function of  $\phi/\phi_0$ . Here  $\phi_0 = hc/e$ . The incoming electrons have energy  $E = \frac{45\hbar^2}{m^*a^2}$ , the constant potential  $V_0$  of the ring is such that  $V_0 = \frac{40\hbar^2}{em^*a^2}$ . With this choice  $q_1$  and  $q_2$  are both imaginary. Thus, we are considering in this case two evanescent modes. The solid line is  $\frac{G}{2e^2/h}$  for  $L/a = 0.2$  ( $l_1/a = 0.1$ ,  $l_2/a = 0.1$ ) and the dashed line is  $\frac{G}{2e^2/h}$  for  $L/a = 0.16$  ( $l_1/a = 0.08$ ,  $l_2/a = 0.08$ ). 83
- 6.1 A finite thickness quantum ring of width  $a$  made up of normal metal or semiconductor is indicated by the blue region. On either sides the quantum ring is attached with quantum wires made up of normal metal or semiconductor (stripped region). On the left of the above system there is the source reservoir and On the right there is the drain reservoir. . . . . 88
- 6.2 Top: Another schematic diagram of mesoscopic interferometer coupled to the left and right electron reservoirs. Electrostatic potential is zero everywhere. Bottom: Energy level dispersion curve for each region. Dispersion relation,  $E(k_n)$  vs.  $k_n$  obtained from Eq. (6.8) for propagating modes in regions I and IV, indicated by solid lines. Dispersion relation,  $E(q_n)$  vs.  $q_n$  obtained from Eq. (6.27) and Eq. (6.28) for evanescent modes in regions II and III, indicated by dash-dotted lines. . . . . 93
- 6.3 Cylindrical Aharonov-Bohm set up . . . . . 94
- 6.4 The figure shows plot of conductance,  $G/\frac{2e^2}{h}$  as a function of  $\phi/\phi_0$  using evanescent modes for different arm lengths. Total ring length is the same in all cases. Here  $\phi_0 = hc/e$ . The energy of incident electrons,  $E = \frac{49\hbar^2}{m^*a^2}$ . The exact values of  $l_U$  and  $l_L$  are given in the figure inset. For all sets of arm lengths  $G/\frac{2e^2}{h}$  as a function of  $\phi/\phi_0$  have the same nature. . . . . 98

6.5	The figure shows plot of circulating current ( $I_c$ ) in the dimensionless units as a function of incident Fermi energy (solid curve) and transmission coefficient ( $\sum_{i,j}  t_j^{(i)} ^2$ ) as a function of incident Fermi energy (dashed curve) using two propagating modes. Here upper arm length, $l_U/a = 3$ and lower arm length, $l_L/a = 7$ . . . . .	100
6.6	The figure shows plot of circulating current ( $I_c$ ) in dimensionless unit as a function of incident Fermi energy (solid curve) and transmission coefficient ( $\sum_{i,j}  t_j^{(i)} ^2$ ) as a function of Fermi energy of incident electrons (dashed curve) using one propagating mode and one evanescent mode. Here upper arm length is $l_U/a = 3$ and lower arm length is $l_L/a = 7$ . . . . .	101
6.7	The figure shows plot of magnetization strength in dimensionless unit as a function of Fermi energy using two propagating modes. Here upper arm length, $l_U/a = 3$ and lower arm length, $l_L/a = 7$ . . . . .	102
6.8	The figures (a) - (c) show plot of magnetization strength in dimensionless unit as a function of $\phi/\phi_0$ for different choice of parameters. Here $\phi_0 = hc/e$ . The constant potential $V_0$ is taken as 0, so that both the modes are propagating. . . . .	104
6.9	The figures (a) - (c) show plot of magnetization strength in dimensionless unit as a function of $\phi/\phi_0$ . The constant potential $V_0$ of the ring is such that $V_0 = 10\hbar^2/em^*a^2$ . With this choice $q_1$ is real and $q_2$ is imaginary. Thus we are considering in this case one propagating mode and one evanescent mode. . . . .	105
6.10	The figures (a) - (c) show plots of magnetization strength as a function of $\phi/\phi_0$ for an Aharonov-Bohm interferometer where all the current carrying modes are evanescent. Here $\phi_0 = hc/e$ . . . . .	107
6.11	The figures (a) - (b) show plot of magnetization strength as a function of $\phi/\phi_0$ for an Aharonov-Bohm interferometer where all the current carrying modes are evanescent. Here $\phi_0 = hc/e$ . In (a), the incoming electrons have energy $E = \frac{45\hbar^2}{m^*a^2}$ . The solid line is for $L/a = 0.24$ and the dashed line is for $l_U/a = 0.11, l_L/a = 0.09$ . In (b), the incoming electrons have energy $E = \frac{47\hbar^2}{m^*a^2}$ . The solid line is for $L/a = 0.22$ and the dashed line is for $l_U/a = 0.13, l_L/a = 0.12$ . Here (a) and (b) shows that plots are independent of material parameters. . . . .	108
6.12	The figures (a) - (b) show plots of transport current $I_{U/L}^{even}$ in dimensionless unit as a function of $\phi/\phi_0$ for different arm lengths keeping the ring length same. . . . .	109

- 6.13 The figure shows plot of  $m^*I_{U/L}^{max}/e\hbar$  obtained at  $\phi/\phi_0 = 6.2$  (see Fig. 6.12) as a function of upper arm length ( $l_U/a$ ) of the quantum ring. The solid line indicates  $m^*I_U^{max}/e\hbar$  as a function of  $l_U/a$  and the dashed line indicates  $m^*I_L^{max}/e\hbar$  as a function of  $l_U/a$ . . . . . 110
- 6.14 The figures (a) - (b) show plot of persistent current in dimensionless unit as a function of  $\phi/\phi_0$  for different arm lengths keeping the ring length same. In (a) and (b), we have used the same convention and same parameters as in Fig. 6.12 (a) and (b), respectively. . . . . 111



# Chapter 1

## INTRODUCTION

*“Around here, however, we don’t  
look backwards for very long.  
We keep moving forward,  
opening new doors  
and doing new things,  
because we’re curious,  
and curiosity keeps  
leading us down new paths.”*  
– Walt Disney.

R. P. Feynman discussed, predicted and challenged the future generation scientists: *“Why cannot we write the entire 24 volumes of the Encyclopaedia Britannica on the head of a pin?”* or *“The entire contents of the library of congress in the volume of a sugar cube?”* in his seminal lecture entitled by *“There is plenty of room at the bottom”* on 29th December, 1959 at the annual meeting of the American Physical Society at the California Institute of Technology [1]. In 1947, with the invention of world’s first transistor [2], a trend towards miniaturization started. In the last five decades there has been tremendous progress made in the development of technologies for reaching the physical limits of miniaturization, in order to satisfy increasing industrial demands. Requirements for lower power consumption, occupying less space, containing more information and faster processing speeds of electronic devices has imposed the necessity for smaller dimension and has led to a rapid development of manufacturing technologies. Since the 1960’s, the number of transistors per unit area has been doubling every 18 months. This fantastic progression of circuit fabrication is known as Moore’s law [3, 4], after Intel co-founder Gordon E. Moore. If the size of integrated circuit chips stay approximately the same, then the linear dimension of the transistors will half every four years. Current transistor fabrica-

tion already runs at 22 nm, and Intel claim that they will have 5 nm technology in commercial devices by 2020. Today, this critical dimension is reached in commercial microprocessors fabrication using optical lithographic techniques. This limit can be reduced to a few nanometers by use of electron beam lithography (EBL), electrochemical methods, etching techniques, etc. These techniques have opened another field of solid state science, namely mesoscopic physics.

Meso means *middle* or *intermediate* in Greek. In 1976 N. G. van Kampen first coined the term mesoscopic systems in the context of statistical physics [5], and similar usages have come to appear more often in diverse fields since early 1990s with the advent of micro-fabrication processing techniques, referring to small samples whose dimension lies in between microscopic and macroscopic counterparts. They are much larger than microscopic objects like atoms, but not large enough to be described by text book condensed matter physics or statistical mechanics. For example a conductor usually shows ohmic behavior if its dimensions are much larger than each of the three characteristic length scales:

- (i) the de Broglie wave length, which is related to the kinetic energy of the electrons,
- (ii) the mean free path which is the distance that an electron travels before its initial momentum gets destroyed and
- (iii) the phase-relaxation length, which is the distance that an electron travels before its initial phase is destroyed.

These length scales vary widely from one material to another and are strongly affected by temperature, magnetic field etc. If sample (conductor) dimension becomes comparable to these length scales then Ohmic behavior breaks down. Fig. 1.1

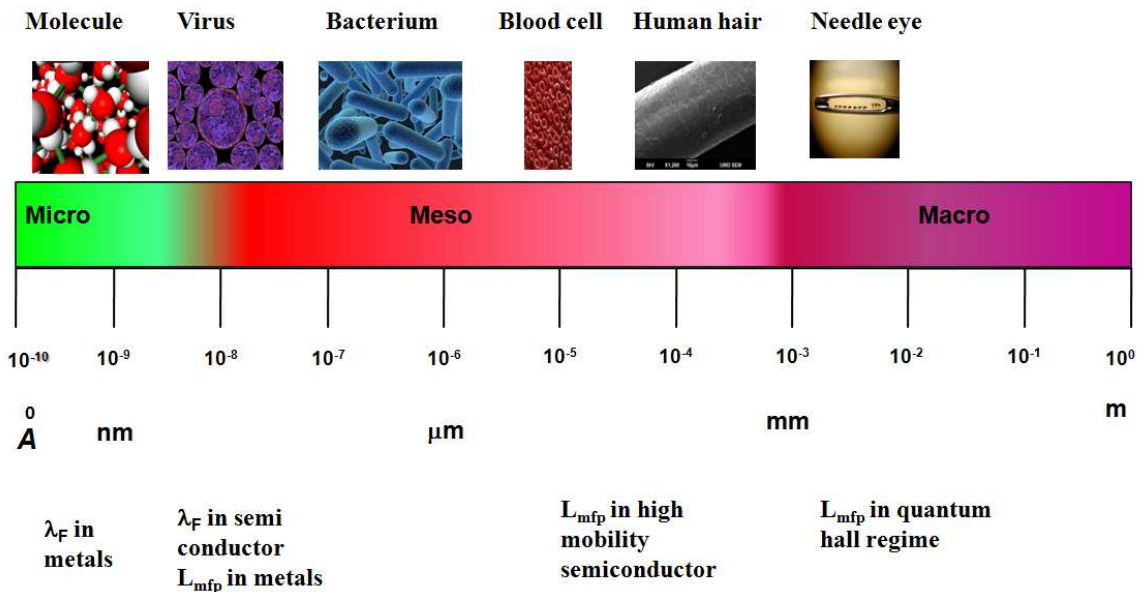


Figure 1.1: Zone of macroscopic, mesoscopic and microscopic systems.

presents three regions of systems along the length scale bar with familiar objects corresponding the size of physical length. Macroscopic ones are often what our bare eyes can see, typically bigger than millimeters, whereas microscopic systems are too tiny to understand. Mesoscopic world closes the gap between the two regions, spanning from millimeters to nanometers (a billionth of a millimeter).

## 1.1 Some Basic Concepts

### 1.1.1 Characteristic Lengths

In this section different characteristic lengths like de Broglie wave length, mean free path, phase relaxation length, magnetic length and thermal length have been described at which mesoscopic effects appear. These length scales have the following physical meaning:

- (i) **de Broglie wave length,  $\lambda_F$** : This length is defined as

$$\lambda_F = 2\pi\hbar/p(k) = 2\pi/k$$

where  $p(k)$  is the typical electron momentum (wave vector). For Fermi gas the characteristic momentum is just the Fermi momentum. For the case of a single filled band in two dimensional electron gas (2-DEG),

$$\lambda_F = 2\pi/k_F = \sqrt{2\pi/n_s}$$

where  $n_s$  is the electron density. For the Boltzmann gas,  $p \approx \sqrt{2mkT}$ , and

$$\lambda_F = 2\pi\hbar/\sqrt{2mkT}.$$

For an electron density of  $5 \times 10^{11}/\text{cm}^2$ , the Fermi wavelength is about 35 nm. At low temperatures the current is carried mainly by electrons having an energy close to the Fermi energy so that the Fermi wavelength is the relevant length. Other electrons with less kinetic energy have longer wavelengths but they do not contribute to the conductance [6]. When the sample dimension becomes comparable to  $\lambda_F$  then quantum effects become predominant and Schrödinger equation becomes the guiding equation of motion for particle dynamics.

- (ii) **Mean free path,  $L_m$** : An electron in a perfect crystal moves as if it were in vacuum but with a different mass. Any deviation from perfect crystallinity such as impurities, lattice vibrations or presence of other electrons lead to ‘collisions’ that scatter the electron from one state to another thereby changing

its momentum. The momentum relaxation time  $\tau_m$  is related to the collision time  $\tau_c$  by a relation of the form

$$\frac{1}{\tau_m} \rightarrow \frac{1}{\tau_c} \alpha_m$$

where the factor  $\alpha_m$  (lying between 0 and 1) denotes the effectiveness of an individual collision in destroying momentum, e.g., if the collisions are such that the electrons are scattered only by a small angle then very little momentum is lost in an individual collision. The factor  $\alpha_m$  is then very small so that the momentum relaxation time is much longer than the collision time.

The mean free path,  $L_m$ , is the distance that an electron travels before its initial momentum is destroyed; i.e.,

$$L_m = \nu_f \tau_m$$

where  $\tau_m$  is the momentum relaxation time and  $\nu_f$  is the Fermi velocity. The Fermi velocity is given by

$$\nu_f = \frac{\hbar k_f}{m} = \frac{\hbar}{m} \sqrt{2\pi n_s} \rightarrow 3 \times 10^7 \text{ cm/s}$$

if  $n_s = 5 \times 10^{11} / \text{cm}^2$ . Assuming a momentum relaxation time of 100 ps we obtain a mean free path of  $L_m = 30 \mu\text{m}$ . When the sample dimension becomes comparable to  $L_m$  then one has to abandon the usual notions of canonical and grand canonical ensembles and carefully develop a new approach for mesoscopic system.

- (iii) **Phase relaxation length,  $L_\phi$ :** The phase relaxation length is the average distance that an electron travels before it experiences inelastic scattering which destroys its initial coherent state. Typical scattering events, such as electron-phonon or electron-electron collisions, change the energy of the electron and randomize its quantum-mechanical phase. Impurity scattering may also contribute to phase relaxation if the impurity has an internal degree of freedom so that it can change its state. For example, magnetic impurities have an internal spin that fluctuates with time. In high-mobility degenerate semiconductors, phase relaxation often occurs on a time-scale  $\tau_\phi$  which is of the same order or shorter than the momentum relaxation time  $\tau_m$ . We will discuss phase-relaxation time ( $\tau_\phi$ ) as follows

$$\frac{1}{\tau_\phi} \rightarrow \frac{1}{\tau_c} \alpha_\phi$$

where the factor  $\alpha_\phi$  denotes the effectiveness of an individual collision in destroying phase. We can obtain phase-relaxation length by multiplying the Fermi velocity with the phase relaxation time:

$$L_\phi = v_f \tau_\phi.$$

In low-mobility semiconductors the momentum-relaxation time  $\tau_m$  can be considerably shorter than the phase relaxation time  $\tau_\phi$  and diffusive motion may occur over a phase coherent region; then  $L_\phi^2 = D\tau_\phi$  with a diffusion constant  $D = v_F^2 \tau_m / 2$ . When the sample dimension becomes comparable to  $L_\phi$  then interference effect has to be properly understood and accounted for.

- (iv) **Magnetic length:** In the presence of a magnetic field (inductance  $B$ ) the electron energy is quantized in Landau levels  $E_N = (N + \frac{1}{2})\hbar\omega_c$  where  $\omega_c = eB/m^*$  is the cyclotron frequency. The magnetic length  $L_B = (\hbar/eB)^{1/2}$  characterizes the extension of the cyclotron orbit. The importance of the magnetic length lies in the fact that it can be tuned over a large range by changing the magnetic field. Thus, a magnetic field provides additional means of reducing the effective dimensionality of the system [7].
- (v) **Thermal length:** The thermal length  $L_T = \hbar v_F / (k_B T)$  is connected with the average excess energy of thermal electrons  $k_B T$ . The phase of an electron which travels at the Fermi velocity is undetermined within  $L_T$ , due to thermal fluctuations of the electron energy [7].

## 1.1.2 Fabrication of Mesoscopic Samples

### Semi-conducting sample fabrication

Advances in electron beam lithography within the last few years have made it possible to fabricate nano sized or mesoscopic artificial structures with good control over design parameters and probe the quantum transport properties [6]. These include very narrow quasi one-dimensional quantum wires, zero-dimensional electron quantum systems or quantum dots, rings etc., constructed at semiconductor interface. Typical sizes of these systems vary between 1 to 10  $\mu\text{m}$ . Recent work on mesoscopic conductors has largely been based on GaAs-AlGaAs heterojunctions where a thin two-dimensional conducting layer is formed at the interface between GaAs and AlGaAs. The generic semiconductor structures used to obtain a two dimensional electron gas (2-DEG) which is shown in Fig. 1.2.

The conduction and valence band line-up in the  $z$ -direction when we first bring the layers in contact (Fig. 1.2 (a)). The Fermi energy  $E_f$  in the wide gap AlGaAs layer is higher than that in the narrow gap GaAs layer (Fig. 1.2 (b)). Consequently

electrons spill over from the n-AlGaAs leaving behind positively charged donors. This space charge gives rise to an electrostatic potential that causes the band to bend as shown in Fig. 1.2 (c). At equilibrium the Fermi energy is constant ev-

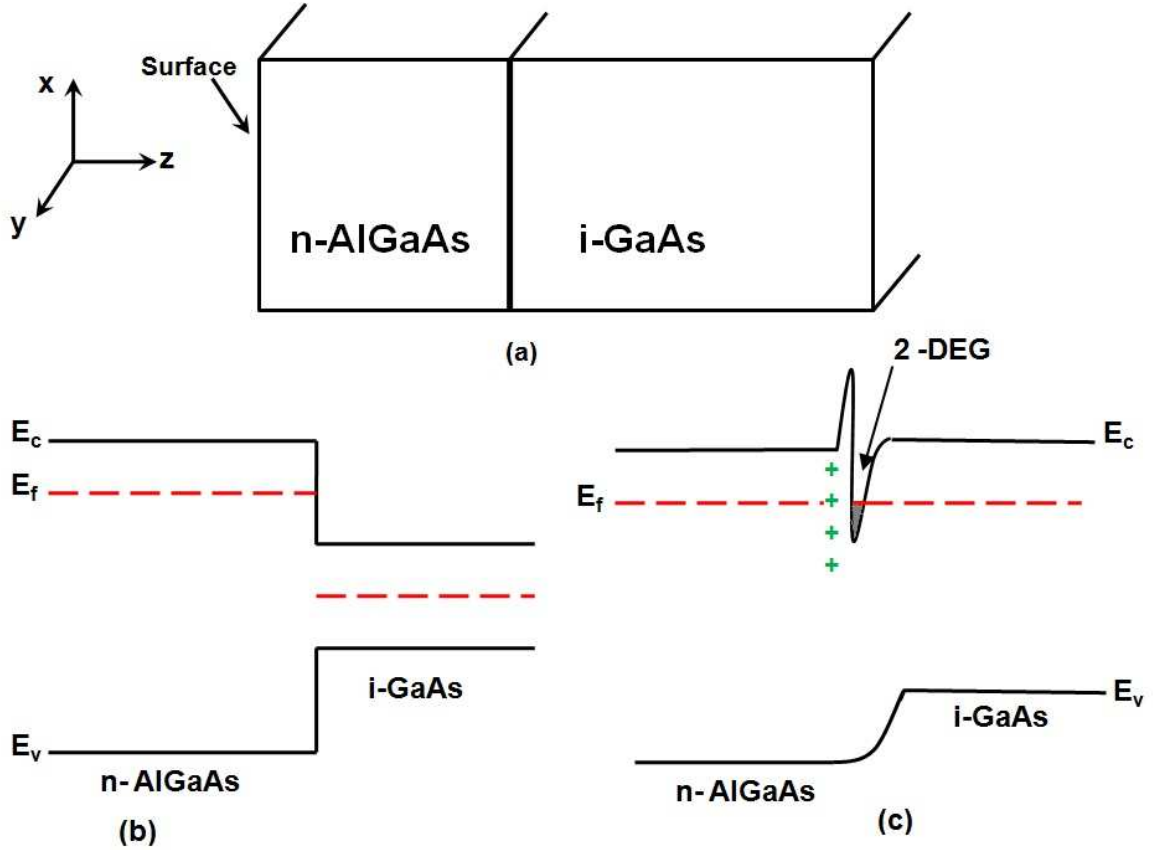


Figure 1.2: Line-up of conduction and valence band at a junction between an **n**-type *AlGaAs* and intrinsic *GaAs*, (a), (b) before and (c) after charge transfer has taken place. This is a cross-sectional view. Figure taken from [6].

erywhere. The electron density is sharply peaked near the GaAs-AlGaAs interface (shaded region in Fig. 1.2 (c)) forming a thin conducting layer which is usually referred to as the two dimensional electron gas (2-DEG). The carrier concentration in a 2-DEG typically ranges from  $2 \times 10^{11}/cm^2$  to  $2 \times 10^{12}/cm^2$  and can be depleted by applying a negative voltage to a metallic gate deposited on the surface. The practical importance of this structure lies in its use as a field effect transistor (FET) [8, 9], etc. There are various types of FETs (which are distinguished by the method of insulation between channel and gate) under a variety of names such as MODulation Doped Field Effect Transistor (MODFET), Metal Oxide Semiconductor Field Effect Transistor (MOSFET), High Electron Mobility transistor (HEMT) etc. This structure is similar to standard silicon MOSFETs, where the 2-DEG is formed in silicon instead of GaAs-AlGaAs interface. The role of the wide-gap AlGaAs is played by

a thermally grown oxide layer ( $SiO_x$ ). Indeed much of the pioneering work on the properties of two-dimensional conductors was performed using silicon MOSFETs [10]

### Metal film fabrication

Similarly immense interest in mesoscopic physics was motivated by novel developments in metal film fabrication techniques. Consider, e.g., the conductance of a rectangular conductor is directly proportional to its width ( $W$ ) and inversely proportional to its length ( $L$ ), i.e.,  $G = \frac{\sigma W}{L}$ , where  $\sigma$  is the conductivity of the material independent of its dimensions. The ring shaped resistor made up of polycrystalline

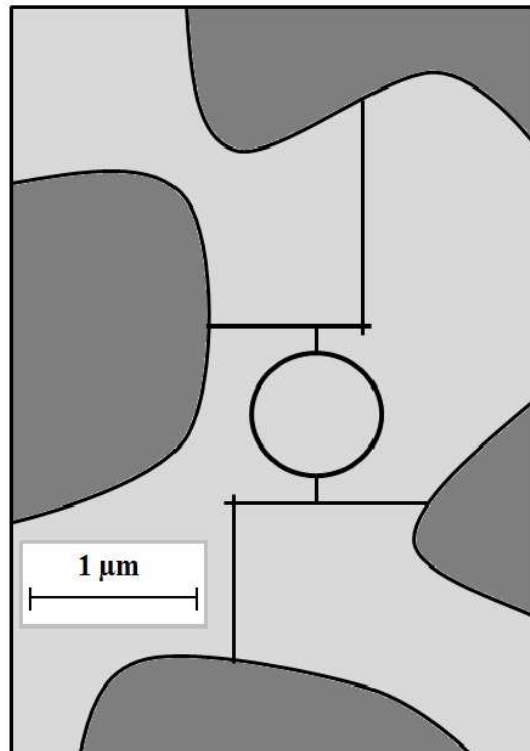


Figure 1.3: Transmission electron micrograph of a ring-shaped resistor made from a 38 nm film of polycrystalline gold. The diameter of the ring is 820 nm and the thickness of the wires is 40 nm. This structure is redrawn by me from the original work of S. Washburn and R. A. Webb (1986) *Adv. Phys.* **35**, 375. The structures were fabricated by C. Umbach of IBM.

gold described in Fig. 1.3 was used for one of the landmark experiments in mesoscopic physics [11] : the resistance of the ring was shown to oscillate as the magnetic field through it was changed because the magnetic field modified the interference between the electron waves traversing the the two arms of the ring. The devices were fabricated on  $Si_3N_4$  windows which are 100nm thick. A metal film was deposited onto the wafer, the metal was gold ( $Au$ ) or some material to resist oxidation. The

film was coated with resist, and islands of resists were curved with conventional electron-beam lithography to define contact pads. The resist was dissolved away leaving the pad areas covered, and the wafer was diced into individual devices. The individual chips were installed into a high resolution scanning transmission electron microscope (STEM), and the device was drawn by rastering the STEM beam back and forth in the desired pattern.

## 1.2 Prominent Mesoscopic Effects

Mesoscopic systems reveal a number of interesting physical phenomena, never observed in the bulk. In this section, we briefly present a selection of the most important effects arising as a consequence of the quantum phase coherence of the electronic wave functions in the mesoscopic regime. Many of the most significant effects appear in samples of reduced dimension like two-dimensional electron gases in semiconductor heterostructures, one-dimensional systems (so-called quantum wires) and structures in which electrons are completely confined, the so-called quantum dots. Some conceptually important mesoscopic phenomena are the Aharonov-Bohm oscillations in magnetoresistance, integer and fractional quantum Hall effect, universal conductance fluctuations, quantized conductance in quantum point contacts and persistent current which we will discuss in next subsections.

### 1.2.1 Aharonov-Bohm Oscillations in Magnetoresistance

Aharonov and Bohm first proposed an experiment in 1959 that there exists effects of potentials on charged particle even in the region where all the fields, viz., electric and magnetic fields vanishes [12, 13]. This effect is named after Yakir Aharonov and David Bohm. Fig. 1.4 is a schematic description of an experimental set-up, suited for verifying the prediction of Aharonov and Bohm. In a metallic ring small enough that the circumference of the ring is smaller than the phase coherence length, an interference pattern should be present in the magnetoresistance of the device [14]. One of the pioneering experiments in mesoscopic physics was performed by Washburn et al. using a small ring, 820 nm in diameter, etched out a high quality gold film. They observed that the conductance of normal metal ring oscillates as a function of magnetic flux enclosed by the ring. The fundamental period of the oscillations is found out to be flux quantum,  $\phi_0 = \frac{hc}{e}$ . Classically no such oscillations can occur. This is because the quantum phase memory of the electron is randomized during a travel around the whole circumference. A quantum wave associated to such an electron separates into two partial waves at the entrance of the ring and recombine at the exit point. These electron waves moving along fixed paths acquire a phase difference because of monotonically changing magnetic field. The interference between these

two partial waves traversing two arms of the ring leads to this oscillatory behavior of the conductance.

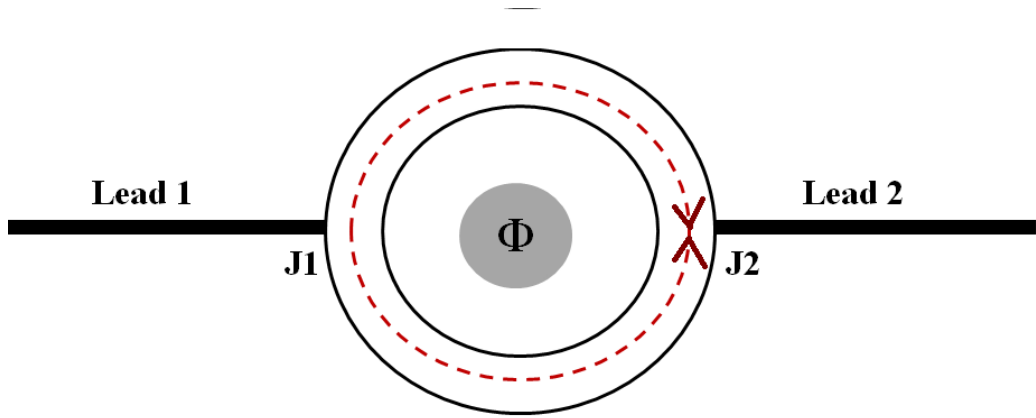


Figure 1.4: Schematic diagram of a circular ring connected to semi-infinite leads. The conductor exhibits periodic oscillations in its conductance as a function of enclosed magnetic flux  $\phi$ .

However, Aharonov-Bohm effect observed in mesoscopic rings is quite different from this simplistic view. Complications arise due to non-locality and multiple reflections at J1 and J2 because of which we cannot interpret the experimental results as an interference between waves traversing the two arms. A detailed description of this both in open system and in closed system in one-dimension is given in Chapter 3: “Aharonov - Bohm Effect”. This approach is followed when we deal with the realistic quasi one-dimensional rings, multi-channel rings in Chapter 5 and Chapter 6.

### 1.2.2 The Quantized Hall Effect

The “Hall effect” or “Hall measurement” was discovered in the nineteenth century [15]. This Hall measurement of conductivity in presence of weak magnetic field is very useful for characterizing semiconducting thin films because both the electron density and mobility can be measured simultaneously. When crossed magnetic and electric fields are applied to a rectangular bar shown in Fig. 1.5, a voltage is induced in a direction orthogonal to the crossed fields, as evidenced by an induced current flowing in that direction - the Hall current. Crossed magnetic and electric fields, denoted respectively, by  $\vec{H}$  and  $\vec{E}$ , act as velocity filters to free charges, letting through only those whose velocity  $v$  is such that  $\vec{E} + (\vec{v}/c)\vec{H} = 0$ , or

$$\frac{\vec{v}}{c} = -\frac{\vec{E}}{\vec{H}} \quad (1.1)$$

For free charge carriers in a metal, the current density is

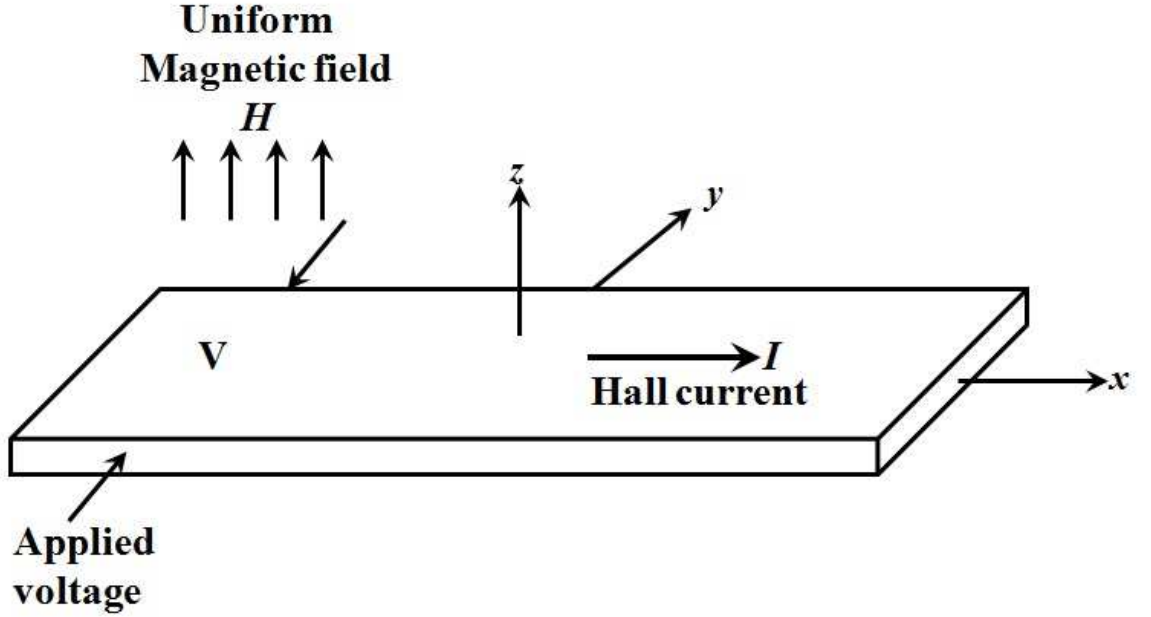


Figure 1.5: The Hall effect. A current  $I$  flows in a direction orthogonal to crossed electric and magnetic fields. The Hall resistivity is defined as  $\rho_{xy} = V/I$ . The conventional resistivity  $\rho_{xx}$  can be obtained by measuring the voltage drop along the direction of the current. [16]

$$j = qn\vec{v} \quad (1.2)$$

where  $q$  is the charge and  $n$  is the density. The Hall resistivity  $\rho_{xy}$  is defined as the ratio of the electric field (in the  $y$  direction) to the Hall current density (in the  $x$  direction):

$$j = \frac{\vec{E}}{\rho_{xy}} \quad (1.3)$$

Substituting Eq. (1.3) into Eq. (1.2) and then into Eq. (1.1), we obtain

$$\rho_{xy} = \frac{\vec{H}}{qnc} \quad (1.4)$$

Measurements of the Hall resistivity in various metals has yielded charge carrier densities and provided the first demonstrations that there are not only negative charge carriers (electron), but also positive ions (holes). From classical Drude model [17], the longitudinal resistance is independent of the applied magnetic field whereas the Hall resistance is a linear function of  $\vec{H}$ . As long as the magnetic field is very low, Drude model for Hall effect is valid.

## The Integer Quantum Hall Effect

In 1980 Klaus von Klitzing et. al. used the two-dimensional electron gas formed in a silicon MOSFET device and performed the Hall experiment at very low temperatures for stronger magnetic fields. They measured the direct resistivities  $\rho_{xx}$  and the Hall resistivities  $\rho_{xy}$ . The longitudinal resistivities shows oscillation in  $\vec{H}$  and the

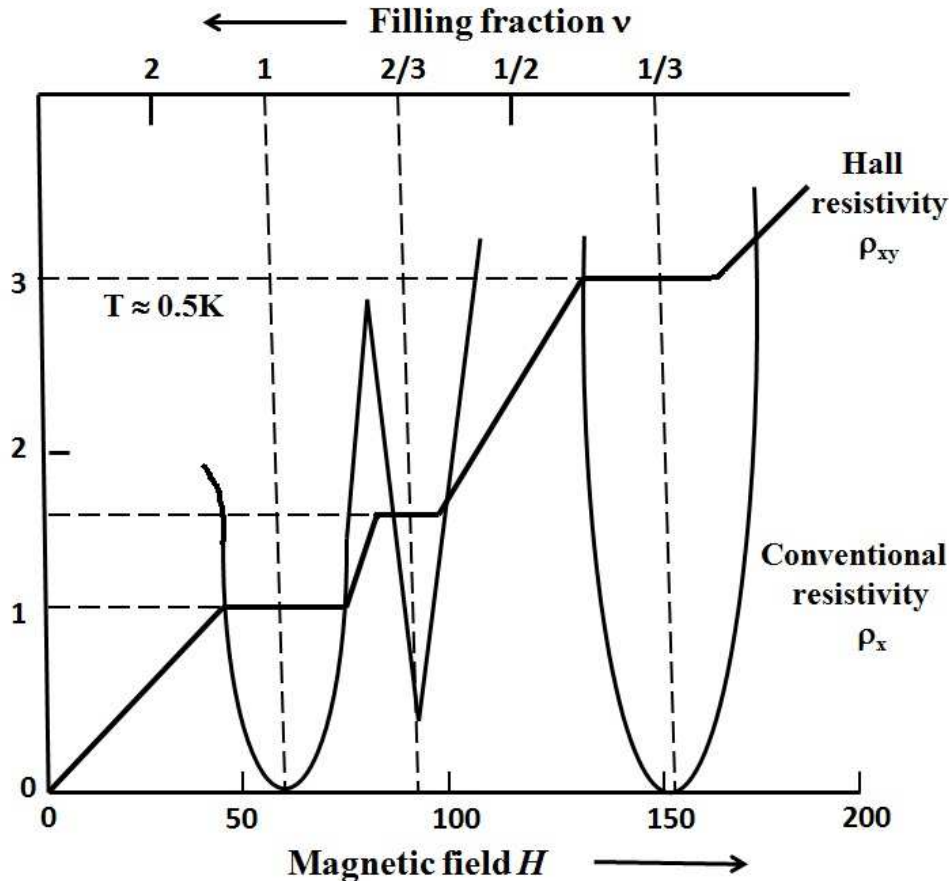


Figure 1.6: Quantized Hall effect: Schematic representation of experimental data. The filling fraction  $\nu$  is the fraction of degenerate states in the lowest Landau levels occupied by electrons. The Hall resistivity exhibits plateau of value  $1/\nu$ , at  $\nu = 1, \frac{2}{3}, \frac{1}{3}$  (in units of  $h/e^2$ .) The conventional resistivity becomes very small at these values. The quantization is accurate to at least one part in  $10^4$ .

Hall resistivity exhibits plateau corresponding to the minima in the longitudinal resistivities shown in the Fig. 1.6. These features can be explained in terms of Landau levels which are purely quantum effect. Thus two-dimensional electron gas shows Quantum Hall effect [18] when it is placed under a strong perpendicular magnetic field. As the magnetic field  $\vec{H}$  increases, the degeneracy of the Landau levels increases. Since the electron density does not depend on the field the filling

fraction  $\nu$  of the lowest Landau level decreases:

$$\nu \equiv \frac{hcn}{e\hbar} \quad (1.5)$$

The Hall resistivity exhibits plateaus at  $\nu = 1, \frac{2}{3}, \frac{1}{3}$ , with values equal to  $1/\nu$ , in units of  $h/e^2$ . At the same time, the conventional resistivity  $\rho_{xx}$  drops to very low values. This indicates that in the neighborhood of these special filling fractions the two-dimensional electron gas flows with almost no resistance. The value at  $\nu = 1$ , called the integer quantized Hall effect. The Hall resistivity was found to be quantized with a precision of one part in  $10^5$  [18].

At  $\nu = 1$  the lowest Landau level is completely filled, there is an energy gap above the Fermi level. Low-energy excitations are therefore impossible, and so the centers of the electron orbits flow like a free gas. Using Eq. (1.4), with  $n = eH/hc$ . The Landau degeneracy per unit area, we immediately obtain the desired result.

$$\rho_{xy} = \frac{h}{e^2} \quad (1.6)$$

The precision of the Integer Quantum Hall Effect is so accurate that it now forms the international standard of resistance.

### The Fractional Quantum Hall Effect

Going to stronger magnetic fields and to lower temperatures in two-dimensional electron gases, one can observe additional plateaus of the Hall resistance at fractional filling factors like  $\nu = \frac{1}{3}, \frac{1}{5}$  etc. (Fig. 1.6). This so-called fractional quantum Hall effect has been discovered by Daniel Tsui et. al. [19] in 1982. The features at fractional filling can be traced back to the existence of correlated collective quasi-particle excitations [20]. Thus, in contrast to the integer quantum Hall effect, the Coulomb interactions between the electrons is essential for the explanation of the fractional quantum Hall effect. The quasi-particles have fractional charge (for instance  $e/3$  at  $\nu = \frac{1}{3}$ ). From shot noise measurements [21], it could be confirmed that the charge carriers at  $\nu = \frac{1}{3}$  in the fractional quantum Hall effect regime have indeed charge  $e/3$ . After this confirmation, Tsui, Störmer and Laughlin received the 1998 Nobel prize for the discovery and interpretation of the fractional quantum Hall effect.

### 1.2.3 Universal Conductance Fluctuations

At low temperatures, the conductance of disordered wires in the mesoscopic regime exhibits pronounced fluctuations as a function of external parameters like the magnetic field or the Fermi energy [22]. These fluctuations were discovered [23] in the low-temperature (below 1K) conductance of the inversion layer in a disordered

silicon MOSFET. In 1986, Washburn and Webb [11] measured the fluctuation in conductance of an *Au* wire as a function of applied magnetic field at 10mk. These fluctuations are not time dependent noise as they are completely reproducible. The origin of the fluctuations lies in the interference of different ways the electrons can take when travelling through the sample, as sketched in Fig. 1.7. Supporting the

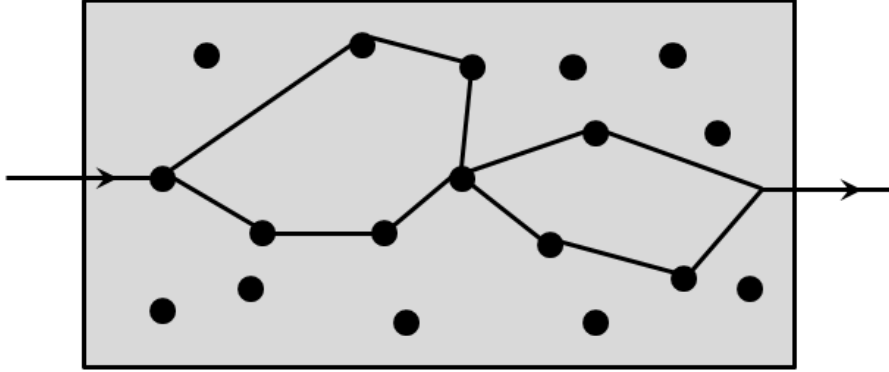


Figure 1.7: Possible paths of an electron through a disordered wire, with elastic scattering processes at impurities. The interference of such paths is influenced by a magnetic field or the value of the Fermi wave vector, leading to fluctuations of the conductance in the mesoscopic regime.

earlier theory on conductance fluctuations [24] these data showed that the magnitude of fluctuation is of order  $\frac{e^2}{h}$ . These fluctuations are universal in nature because firstly the variance of conductance is of order  $(\frac{e^2}{h})^2$ , independent of sample size and the strength of impurities and secondly this variance decreases precisely by a factor of two when time reversal symmetry is broken. This variance of conductance is weakly dependent on the shape of the conductor. At zero temperature, for a quantum wire the variance  $\frac{\Delta G}{G_0}$  is independent of the mean free path  $l_m$ , wire length  $L$  or the number of transverse modes  $N$  as long as the wire is much longer than the mean free path but much shorter than the localization length, i.e.,  $l_m \ll L \ll Nl_m$ . Various explanations came after the discovery of the universality of conductance fluctuations. Imry's argument was in terms of transmission eigenvalues [25]. Most transmission eigen values are exponentially small in disordered conductor while a fraction  $\frac{l_m}{L}$  of the total number  $N$  of transmission eigenvalues is of order unity. Depending on this transmission eigenvalues, the corresponding channels are referred as closed and open channels. Only the open channels contribute to the conductance:  $\frac{G}{G_0} \equiv N_{open} \approx N \frac{l_m}{L}$ . Thus the fluctuations in conductance can be interpreted as the fluctuations in number  $N_{open}$  of the open channels in the sample. If the transmission eigenvalues were uncorrelated, one would calculate that the fluctuations in  $N_{open}$  would have been of the order  $\sqrt{N_{open}}$  which would imply the variance in con-

ductance  $\frac{\Delta G}{G_0}$  would be of order  $N_{open}$  ( $\geq 1$ ). Due to the strong suppression of fluctuations in  $N_{open}$  by eigenvalue repulsion the variance of conductance is of order unity.

### 1.2.4 Quantized Conductance in Quantum Point Contacts

A point contact is a very narrow link between two conducting materials. Such a link can be formed by imposing a confining constriction in a wire or by forcing the electrons to pass through a narrow channel defined electrostatically when they are driven from one two- or three-dimensional region of the sample to the other. In the case of very narrow constrictions of width  $W$ , narrower than the mean free path and the phase coherence length ( $W \ll l_m, L_\phi$ ), such a constriction is called ballistic quantum point contact. In 1988, van Wees et. al. [24] and Wharam et. al. [27]

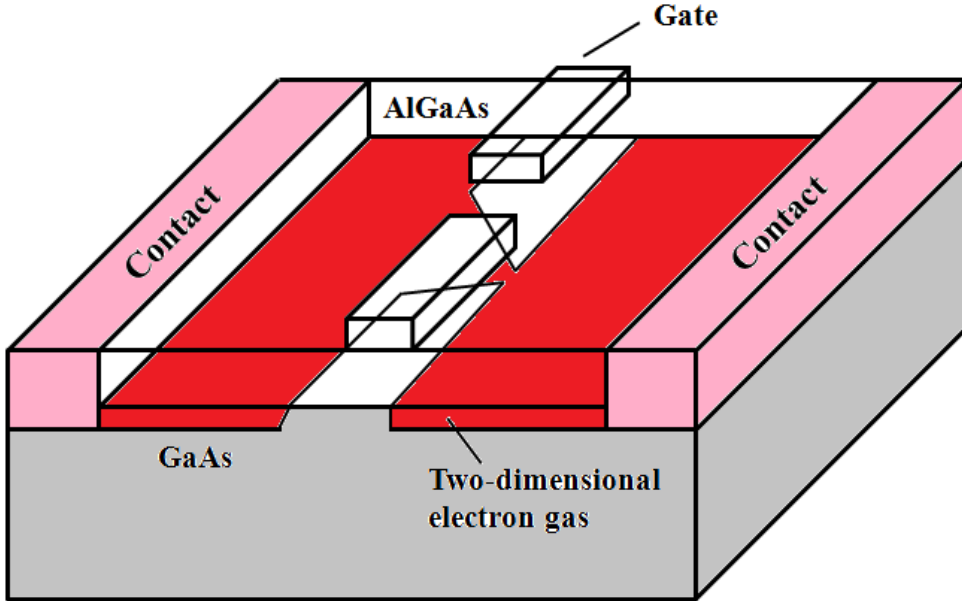


Figure 1.8: QUANTUM POINT CONTACT scheme. The contact is defined in a high-mobility two-dimensional electron gas at the interface of a GaAs-AlGaAs heterojunctions. The point contact is formed when a negative voltage is applied to the gate electrodes on top of the AlGaAs layer. Transport measurements are made by employing contacts to the two-dimensional electron gas at either side of the constriction [26].

independently observed the two-probe conductance of a quantum point contact at sub-Kelvin temperature. In absence of applied magnetic field, they measured the

conductance  $G$  as a function of the gate voltage  $V_g$ . Assuming the linear dependence of the width of quantum point contact on  $V_g$ , they showed the conductance decreases with narrowing constriction. However, around this classical dependence,  $G$  changes in quantized steps of  $\frac{2e^2}{h}$ . These data exhibited conductance plateaus quantized in integer multiples of fundamental conductance  $G_0 = \frac{2e^2}{h}$  as  $G = NG_0$ . Typically all these measurements were performed in a two-terminal configuration where voltage and current measured through the same set of source-drain contacts. The number  $N$  increases with the decrease in gate voltage, i.e., as the gate-voltage is made less negative. As the gate voltage is made more negative, the potential in the narrow region of the quantum point contact squeezes the 2-DEG, pushing successive one-dimensional sub-bands through the Fermi energy. As each one-dimensional sub-band is depopulated, the conductance drops by an amount  $G_0$  until finally all the sub-bands are completely depopulated and conductance approaches zero. The conductance quantization is not as exact as the Hall effect. A series resistance originating from the wide 2-DEG regions have been subtracted [24] to line up the plateaus at their quantized values and the plateaus are not completely flat.

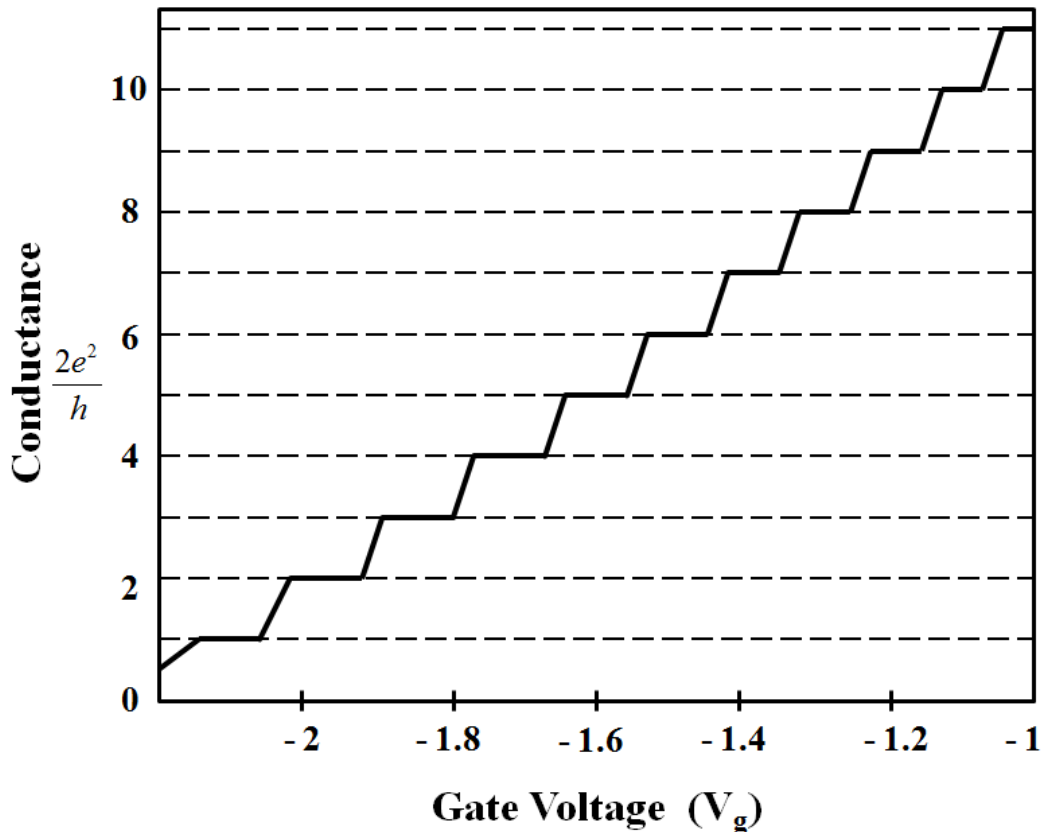


Figure 1.9: Schematic representation of experimental data. The conductance through a quantum point contact as a function of the gate voltage. The conductance exhibits clear steps of height  $\frac{2e^2}{h}$  (from [24]).

### 1.2.5 Violation of Onsager's Symmetry Relation

The Onsager-Casimir relation was originally derived for macroscopic conductors using thermodynamic arguments. These are symmetry condition for correlation functions. In electronic transport measurements, microscopic reversibility requires that in the presence of a magnetic field  $\vec{B}$  the conductance obeys  $G_{ij}(B) = G_{ij}(-B)$  between contacts  $i$  and  $j$ . In particular for a two-probe conductor the conductance is an even function of magnetic field  $G(B) = G(-B)$ . Such relation generally hold for macroscopic systems near thermodynamic equilibrium. Experimentally [28] there is no evidence that this relation is ever violated in the linear response regime regardless of the nature of the transport. When transport is phase coherent as it occurs in mesoscopic conductors, the conductance is not just material specific but also depends on the probe configuration. Four-probe conductance of a sample is not symmetric under flux reversal, i.e.,  $G_{ij,kl}(B) \neq G_{ij,kl}(-B)$ . Herein, the first pair of indices represents the probes used to supply and draw current, while the last pair of indices denote the probes used to measure the potential difference. Though Onsager's symmetry relations fail in this regime but Onsager's reciprocity relations [29] holds. The reciprocity relations tell us the conductance of a mesoscopic sample is invariant under the magnetic field reversal accompanied by the exchange of voltage and current probes, i.e.,  $G_{ij,kl}(B) = G_{kl,ij}(-B)$ . This also prove that unlike bulk sample there is no material specific quantities like resistivity (or conductivity). Instead there are only global properties like resistance [30].

### 1.2.6 Persistent Current

The existence of persistent currents was first suggested by London in 1937 [31], in his studies on the diamagnetism of aromatic rings (benzene rings). In 1938, Hund suggested that such an effect could be present in clean, metallic samples at low temperature [32]. The amplitude of the persistent current was first calculated by Bloch and Kulik in the case of a clean, one-dimensional ring [33, 34], but their existence in a real, diffusive three-dimensional metallic ring was only been predicted by Büttiker et al. [14] in 1983. In their seminal paper, they suggested the existence of persistent current even in a normal metal closed loop (e.g., ring) but in the presence of Aharonov - Bohm flux. Later experiments in diffusive as well as ballistic normal and semiconducting rings showed the existence of persistent currents. In 1990, Lévy et al. measured the low-temperature magnetization response of  $10^7$  isolated mesoscopic copper rings to a slowly varying magnetic flux [35]. At sufficiently low temperature, the total magnetization response oscillates as a function of the enclosed magnetic flux on the scale of *half a flux quantum*. In 1991, Chandrasekhar et al. measured the low-temperature magnetic response of single, isolated, micron size Au loops [36]. In 1993, Maily et al. measured the magnetic response of GaAlAs/GaAs

mesoscopic ring [37]. There is a discrepancy between the experimentally measured and theoretically predicted magnitude of the persistent currents. It is seen that the magnitude of persistent currents measured experimentally is an order of magnitude larger than predicted by theory. The theoretical aspects of persistent current is described in detail in Chapter 3: Some Basic Theories.



## Chapter 2

# TRANSPORT FORMALISMS USED IN MESOSCOPIC SYSTEM

*“asato mā sad gamaya  
tamaso mā jyotir gamaya  
mrtyor mā amrtarṇ gamaya”*

From ignorance lead me to truth  
From darkness lead me to light  
From death lead me to immortality.  
–(1-6-28, Brihadaranyaka Upanishad).

Drude formalism is based on classical Brownian motion and explains Ohmic behavior. Boltzmann transport is based on Brownian motion along with the appropriate distribution law of the carriers. Then there are quantum formalisms like Kubo formalism and Keldysh formalism but in mesoscopic system, the appropriate formalism is Landauer-Büttiker formalism which explicitly accounts for sample size, sample geometry, specific connectivity to reservoirs, sample specific impurity configuration etc. Thermodynamic properties of a sample closely depend on the mechanism of transport in the sample. One can study a transport property and acquire knowledge about the thermodynamic property of the sample and vice versa. Mesoscopic transport regimes can be categorized into three major regimes like

- (i) localized transport regimes,
- (ii) diffusive transport regime and
- (iii) ballistic transport regime.

## 2.1 Transport regime

Depending upon the values of characteristic lengths described in Chapter 1 in subsection 1.1.1, in comparison with the system size  $L$ , different transport regimes can be distinguished.

- (i) **Localized transport regime** For a disordered system we know that electronic states are localized at  $x_0$  within a length scale  $L_l$ , i.e., the electron density typically decay as  $e^{-\frac{(x-x_0)}{l_l}}$ . Conductivity of such a sample in the bulk is 0 but if the mesoscopic sample dimension is comparable to  $L_l$  then the sample can conduct and its conductance has to be studied using Landauer-Büttiker formalism. Although a conductivity cannot be defined as explained in Landauer-Büttiker formalism which explicitly accounts for sample size, sample geometry, specific connectivity to reservoirs, sample specific impurity configuration etc.
- (ii) **Diffusive transport regime** This typically happen in mesoscopic metallic samples. Here the disorder is not strong enough to localize the electrons but also not weak enough to allow ballistic transport.
- (iii) **Ballistic transport regime** This typically happens in mesoscopic semi-conducting sample where Fermi energy is very low and for such long wavelengths impurity scattering do not play a significant role.

Landauer-Büttiker formalism apply to all three regimes.

## 2.2 The Landauer-Büttiker Formalism

The earliest application of current formulas was in the calculation of the current-voltage characteristics of tunnelling junctions where the transmission probability is usually much less than unity [38]. Rolf Landauer in 1957 gave a physical argument for calculating the conductance of a mesoscopic scatterer where leads are explicitly accounted for. The effect of environment comes into picture through the attached leads. In contrast to Kubo formalism which is time-dependent, the Landauer formula connects the conductance of a mesoscopic system to its scattering properties. Landauer brilliantly captured the wave nature of electrons in mesoscopic conductors. In the linear transport regime, i.e., for very small bias, the conductance is effectively determined by the *transmission probabilities of propagating modes* analogous to electromagnetic fields in optical waveguide [39, 40]. For ballistic conductor, he drew attention to the wise question, ‘*where does this resistance come from?*’ that arise when we apply this relation to conductors having transmission probabilities close to unity. Imry [41] clarified this question using earlier notions due to Engquist

and Anderson [42]. M. Büttiker [43, 44, 45] extended this approach to describe multi-terminal measurements in presence of magnetic field.

### 2.2.1 General Landauer Conductance Formula

To derive the Landauer conductance formula, we consider a mesoscopic conductor at zero temperature connected to two electron reservoirs (contacts) by ideal leads (LEAD 1 and LEAD 2) as shown in Fig. 2.1 in quasi one-dimension. These leads are made up of normal metal or semiconductor. There can be only single channel (or modes) or multi-channel in these leads. These leads can act as a waveguide. In the next paragraph we explain how the leads can act as an electron wave guide. The left

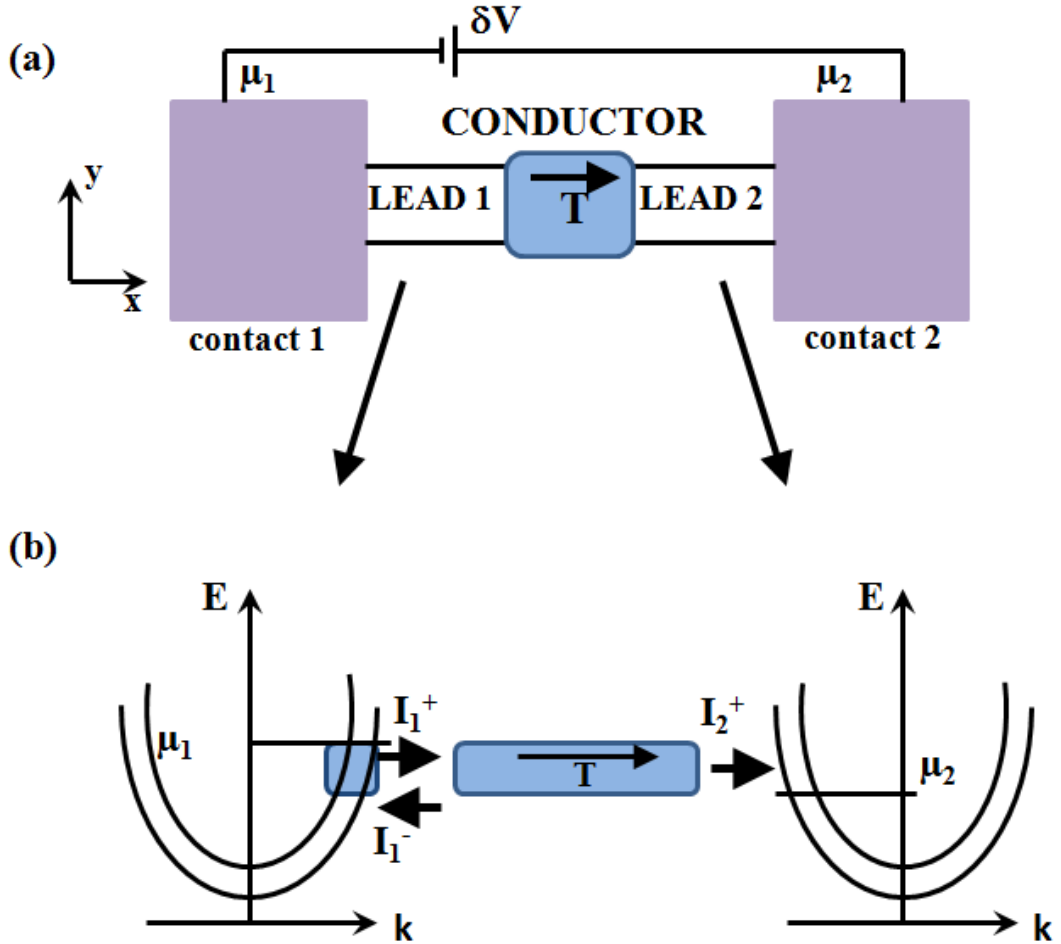


Figure 2.1: (a) A conductor having a transmission probability of  $T$  is connected two large contacts through two leads (LEAD 1 and LEAD 2). ‘Zero’ temperature is assumed such that the energy distributions of the incident electrons in the two leads can be assumed to be step functions. (b) Dispersion relations  $E(k)$  vs.  $k$  for the different transverse modes (or subbands) in the leads. Figure is taken from [6].

and right reservoirs are characterized by chemical potential  $\mu_1$  and  $\mu_2$  respectively.

The conductor is represented as a scattering region (shaded region in Fig. 2.1). When  $\mu_1 > \mu_2$ , current starts flowing through the system from left to right. The left hand electron reservoir acts as a source and the right hand electron reservoir acts as a sink of electrons and by definition, there is no phase relationship between the absorbed and emitted electrons. The current is seen as a consequence of the imbalance of chemical potential at the external reservoirs. The reservoirs act as an inelastic scatterer and is a source of energy dissipation.  $T$  is the average probability that an electron injected in LEAD 1 will transmit to LEAD 2. In the following sections, we assume ‘zero-temperature’ so that there is current flow only in the energy range  $\mu_1 > E > \mu_2$ .

### Quantum Waveguide Theory

The two dimensional electron gas (2-DEG) described in Fig. 1.2 is like a two dimensional plane consisting of highly mobile electrons. This 2-DEG can be etched from two sides to form a very thin strip of width  $a$ , negligible thickness (to be explained latter), and theoretically infinite length, called a quantum wire. LEAD 1 and LEAD 2 in Fig. 2.1 are quantum wires. They can act like an electron waveguide. A waveguide is a structure that guide waves, such as electromagnetic waves or sound waves. Waves in open source propagate in all directions, in this way they lose their power proportionally to the square of the distance (inverse square law), i.e., at a distance  $R$  from the source. The waveguide confines the wave to propagate in one direction so that (under ideal condition) it loses no power while propagating. Waveguide may refer to any linear structure that conveys waves between its endpoints. At very low temperatures (typically mK), the scattering by phonons is significantly suppressed, and the phase coherence length can become large compared to the system size. In this regime the electron maintains the single particle phase coherence across the entire sample. To understand the waveguide nature of the leads we consider a two-dimensional conductor that is uniform in the  $x$ -direction and has some transverse confining potential  $V(y)$  shown in Fig. 2.2. The detailed analysis of quantum waveguide theory for one-dimensional mesoscopic structures of waveguide type is given in Xia’s paper [46].

The starting point is the Schrödinger equation:

$$-\frac{\hbar^2}{2m^*} \left( \frac{\partial^2 \psi}{\partial x^2} + \frac{\partial^2 \psi}{\partial y^2} \right) + V(x, y) \psi(x, y) = E \psi(x, y) \quad (2.1)$$

We assume that the width of the structure is narrow enough compared to the length of the structure so that the energy spacing between the quantum energy levels produced by the transverse confinement is much larger than the energy range of the longitudinal transport. Without any loss of generality we take  $V(x, y) = V(y)$  to be

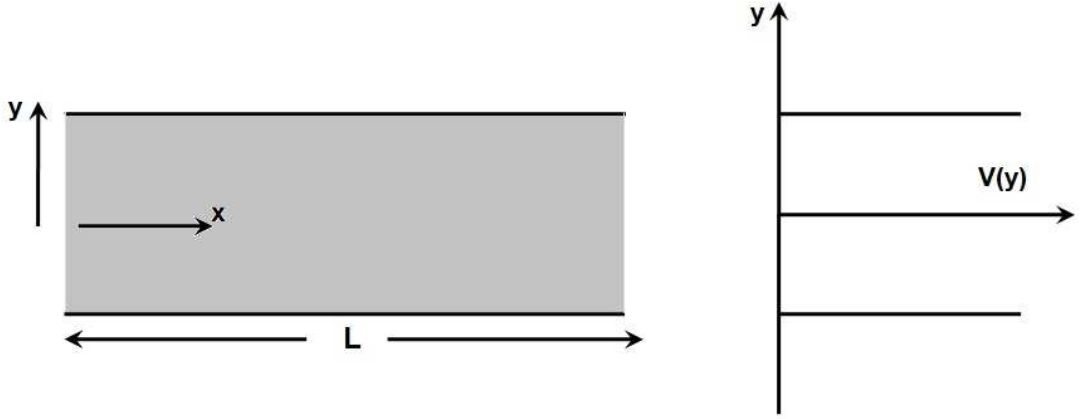


Figure 2.2: A rectangular conductor assumed to be uniform in the  $x$ -direction, extending from  $x = -\infty$  to  $x = \infty$  and having some transverse confinement potential  $V(y)$ .

an infinite square well potential of width  $a$ . That is

$$V(y) = 0 \quad \text{for } -a/2 \leq y \leq a/2$$

and

$$V(y) = \infty \quad \text{for } |y| > a/2 \quad (2.2)$$

The wave functions can be obtained by solving Eq. (2.1). From Eq. (2.1) and (2.2) we get

$$-\frac{\hbar^2}{2m} \left( \xi(y) \frac{\partial^2 \phi(x)}{\partial x^2} + \phi(x) \frac{\partial^2 \xi(y)}{\partial y^2} \right) + V(y) \phi(x) \xi(y) = E \phi(x) \xi(y)$$

where

$$\psi(x, y) = \phi(x) \xi(y) \quad (2.3)$$

Dividing both sides by  $\phi(x) \xi(y)$  we get

$$\begin{aligned} -\frac{\hbar^2}{2m} \left[ \frac{1}{\phi(x)} \frac{\partial^2 \phi(x)}{\partial x^2} + \frac{1}{\xi(y)} \frac{\partial^2 \xi(y)}{\partial y^2} \right] + V(y) &= E \\ -\frac{\hbar^2}{2m} \left[ \frac{1}{\phi(x)} \frac{\partial^2 \phi(x)}{\partial x^2} + \frac{1}{\xi(y)} \frac{\partial^2 \xi(y)}{\partial y^2} \right] + V(y) &= E_1 + E_2 \end{aligned} \quad (2.4)$$

where

$$E = E_1 + E_2 \quad (2.5)$$

After separating the variables we get

$$-\frac{\hbar^2}{2m} \frac{1}{\phi(x)} \frac{\partial^2 \phi(x)}{\partial x^2} = E_1 \quad (2.6)$$

$$-\frac{\hbar^2}{2m} \frac{1}{\xi(y)} \frac{\partial^2 \xi(y)}{\partial y^2} + V(y) = E_2 \quad (2.7)$$

Eq. (2.6) has a solution of the form

$$\phi(x) = e^{\pm ik_n x} \quad (2.8)$$

or

$$\phi(x) = A_n e^{ik_n x} + B_n e^{-ik_n x} \quad (2.9)$$

From Eq. (2.6) we can write

$$E_1 = \frac{\hbar^2 k_n^2}{2m}$$

From Eq. (2.7)

$$-\frac{\hbar^2}{2m} \frac{\partial^2 \xi(y)}{\partial y^2} + V(y)\xi(y) = E_2 \xi(y) \quad (2.10)$$

Eq. (2.10) has a solution of the form

$$\xi(y) = e^{\pm ik' y}$$

Thus the wave function  $\xi(y)$  becomes

$$\xi(y) = C_l e^{ik' y} + D_l e^{-ik' y}$$

or

$$\xi(y) = F_l \cos(k' y) + G_l \sin(k' y) \quad (2.11)$$

where  $F_l = C_l + D_l$  and  $G_l = (C_l - D_l)i$ . When  $y = -a/2$ ,  $\xi(-a/2) = 0$ . So,

$$\xi(-a/2) = F_l \cos\left(\frac{k' a}{2}\right) - G_l \sin\left(\frac{k' a}{2}\right) = 0 \quad (2.12)$$

Similarly, when  $y = +a/2$ ,  $\xi(a/2) = 0$ . So,

$$\xi(a/2) = F_l \cos\left(\frac{k' a}{2}\right) + G_l \sin\left(\frac{k' a}{2}\right) = 0 \quad (2.13)$$

Linear combination of cos function and sin function can not be zero for a given  $k'$ .

They have to be separately zero.

Thus, solution is either

$$\xi(y) = F_l \cos(k'y) \quad (2.14)$$

or

$$\xi(y) = G_l \sin(k'y) \quad (2.15)$$

Let us first consider the even solution i.e., Eq. (2.14), at  $y = -a/2$ ,  $\xi(-a/2) = 0$ . Excluding  $F_l = 0$

$$\cos(k'a/2) = 0 = \cos\left(\frac{(2l+1)\pi}{2}\right)$$

where  $l = 0, 1, 2, 3, \dots$ . Therefore,

$$k' = \frac{(2l+1)\pi}{a} \quad (2.16)$$

Putting the value of  $k'$  in Eq. (2.14) we get

$$\xi(y) = F_l \cos\left[\frac{(2l+1)\pi y}{a}\right] \quad (2.17)$$

Now, let us consider the odd solution, i.e.,

$$\xi(y) = G_l \sin(k'y)$$

At  $y = a/2$ ,  $\xi(a/2) = 0$ . Excluding  $G_l = 0$

$$\sin(k'a/2) = 0 = \sin l'\pi$$

where  $l' = 0, 1, 2, 3, \dots$  therefore,

$$k' = \frac{2l'\pi}{a} \quad (2.18)$$

Thus, the odd solution is

$$\xi(y) = G_l \sin\left(\frac{2l'\pi y}{a}\right) \quad (2.19)$$

Now combining Eq. (2.15) and Eq. (2.17) we can write

$$\xi(y) = K_n \sin\frac{n\pi}{a}\left(\frac{a}{2} + y\right) \quad (2.20)$$

where  $n = 0, 1, 2, 3, \dots$  any integer. For even values of  $n$ , we get Eq. (2.17) and for odd values of  $n$ , we get Eq. (2.15). Here  $K_n$  is the normalization constant. From Eq. (2.5) we can write

$$E = \frac{\hbar^2 k_n^2}{2m} + \frac{n^2 \pi^2 \hbar^2}{2ma^2} \quad (2.21)$$

Putting the value of  $\phi(x)$  from Eq. (2.9) and  $\xi(y)$  from Eq. (2.20) in Eq. (2.3) the complete wavefunction becomes

$$\psi(x, y) = \left[ \frac{A_n}{\sqrt{k_n}} e^{ik_n x} + \frac{B_n}{\sqrt{k_n}} e^{-ik_n x} \right] \left[ K_n \sin \frac{n\pi}{a} \left( \frac{a}{2} + y \right) \right] \quad (2.22)$$

Since we know that the normalization constant include a factor  $\frac{1}{\sqrt{k_n}}$  to conserve current. This shows how the structure In Fig. 2.2 has become a waveguide. A right moving wave for example is given by

$$\psi(x, y) = \frac{L_n e^{ik_n x}}{\sqrt{k_n}} \left[ \sin \frac{n\pi}{a} \left( \frac{a}{2} + y \right) \right] \quad (2.23)$$

and it is a plane wave that remains undiminished in amplitude  $\frac{L_n}{k_n}$  upto  $+\infty$ . A left moving wave for example is given by

$$\psi(x, y) = \frac{M_n e^{-ik_n x}}{\sqrt{k_n}} \left[ \sin \frac{n\pi}{a} \left( \frac{a}{2} + y \right) \right] \quad (2.24)$$

and it is a plane wave that remains undiminished in amplitude  $\frac{M_n}{k_n}$  upto  $-\infty$ . In a quantum waveguide Eq. (2.23) implies a steady incident beam towards the right and Eq. (2.24) implies a steady incident beam towards the left. If such a steady beam encounters a scatterer then scattering will take place and such scattering is crucial to understand mesoscopic phenomena.  $k_n$  for different  $n$  correspond to the different partial waves.

Scattering is a general physical process where some form of radiation, such as light, sound, or moving particles, are forced to deviate from a straight trajectory by one or more paths due to localized non-uniformities in the medium through they pass. Electron motion in a mesoscopic sample is governed by Schrödinger equation and elastic scattering plays a very prominent role. Elastic scattering can be treated in the time dependent approach wherein we see the time evolution of a wave packet or it can be treated in the time independent approach where we make a partial wave analysis of a steady beam. In the probabilistic interpretation of quantum mechanics both approaches give identical results. We will essentially use this second approach in this thesis.

General solution of scattered wave function in three-dimension [47] is given by

$$\psi(r, \theta, \phi) \xrightarrow{r \rightarrow \infty} A \left[ e^{ikz} + f(\theta, \phi) \frac{e^{ikr}}{r} \right] \quad (2.25)$$

In Eq. (2.3), the term  $\frac{e^{ikr}}{r}$  signifies same number of particles within a sphere of

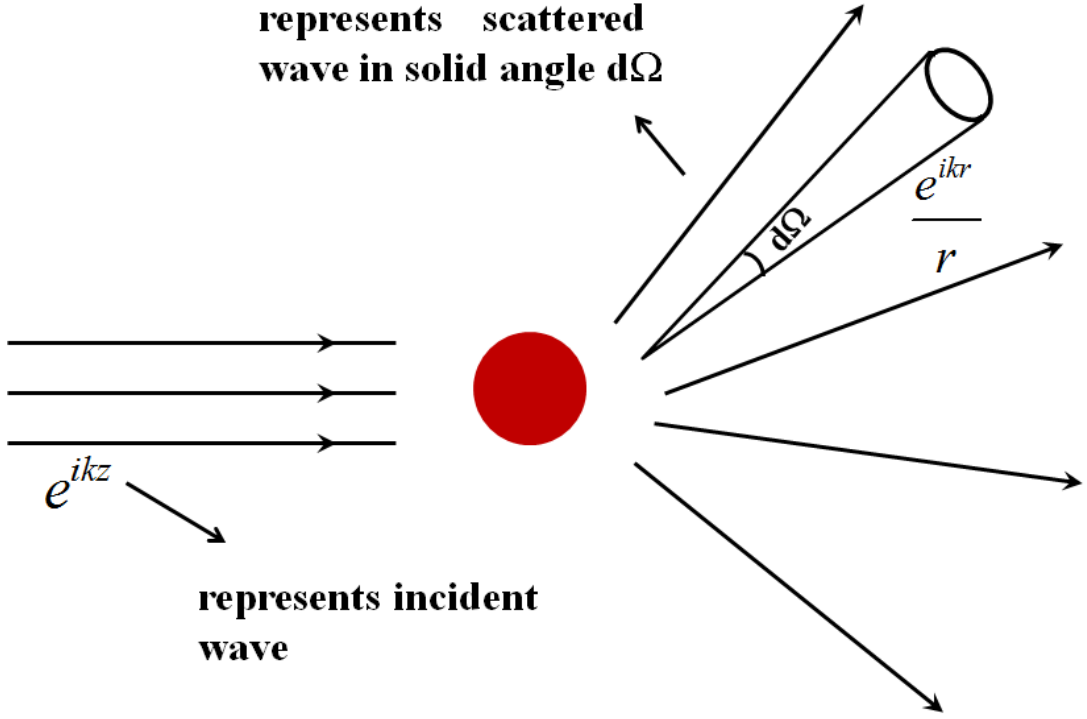


Figure 2.3: Scattering phenomena in three dimension.

radius  $r$ , so intensity has to fall as  $\frac{1}{r}$ .  $f(\theta, \phi)$  signifies angular dependence.

$$\frac{d\sigma}{d\Omega} = |f(\theta, \phi)|^2$$

where  $d\sigma$  = differential scattering cross section.  $f(\theta, \phi)$  expands as

$$f(\theta, \phi) = \frac{1}{k} \sum_{l=0}^{\infty} (-1)^{l+1} C_l Y_l(\theta, \phi) \quad (2.26)$$

For different  $l$  vanishes we get different partial waves.

The same phenomenon in quasi one-dimension is schematically shown in Fig. 2.4. From Eq. (2.23) and Eq. (2.24), we can write the wave function in Lead 1 and Lead 2 as shown in the Fig. 2.4 in respective places. Comparing with Eq. (2.26) we find here  $f(\theta, \phi)$  takes the form  $r_1^{(1)}$ ,  $r_2^{(1)}$ ,  $t_1^{(1)}$ ,  $t_2^{(1)}$  etc which again constitute different partial waves.

### Current calculation

In a narrow conductor due to confinement in transverse direction, several modes or channels are present. Only the propagating modes, i.e.,  $k_x^2 \geq 0$  participate in

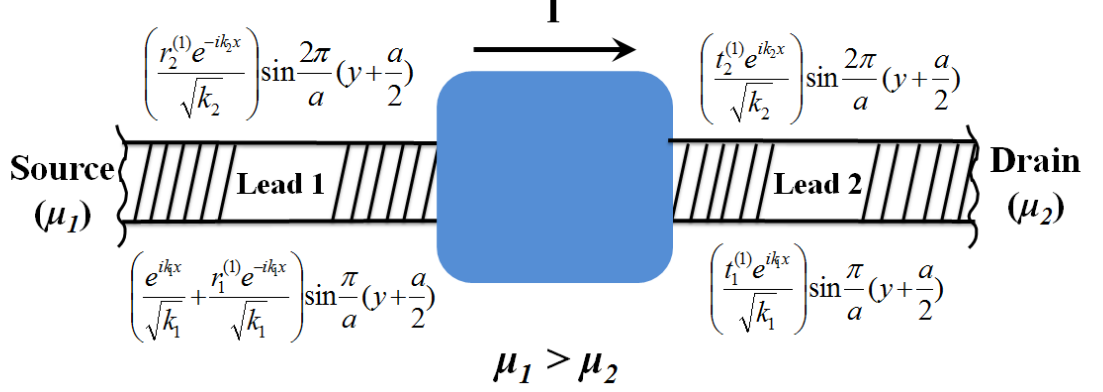


Figure 2.4: Mesoscopic transport problem in quasi one-dimension. Mesoscopic sample (blue region) connected to two electron reservoirs characterized by chemical potential  $\mu_1$  and  $\mu_2$ , respectively, by ideal leads (Lead1 and Lead2). A potential difference,  $\mu_1 - \mu_2$ , drives a current  $I$  through the sample.

conductance. The dispersion curve for each mode has a cut-off energy

$$\varepsilon_n = E(n, k = 0)$$

below which it cannot propagate. The number of transverse modes at an energy  $E$  is obtained by counting the number of modes having cut-off energies smaller than  $E$ :

$$M(E) = \sum_n v(E - \varepsilon_n) \quad (2.27)$$

For simplicity we consider equal number of transverse modes  $M(E)$  are present in both leads, i.e., leads are of equal width.

Let us consider a single transverse mode whose  $k_x$  states are occupied according to some function  $f(E)$ . A uniform electron gas with  $m$  electrons per unit length moving with a velocity  $v_i$  carries a current equal to  $emv$ . The current injected from left reservoir into lead 1 carried by channel  $i$  in a small energy interval  $dE$  is given by

$$dI_{in}^i = ev_i(\partial n^{(i)}/\partial E)f(E)dE \quad (2.28)$$

Here  $v_i$  is the longitudinal velocity along  $x$ -direction of the electrons at the energy  $E$  and the density of states in the leads for the  $i$ th mode is

$$(\partial n^{(i)}/\partial E) = \frac{\partial n^{(i)}}{\partial k^i} \frac{\partial k^{(i)}}{\partial E} = \frac{1}{2\pi} \frac{1}{\hbar v_i}$$

and  $f(E)$  is the Fermi distribution. The total current flow  $dI_S$  in a small energy interval  $dE$  through the system is given by the current injected into the wires by reservoirs multiplied by the transmission coefficient  $T$ . Using these two relations in Eq. (2.28) we find that

$$dI_{in}^i = \frac{e}{2\pi\hbar} f(E) dE \quad (2.29)$$

which is same for all propagating modes (channels) present in the system. Thus the total influx of current from LEAD 1 in Fig. 2.1 is given by

$$dI_{in} = \frac{e}{2\pi\hbar} M(E) f(E) dE \quad (2.30)$$

In linear transport regime  $\mu_1 - \mu_2$  is very small and taken to be  $dE$ . We can write the above equation as

$$dI_{in} = \frac{2e}{h} M(E) (\mu_1 - \mu_2) \quad (2.31)$$

2 is incorporated in Eq. (2.31) due to spin and the function  $M(E)$  gives the number of modes that are above cut-off at energy  $E$ . The current carried per mode per unit energy by an occupied state is equal to  $2|e|/h$  (which is about 80nA.meV).

### Contact resistance

Assuming that the number of modes  $M$  is constant over the energy range  $\mu_1 > E > \mu_2$ , we can write

$$G_c = \frac{dI_{in}}{(\mu_1 - \mu_2)/e} \quad (2.32)$$

Substituting  $dI_{in}$  from Eq. (2.31) we get

$$G_c = \frac{2e^2}{h} M \quad (2.33)$$

so that the contact resistance, which is the resistance of a ballistic waveguide is given by

$$G_c^{-1} \equiv \frac{(\mu_1 - \mu_2)/e}{dI_{in}} = \frac{h}{2e^2 M} \approx \frac{12.9k\Omega}{M}$$

This resistance occurs at the contact between left reservoir and LEAD 1. The contact resistance goes down inversely with the number of modes. The contact resistance of a single-moded conductor is  $\sim 12.9 k\Omega$  which is certainly not negligible. This is the resistance one would measure if a single moded ballistic conductor were sandwiched

between two conductive contacts.

### General two-probe Landauer formula

The total current flow  $dI_S$  in a small energy interval  $dE$  through the system is given by the current injected into the wires by reservoirs multiplied by the transmission coefficient  $T = \sum_{i,j} |t_j^{(i)}|^2$ . Thus,

$$dI_S = dI_{in}^{(i)} \sum_{i,j} |t_j^{(i)}|^2 \quad (2.34)$$

$$G = \frac{2e^2}{h} \sum_{i,j} |t_j^{(i)}|^2 \quad (2.35)$$

### General four-probe Landauer formula

One can fabricate a four-probe arrangement (see Fig. 2.5) like a Hall bridge with two voltage probes located right across a scatterer. If we assume that the probes will measure the local electrochemical potentials for the  $+k$  and  $-k$  states (or some specified combination of the two) then we expect that

$$\mu_{P1} - \mu_{P2} = (1 - T)\Delta\mu$$

where  $\Delta\mu \equiv (\mu_1 - \mu_2)$ . The resistance measured in a four-probe configuration should be

$$R_{4t} = \frac{(\mu_{P1} - \mu_{P2})e}{dI_S} = \frac{h}{2e^2m} \frac{1 - T}{T} \quad (2.36)$$

If we try to apply this result we run into three separate problems.

Firstly, *mesoscopic probes are often invasive*, i.e., they change what we are trying to measure. With macroscopic conductors, the probes represent a minor perturbation. Their presence does not change the current significantly. But for a small conductor, the probes can very well be the dominant source of scattering (and hence resistance). There is no fundamental reason why a voltage probe has to be strongly coupled to the conductor. There has been some work using weakly coupled scanning tunneling probes to observe resistivity dipoles around individual scatterer and it is likely that there will be more of such non-invasive microscopic measurements as nanotechnology progresses.

Secondly, *mesoscopic probes are seldom identical* so that the two voltage probes could very well couple differently to the  $+k$  and  $-k$  states, e.g., suppose a probe were bent over to the right like P2 in Fig. 2.5 (b) then it could couple much better to  $+k$  states than to  $-k$  states. This is because a small deflection would make an electron in a  $+k$  state enter the probe but a large angle scattering is needed to make

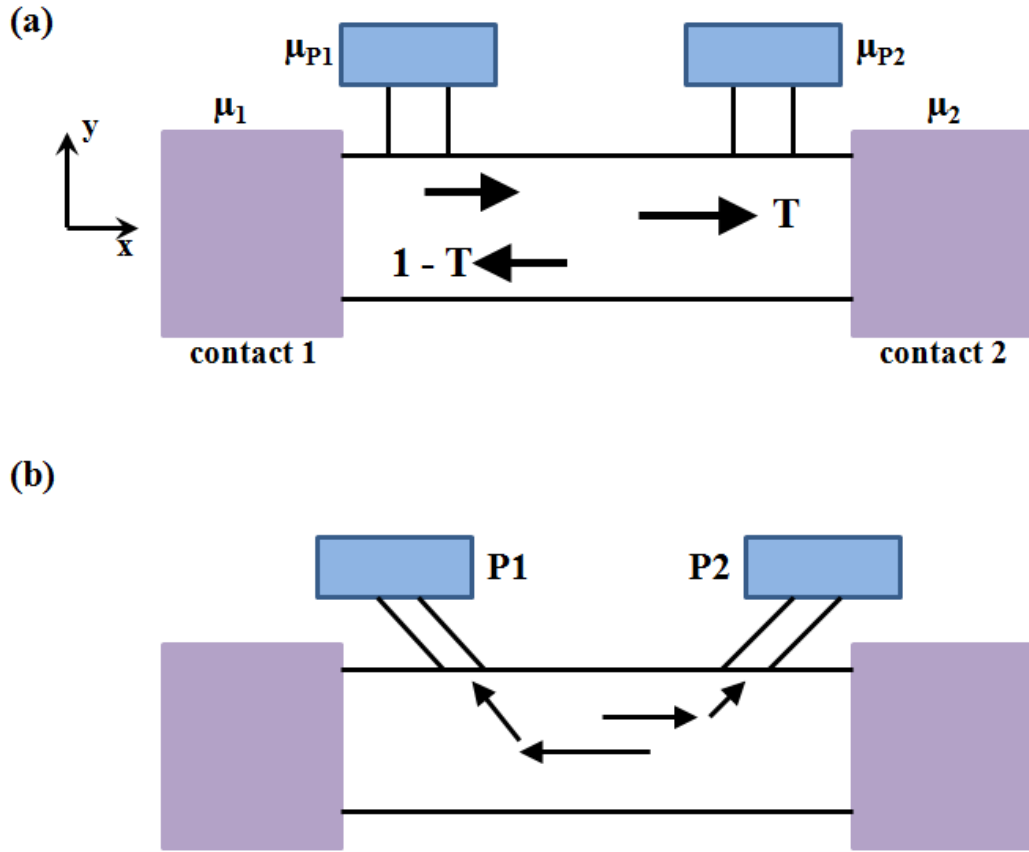


Figure 2.5: (a) A four-probe arrangement designed to measure the potential drop across a scatterer. (b) If the probes are bent as shown here they could show an apparent negative resistance if  $T > 0.5$ . Figure is taken from [6].

a  $-k$  state enter. Hence probe P2 would register a potential close to that of the  $+k$  state. Similarly, if a probe were bent over to the left like P1 in Fig. 2.5 (b) it would couple more strongly to a  $-k$  state and register a potential close to that of the  $-k$  state. In practice one has little control over the microscopic potential profiles that determine the coupling of the probes to the  $+k$  and  $-k$  states. We expect to measure the resistance given by Eq. (2.36) only if the two voltage probes couple identically to the  $+k$  and  $-k$  states noninvasively.

Finally, *mesoscopic measurements are strongly affected by quantum interference effects* unless the distance of the probes from the scatterer is much greater than the phase-relaxation length. Here we will consider a strongly reflecting scatterer with  $T \ll 1$ . In that case the electrochemical potentials for the  $+k$  and  $-k$  states are both nearly equal to one to the left of the scatterer and zero to the right of the scatterer. We would expect that a probe to the left of a scatterer should measure a potential of approximately one (equal to that of the left reservoir). However, due to quantum interference it could measure any potential between zero and one depending on its

distance from scatterer. The reason is that the probe may not be able to ‘see’ the electrons from the left reservoir due to destructive interference between the incident wave and the reflected wave. As a result it could float to a potential closer to that of the *right* reservoir even though it is located to the *left* of a strongly reflecting scatterer. We can use Eq. (2.36) to describe the four terminal resistance only if such interference effects are either absent (because of a short phase relaxation length) or carefully eliminated (by averaging measurements over a wavelength or using ‘directional couplers’ to couple the probes so that they see only the  $+k$  and  $-k$  states).

The problem can be appreciated by considering a simple analogy with optics. A beam of unpolarized light is a 50-50 mixture of photons that are polarized in the  $x$ -direction and photons that are polarized in the  $y$ -direction. But so is a beam of light that is polarized at 45 degrees to the  $x$ -axis. Yet the two are very different physically and there are many experiments that can distinguish between them. One way to represent this difference is by using a density matrix:

$$\begin{bmatrix} 0.5 & 0 \\ 0 & 0.5 \end{bmatrix}$$

(unpolarized)

$$\begin{bmatrix} 0.5 & 0.5 \\ 0.5 & 0.5 \end{bmatrix}$$

(45-degree polarized)

The diagonal elements of the density matrix represent the usual distribution function while the off-diagonal elements represent phase-correlations. For unpolarized light, the  $x$ - and  $y$ - polarizations are uncorrelated so that the off-diagonal elements are zero. For 45-degree polarized light the off-diagonal elements are as large as the diagonal ones due to the perfect phase correlation between the  $x$ - and  $y$ - polarizations.

We have an analogous situation in phase-coherent conductors with  $+k$  and  $-k$  states playing the role of  $x$ - and  $y$ - polarizations. The distribution function only give us the diagonal elements. The rest of the story is contained in the off-diagonal elements which cannot be neglected unless the phase-relaxation length is much shorter than the other length scales.

We will now describe an approach that was developed by Büttiker following the work of Engquist and Anderson [42], which allows us to describe multi-terminal phase coherent conductors directly in terms of measured currents and voltages, com-

pletely ignoring any questions regarding the internal state of the conductor.

### 2.2.2 Büttiker Formula

Since 1985 many mesoscopic experiments have been conducted using miniature Hall bridges fabricated on both metallic and semiconducting samples. However, because of the reasons mentioned above, for a while there was a serious confusion about how such four-terminal measurements should be interpreted. Indeed there was no agreement regarding the two-terminal resistance either, primarily because the importance of the contact resistance in this context was not recognized.

Büttiker found a simple and elegant solution to this problem. He noted that since there is really no qualitative difference between the current and voltage probes, one could treat all the probes on an equal footing and simply extend the two-terminal linear response formula

$$I_S = \frac{2e}{h} \bar{T} [\mu_1 - \mu_2]$$

by summing over all terminals (indexed by  $p$  and  $q$ ) as follows

$$I_{Sp} = \frac{2e}{h} \sum_q [\bar{T}_{q \leftarrow p} \mu_P - \bar{T}_{p \leftarrow q} \mu_P].$$

We can rewrite this in the form (with  $V = \mu e$ )

$$I_{Sp} = \sum_q [G_{qp} V_p - G_{pq} V_q] \quad (2.37)$$

where

$$G_{pq} \equiv \frac{2e^2}{h} \bar{T}_{p \leftarrow q} \quad (2.38)$$

The arrows in the subscripts have been inserted just as a reminder that the electron transfer is backwards from the second subscript to the first one.

The coefficients  $G$  in Eqs. (2.37, 2.38) must satisfy the following ‘sum rule’, regardless of the detailed physics, in order to ensure that the current is zero when all the potentials are equal:

$$\sum_q G_{qp} = \sum_q G_{pq} \quad (2.39)$$

This allows to rewrite Eq. (2.37) in an equivalent form

$$I_{Sp} = \sum_q G_{pq} [V_p - V_q] \quad (2.40)$$

The conductance coefficients ( $G$ ) also obey the relation as follows (where  $B$  is the

magnetic field)

$$[G_{qp}]_{+B} = [G_{pq}]_{-B} \quad (2.41)$$

Unlike the sum rule in Eq. (2.41), there is no simple reason why this relation has to be true regardless of the detailed physics. To prove this, one needs to assume a particular model for the transport. Experimentally, however, there is no evidence that this relation is ever violated (in the linear transport regime) regardless of the nature of the transport.

A couple of comments here arise: firstly, we note that the potential  $V_P$  at a voltage probe can be rewritten from Eq. (2.40) as (setting  $I_P = 0$ )

$$V_P = \frac{\sum_{q \neq P} G_{Pq} V_q}{\sum_{q \neq P} G_{Pq}}$$

This means that the potential measured at a floating terminal  $P$  is simply a weighted average of all other terminal potentials  $q$  and the weighting is determined by the conductance coefficient  $G_{Pq}$  which is proportional to transmission function from the terminal  $q$  to the floating terminal  $P$ . The shape and construction of the probes affects the measured potential through the transmission functions. Secondly, if the magnetic field is zero then the coefficients are symmetric and Eq. (2.40) is precisely what we get if we apply Kirchhoff's law to a network of conductors  $G_{qp}(=G_{pq})$  connecting every terminal  $q$  to every other terminal  $p$ . This simple resistor model, however, cannot be used in a non-zero magnetic field since the conductance coefficients ( $G$ ) are usually not symmetric, i.e.,  $G_{qp} \neq G_{pq}$ .

## 2.3 Summary

In this chapter, the basic theoretical descriptions of transport formalism of mesoscopic systems have been discussed. First we have given a brief idea about transport regime. Landauer conductance formula has been derived in detail taking an example of a mesoscopic conductor connected to electron reservoirs (contacts) by ideal leads at zero temperature. How these leads can act as quantum waveguide has been described in detail. Elastic scattering plays a very important role in electron motion. We have discussed briefly elastic scattering in time independent approach. Landauer two-probe conductance formula will be very useful to calculate conductance in multi-channel Aharonov-Bohm ring in Chapter 5 and Chapter 6.

## Chapter 3

# AHARONOV - BOHM EFFECT

*“Never underestimate the pleasure your,  
audience can receive by learning about  
something they already know.”*

–R. P. Feynman .

The description of electromagnetic phenomena can be simplified by introduction of electromagnetic potentials: scalar potential  $\phi$  and vector potential  $\vec{A}$ . To write electric and magnetic field in form of potentials is useful in Lagrangian and Hamiltonian formalism. Until the beginning of the 20th century it was widely believed that potentials are only a mathematical construct to simplify calculations and that they contain no physical significance.

With the development of quantum mechanics in the early 20th century, this view was put under question, because Schrödinger equation, basic equation of quantum mechanics, doesn't contain fields but potentials. Here the question arises: *“which description of electromagnetic phenomena is more fundamental, through electric and magnetic fields or through scalar and vector potentials?”* In 1959, Yakir Aharonov and his doctoral advisor David Bohm, proposed an experiment to address this [12]. The heart of the experiment is the effect in which wavefunction acquire some additional phase when travelling through space with no electromagnetic fields, but only potentials. This is the Aharonov-Bohm effect.

Aharonov-Bohm effect plays a very significant role in mesoscopic physics essentially because interference effects play a very crucial role there. In this chapter we give a thorough theoretical analysis of Aharonov-Bohm effect in one-dimension as this will be very useful to analyze the multi-channel rings in Chapter 5 and Chapter 6.

The Aharonov-Bohm effect [12, 13] provides a mechanism for tuning the phase of an electron wave by means of an electric or magnetic field and controls the switching

action of several proposed quantum interference devices. The magnetic Aharonov-Bohm effect has been clearly demonstrated in metal rings and cylinders [11, 48] and with much larger amplitude in 2-DEG rings [49, 50, 51, 52, 53].

### 3.1 Aharonov - Bohm Effect in Open One Dimensional Ring

Now we will discuss the basic elastic scattering problem of a one-dimensional ring pierced by a magnetic flux through the centre and connected to two electron reservoirs via perfect leads (quantum wires) in both sides. The system described in Fig. 3.1 represents an open system. On the left of this system there is source reservoir characterized by a well defined chemical potential  $\mu_1$ , and on the right there is drain reservoir characterized by chemical potential  $\mu_2$ . The left hand electron reservoir acts as a source and the right hand electron reservoir acts as a sink of electrons and by definition, there is no phase relationship between the absorbed and emitted electrons. Electrons emitted by the reservoir propagate along the perfect lead with potential  $V = 0$  to the junction with the one-dimensional ring. At the junction, electrons are partially reflected back to the reservoir and partially transmitted along the one-dimensional ring with potential  $V \neq 0$ . Electrons in the ring will eventually reach the reservoir via the junction after some time delay. This gives rise to finite-life time broadening for the electron states in the ring. In the ring, the scattering processes are elastic. The reservoirs act as an inelastic scatterer and is a source of energy dissipation. Since the reservoirs keep the chemical potential fixed, the statistical mechanical description for this system must be based on the grand canonical ensemble. This implies that the opened and closed ring systems belong to different statistical treatments. The exact description of the system is important since the dependence of the currents versus flux has a different behavior if the chemical potential is held fixed or if the number of electrons is fixed to an even or odd number. A potential difference ( $\mu_1 - \mu_2$ ) between the source reservoir and the drain reservoir drives a transport current. Incident electrons coming from the source reservoir on the left get scattered by the ring. Division of wave front occurs at junction J1; a partial wave propagates along the upper arm of the ring and another partial wave propagates along the lower arm of the ring. These two partial waves recombine and give a transmittance that bears the signature of interference between the two partial waves along the two arms of the ring. This interference can be modified by an Aharonov-Bohm flux through the centre of the ring. Different regions are marked as I, II, III and IV.  $\alpha$  is the Aharonov-Bohm phase an electron picks up in region II and  $\beta$  is that in region III. J1 is the junction where the regions I, II and III meet and J2 is the junction where the regions II, III and IV meet. The

current injected by the reservoir into the lead attached to it around the small energy interval  $dE$  is given by

$$dI_{in} = ev(dn/dE)f(E)dE. \quad (3.1)$$

Here  $v = \hbar k/m$  is the velocity of the electrons at the energy  $E$ .  $(dn/dE) = 1/(e\pi\hbar v)$  is the density of states in the perfect leads (wire), and  $f(E)$  is the Fermi distribution being 1 at  $T = 0$ . The total current flow  $dI_S$  in a small energy interval  $dE$  through the system is given by the current injected into the wires by reservoirs multiplied by the transmission coefficient  $|t|^2$  which is given by

$$dI_S = dI_{in}|t|^2. \quad (3.2)$$

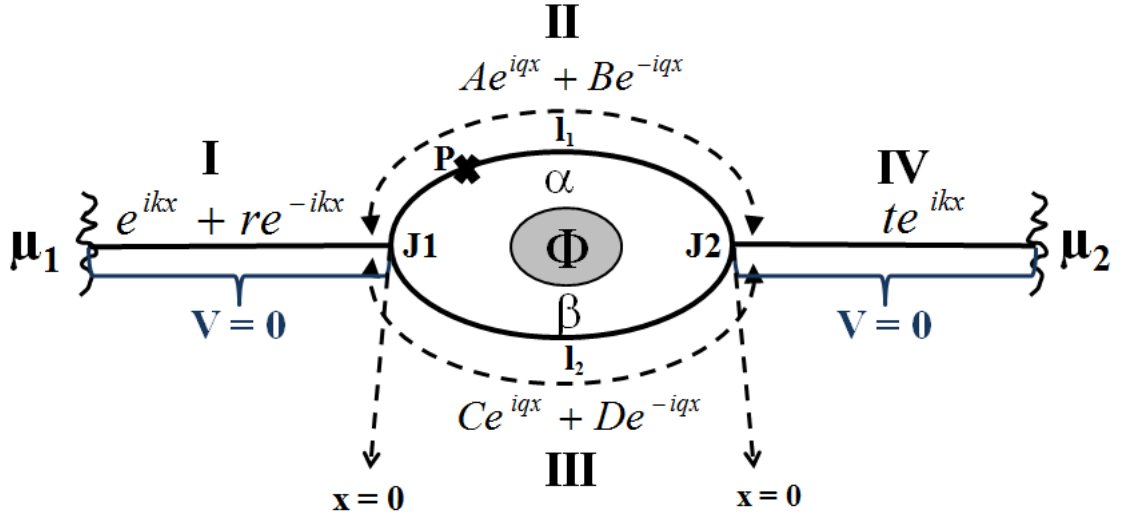


Figure 3.1: Schematic diagram of a quantum ring made up of normal metal or semiconductor in one dimension. The ring is attached to perfect leads (quantum wire) in both sides. On the left there is source reservoir having chemical potential greater than the chemical potential of the drain reservoir. Current will flow from source to drain. The wave functions of the electron in different regions have been shown in the figure at their respective places.

The Schrödinger equation for this system is given by

$$\left[-\frac{\hbar^2}{2m} \frac{\partial^2 \psi(x)}{\partial x^2} + V(x)\right] \psi(x) = E\psi(x) \quad (3.3)$$

The wave function in region I of the system described in Fig. 3.1 is given by

$$\psi_I = e^{ikx} + re^{-ikx},$$

where  $r$  is the reflection amplitude. The wave function in region IV of the system described in Fig. 3.1 is given by

$$\psi_{IV} = te^{ikx},$$

where  $t$  is the transmission amplitude.  $k$  is the wave vector given by  $k = \sqrt{\frac{2mE}{\hbar^2}}$ . The wave function in region II of the quantum ring is given by

$$\psi_{II} = Ae^{iqx} + Be^{-iqx},$$

where  $A$  and  $B$  are the amplitudes and  $q$  is the wave vector in the quantum ring. The wave function in region III of the quantum ring is given by

$$\psi_{III} = Ce^{iqx} + De^{-iqx},$$

where  $C$  and  $D$  are the amplitudes and  $q$  is the wave vector in the quantum ring. The magnetic flux is restricted to the shaded region of radius  $r_0$  at the centre of the ring and is given by

$$\phi = \int_s \vec{B} \cdot d\vec{s}$$

or,  $\phi = \int_s (\vec{\nabla} \times \vec{A}) \cdot d\vec{s}$ , since  $\vec{B} = \vec{\nabla} \times \vec{A}$ . Now using Stoke's theorem:

$$\phi = \oint \vec{A} \cdot d\vec{x}$$

or,

$$\phi = AL,$$

where  $L$  is the total length of the ring.

$$A = \frac{\phi}{L} = \frac{B \cdot \pi r_0^2}{2\pi r}, \quad (3.4)$$

and  $\vec{A} = A\hat{x}$  That means for  $r > r_0$ ,  $B = 0$  but  $\vec{A}$  is non zero and its magnitude decay as  $\frac{1}{r}$ .

Therefore for the electrons in the one-dimensional ring the Schrödinger equation is

$$\left[ \frac{1}{2m} \left( \vec{p} - \frac{e}{c} \vec{A} \right)^2 + V(x) \right] \psi(x) = E\psi(x) \quad (3.5)$$

or,

$$\frac{1}{2m} \left( \vec{p} - \frac{e}{c} \vec{A} \right)^2 \psi(x) = [E - V(x)] \psi(x) \quad (3.6)$$

Applying Gauge transformation (since  $\vec{\nabla} \times \vec{\nabla}\chi$  is 0 for any arbitrary scalar function  $\chi$ , adding  $\vec{\nabla}\chi$  to  $\vec{A}$  does not change  $\vec{B}$ . However an appropriate phase factor is to

be added to the wave function.):

$$\left[\frac{1}{2m}\left(\vec{p} - \frac{e}{c}(\vec{A} - \vec{\nabla}\chi)\right)^2\right]\psi(x)e^{-\frac{ie}{\hbar c}\int\vec{\nabla}\chi\cdot d\vec{x}} = [E - V(x)]\psi(x)e^{-\frac{ie}{\hbar c}\int\vec{\nabla}\chi\cdot d\vec{x}}$$

Since  $\vec{\nabla}\chi$  is arbitrary, we have taken  $\vec{A} = \vec{\nabla}\chi$ . or,

$$\frac{1}{2m}[\vec{p}]^2\psi(x)e^{-\frac{ie}{\hbar c}\int\vec{A}\cdot d\vec{x}} = [E - V(x)]\psi(x)e^{-\frac{ie}{\hbar c}\int\vec{A}\cdot d\vec{x}}$$

or,

$$\frac{1}{2m}[\vec{p}]^2\psi'(x) = [E - V(x)]\psi'(x) \quad (3.7)$$

where,

$$\psi'(x) = \psi(x)e^{-\frac{ie}{\hbar c}\int\vec{A}\cdot d\vec{x}} \quad (3.8)$$

The phase factors in the wavefunctions can be justified as follows where we substitute Eq. (3.8) in Eq. (3.7)

First we will evaluate LHS of the Eq. (3.7)

$$\begin{aligned} \vec{p}\psi'(x) &= \vec{p}[\psi(x)e^{-\frac{ie}{\hbar c}\int\vec{A}\cdot d\vec{x}}] \\ &= \frac{\hbar}{i}\frac{d}{dx}[(\psi(x)e^{-\frac{ie}{\hbar c}\int\vec{A}\cdot d\vec{x}})] \\ &= [\vec{p}\psi(x)]e^{-\frac{ie}{\hbar c}\int\vec{A}\cdot d\vec{x}} - (e\vec{A}/c)\psi(x)e^{-\frac{ie}{\hbar c}\int\vec{A}\cdot d\vec{x}} \end{aligned}$$

We can get Eq. (3.5) in the following way starting from Eq. (3.7)

$$\frac{1}{2m}[\vec{p}]^2\psi'(x) = [E - V(x)]\psi'(x)$$

or,

$$\begin{aligned} \frac{1}{2m}[\vec{p}^2\psi(x)e^{-\frac{ie}{\hbar c}\int\vec{A}\cdot d\vec{x}} - 2\left(\frac{e\vec{A}}{c}\right)\vec{p}\psi(x)e^{-\frac{ie}{\hbar c}\int\vec{A}\cdot d\vec{x}} \\ - \left(\frac{e\vec{A}}{c}\right)\psi(x)e^{-\frac{ie}{\hbar c}\int\vec{A}\cdot d\vec{x}}\left(-\frac{ie}{\hbar c}\right)\vec{A}\frac{\hbar}{i}] \\ = [E - V(x)]\psi(x)e^{-\frac{ie}{\hbar c}\int\vec{A}\cdot d\vec{x}} \end{aligned} \quad (3.9)$$

or,

$$\frac{1}{2m}[\vec{p}^2\psi(x) - \frac{2e\vec{A}}{c}\vec{p}\psi(x) + \frac{e^2A^2}{c^2}\psi(x)]e^{-\frac{ie}{\hbar c}\int\vec{A}\cdot d\vec{x}} = [E - V(x)]\psi(x)e^{-\frac{ie}{\hbar c}\int\vec{A}\cdot d\vec{x}}$$

$$\frac{1}{2m}\left[\vec{p} - \frac{e\vec{A}}{c}\right]^2\psi(x)e^{-\frac{ie}{\hbar c}\int\vec{A}\cdot d\vec{x}} = [E - V(x)]\psi(x)e^{-\frac{ie}{\hbar c}\int\vec{A}\cdot d\vec{x}}$$

Cancelling  $e^{-\frac{ie}{\hbar c} \int \vec{A} \cdot d\vec{x}}$  from both sides we get

$$\frac{1}{2m} \left[ \vec{p} - \frac{e\vec{A}}{c} \right]^2 \psi(x) = [E - V(x)] \psi(x)$$

So instead of solving Eq. (3.7) we can solve the following equation

$$-\frac{\hbar^2}{2m} \frac{\partial^2 \psi'(x)}{\partial x^2} = [E - V(x)] \psi'(x)$$

$$-\frac{\hbar^2}{2m} \frac{\partial^2 \psi'(x)}{\partial x^2} = q^2 \psi'(x)$$

where,  $q^2 = E - V(x)$ . It is a second order differential equation, thus its general solution can be written as:  $\psi'(x) \approx e^{iqx}$  We know,

$$\psi'(x) = \psi(x) e^{-\frac{ie}{\hbar c} \int \vec{A} \cdot d\vec{x}}$$

Or,

$$\psi(x) e^{-\frac{ie}{\hbar c} \int \vec{A} \cdot d\vec{x}} = e^{iqx}$$

$$\psi(x) = e^{iqx} \cdot e^{\frac{ie}{\hbar c} \int_0^L \vec{A} \cdot d\vec{x}} \quad (3.10)$$

Now we have to match the solution at J1 and J2.

According to Feynman path approach the amplitude of the electron wavefunction at an arbitrary point P in the one dimensional quantum ring described in Fig. 3.1 is the sum of amplitudes of the electron arriving at P along all possible classical paths. Thus using Feynman path approach we get the wave function at P in region II (whose coordinate is  $x$ ) is given by

$$\begin{aligned} \psi_{II}^P &= 1t' e^{iqx + \frac{ie}{\hbar c} \vec{A}x} + 1t' e^{iql_1 + i\alpha} r' e^{-iqx} e^{\frac{ie\vec{A}}{\hbar c}(x-l_1)} \\ &+ 1t' e^{iql_1 + i\alpha} r' e^{-iq(-l_1) - i\alpha} r'' e^{iqx} e^{\frac{ie\vec{A}}{\hbar c}x} \\ &+ 1t' e^{iql_1 + i\alpha} r' e^{-iq(-l_1) - i\alpha} r'' e^{iql_1 + i\alpha} r' e^{-iqx} e^{\frac{ie\vec{A}}{\hbar c}(x-l_1)} + \dots = 0 \end{aligned} \quad (3.11)$$

where  $t'$  is the transmission amplitude from region I to region II,  $r'$  is the reflection amplitude in region II at junction J2,  $r''$  is the reflection amplitude in region II at junction J1. Let us consider one particular term in Eq. (3.11), i.e.,  $1t' e^{iql_1 + i\alpha} r' e^{-iq(-l_1) - i\alpha} r'' e^{iqx} e^{\frac{ie\vec{A}}{\hbar c}x}$ . The incident wave function  $e^{ikx}$  at junction J1 ( $x = 0$ ) is  $e^{ik0} = 1$ . Now  $1t'$  is transmitted from region I to region II across junction J1.  $1t' e^{iql_1 + i\alpha}$  is transmitted from junction J1 to junction J2 along region II. Here  $\alpha = \frac{e}{\hbar c} \int_0^{l_1} \vec{A} \cdot d\vec{x} = \frac{e}{\hbar c} A l_1$ .  $1t' e^{iql_1 + i\alpha} r'$  is reflected back to region II at junction J2.  $1t' e^{iql_1 + i\alpha} r' e^{-iq(-l_1) - i\alpha}$  is transmitted from junction J2 to junction J1 along the region II.  $1t' e^{iql_1 + i\alpha} r' e^{-iq(-l_1) - i\alpha} r''$  is reflected from junction J1 back to region II. Now this propagates from J1 to arbitrary point P and picks up a phase  $e^{iqx} e^{\frac{ie\vec{A}}{\hbar c}x}$

Therefore,

$$\begin{aligned}\psi_{II}^P &= e^{iqx} e^{\frac{ie\bar{A}}{\hbar c}x} (it' + it'e^{iql_1+i\alpha} r' e^{iql_1-i\alpha} r'' + \dots) \\ &+ e^{-iqx} e^{\frac{ie\bar{A}}{\hbar c}(x-l_1)} (1t'e^{iql_1+i\alpha} r' + 1t'e^{iql_1+i\alpha} r' e^{-iq(-l_1)-i\alpha} r'' e^{iql_1+i\alpha} r' + \dots)\end{aligned}$$

It can be written as

$$\psi_{II}^P = A e^{iqx} e^{\frac{ie\bar{A}}{\hbar c}x} + B e^{-iqx} e^{\frac{ie\bar{A}}{\hbar c}(x-l_1)}$$

where

$$A = (it' + it'e^{iql_1+i\alpha} r' e^{iql_1-i\alpha} r'' + \dots)$$

and

$$B = (1t'e^{iql_1+i\alpha} r' + 1t'e^{iql_1+i\alpha} r' e^{-iq(-l_1)-i\alpha} r'' e^{iql_1+i\alpha} r' + \dots).$$

Therefore,  $\psi_{II}^P$  at  $x = 0$ , i.e.,  $\psi_{II}^P(0)$  is given by

$$\psi_{II}^P(0) = A + B e^{-\frac{ie\bar{A}l_1}{\hbar c}} = A + B e^{-i\alpha}$$

$\psi_{II}^P$  at  $x = l_1$ , i.e.,  $\psi_{II}^P(l_1)$  is given by

$$\psi_{II}^P(l_1) = A e^{iql_1 + \frac{ie\bar{A}l_1}{\hbar c}} + B e^{-iql_1} = A e^{i\alpha + iql_1} + B e^{-iql_1}$$

The boundary conditions are due to single valuedness of the wave function and conservation of the current. Here at junctions J1 and J2 we take

$$\psi_I(0) = \psi_{II}(0) = \psi_{III}(0)$$

$$\psi_{II}(l_1) = \psi_{III}(l_2) = \psi_{IV}(0)$$

From this we get

$$A + B e^{-i\alpha} - r = 1 \quad (3.12)$$

$$C e^{i\beta + iql_2} + D e^{-iql_2} - r = 1 \quad (3.13)$$

$$A e^{i\alpha + iql_1} + B e^{-iql_1} - t = 0 \quad (3.14)$$

$$C + D e^{-i\beta} - t = 0 \quad (3.15)$$

There are two more equations due to Kirchhoff's law. Now Kirchhoff's law at the junction can be formulated as follows.

In one dimension, the Schrödinger's equation is

$$\left[-\frac{\hbar^2}{2m} \frac{\partial^2 \psi(x)}{\partial x^2} + V(x)\right] \psi(x) = E\psi(x)$$

Or

$$-\frac{\hbar^2}{2m} \nabla^2 \psi(x) + V(x)\psi(x) = E\psi(x)$$

$$-\frac{\hbar^2}{2m} \int_{V'} \nabla^2 \psi(x) dV' + \int_{V'} V(x)\psi(x) dV' = \int_{V'} E\psi(x) dV'$$

Here  $V'$  is a small volume enclosed by a surface  $S'$ , enclosing the junction J1.

$$-\frac{\hbar^2}{2m} \int_{V'} \vec{\nabla} \cdot \vec{\nabla} \psi(x) dV' + \int_{V'} V(x)\psi(x) dV' = \int_{V'} E\psi(x) dV'$$

$$\lim_{V' \rightarrow 0} \int_{S'} \vec{\nabla} \psi(x) \cdot d\vec{S}' + \lim_{V' \rightarrow 0} \int_{V'} V(x)\psi(x) dV' = \lim_{V' \rightarrow 0} \int_{V'} E\psi(x) dV'$$

Now

$$\lim_{V' \rightarrow 0} \int_{V'} V(x)\psi(x) dV' = 0$$

as the  $V'$  is shrinking to 0 and

$$\lim_{V' \rightarrow 0} \int_{V'} E(x)\psi(x) dV' = 0$$

Therefore it follows that

$$\int_{S'} \vec{\nabla} \psi(x) \cdot d\vec{S}' = 0$$

Another boundary condition is  $\sum_i \frac{d\psi_i}{dx_i} = 0$ . For the partial waves the integration becomes a sum and we can write

$$-iqA + iqBe^{-i\alpha} + iqCe^{i\beta+iql_2} - iqDe^{-iql_2} - ikr = -ik \quad (3.16)$$

$$iqAe^{iql_1+i\alpha} - iqBe^{-iql_1} - iqC + iqDe^{-i\beta} - ikt = 0 \quad (3.17)$$

We will solve Eqs. (3.12 - 3.17) by matrix inversion to calculate  $A$ ,  $B$ ,  $C$  and  $D$  which are the amplitudes in the one-dimensional ring described in Fig. 3.1 and  $r$  and  $t$  are the reflection and transmission amplitudes, respectively in the leads attached to the ring. We will generalize this theoretical analysis for open one-dimensional ring to solve the multi-channel Aharonov-Bohm ring which we will describe in Chapter 5 and in Chapter 6 also.

### 3.2 Aharonov - Bohm Effect in Closed One Dimensional Ring

Here we take a one dimensional ring pierced by magnetic field, such that the field is confined to only the grey region in Fig. 3.2 and the electrons in the ring do not feel the magnetic field. Electrons in one dimensional rings can support a current around the ring in thermodynamic equilibrium, even at zero temperature when only the many-body ground state is occupied. This current depends on the magnetic flux  $\phi$  piercing the ring and cannot decay dissipatively. It therefore flows forever even in normal conducting materials and this is why it is called persistent current. Persistent current was predicted in the early days of quantum mechanics by Hund [32] but their experimental relevance for mesoscopic systems has been recognized only much later by Büttiker, Imry and Landauer in 1983 [14]. In their paper, they suggested the existence of persistent current even in a phase coherent normal metal closed loop (e.g., ring) in the presence of Aharonov - Bohm flux  $\phi$ . The persistent

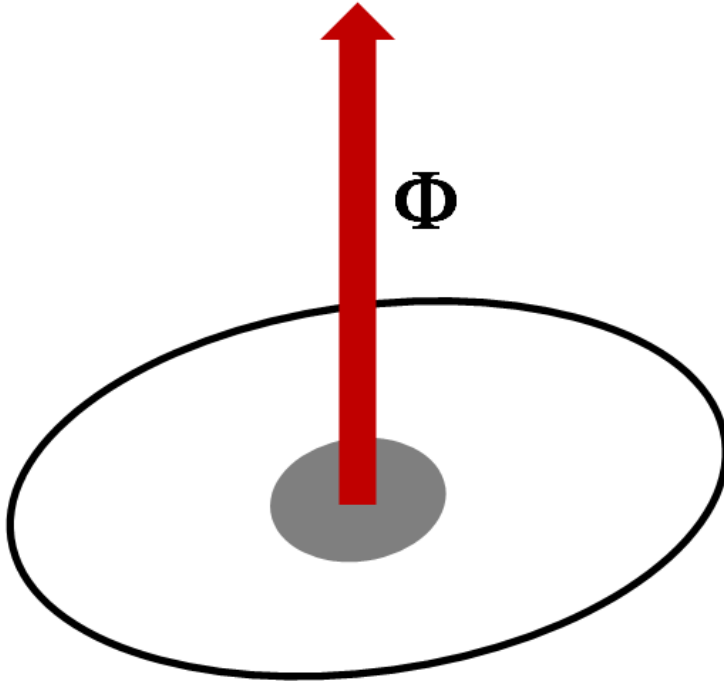


Figure 3.2: An ideal one dimensional ring of circumference  $L$  pierced by magnetic flux  $\phi$

current is given by the flux derivative of the free energy of the ring. These currents are the consequences of the sensitivity of the eigen-states to the boundary condition. Due to the enclosed magnetic field, the time reversal symmetry in the ring system is broken. As a consequence, the degeneracy between the states carrying current

clockwise and anti-clockwise directions is lifted. The persistent current is periodic in flux with periodicity  $\phi_0$ ,  $\phi_0 = hc/e$  being the flux quantum. At temperature  $T = 0$  the amplitude of the persistent current is given by  $ev_F/L$ , where  $v_F$  is the Fermi velocity and  $L$  is the circumference of the ring described in Fig. 3.2. For spinless electrons the persistent current is diamagnetic or paramagnetic depending upon whether the number of electrons are odd or even, respectively. Later experiments in diffusive as well as ballistic normal and semi-conducting rings [35, 36, 37] showed the existence of the persistent currents.

### Persistent currents in one dimensional ring

In case of a one dimensional ballistic ring of length  $L$ , threaded by an AB flux [54], the Hamiltonian is given by

$$H = \frac{1}{2m}(\vec{p} - \frac{e}{c}\vec{A})^2 \quad (3.18)$$

Thus the time independent Schrödinger equation is given by

$$\frac{\hbar^2}{2m}(-i\frac{\partial}{\partial x} - \frac{e\phi}{cL})^2\Psi_n = E_n\Psi_n \quad (3.19)$$

where,  $\Psi_n$ , are the eigen functions and  $x$  is the coordinate along the ring. For the ring geometry, we can apply periodic boundary conditions which lead to the usual quantization of energy levels. The current carried by each eigenstate can be calculated using the current operator. The total current is the sum over the individual contributions from each state, weighted with the appropriate occupation number. Following Byers and Yang [55] and Bloch [56], Cheung et al. [54] worked in a gauge for the vector potential in which the field does not appear explicitly in the Hamiltonian and the current operators, but enters the calculation via the flux modified boundary conditions,

$$\Psi(L) = \exp\left[\frac{i2\pi\phi}{\phi_0}\right]\Psi(0)$$

$$\frac{d\Psi}{dx}(x=L) = \exp\left[\frac{i2\pi\phi}{\phi_0}\right]\frac{d\Psi}{dx}(x=0)$$

The boundary conditions imply that the eigenstates and energies and hence all equilibrium physical properties of the ring are periodic in  $\phi$  with period  $\phi_0$ . This is true also in presence of disorder. A flux  $\phi \neq \phi_0 \times \text{integer}$  is mathematically equivalent to a change in the boundary conditions of the system. The corresponding eigenvalues of the ring are:

$$E_n = \frac{\hbar^2}{2mL^2}(n + \Phi)^2 \quad (3.20)$$

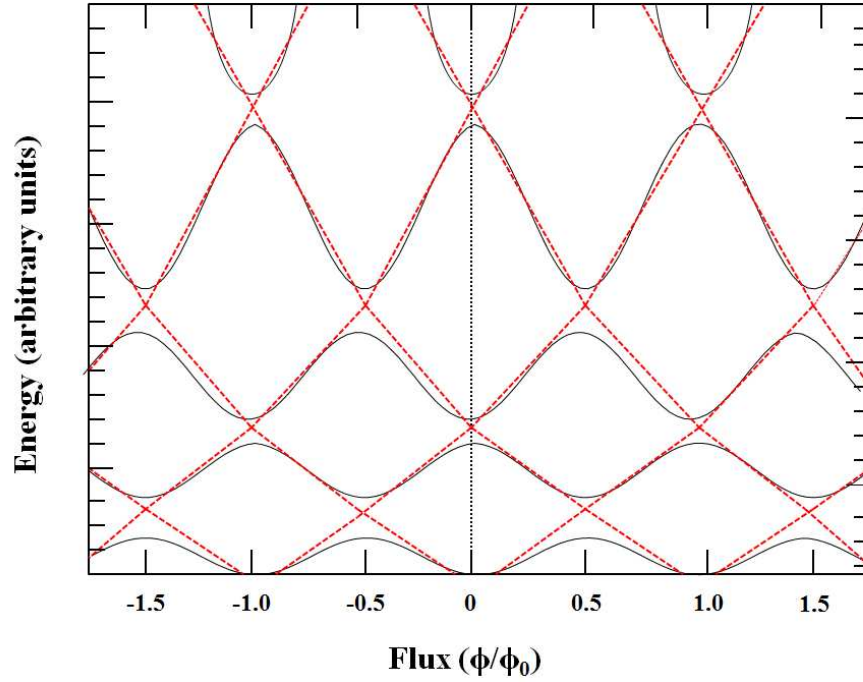


Figure 3.3: Schematic diagram of the electron energy levels as a function of the flux  $\phi/\phi_0$  in a one-dimensional ring with and without impurities (solid and dashed curves respectively). Figure is taken from [54].

wherein  $n$  takes values  $0, \pm 1, \pm 2, \dots$ . Eq. (3.20) represents the eigen energy spectra (with  $\Phi = \phi/\phi_0$ , and  $\phi_0$  is the flux quantum) of a closed normal metal ring [54]. Schematic diagram of the electron energy levels of a closed normal metal ring as a function of the flux  $\phi/\phi_0$  with and without impurities (disorder) is shown in Fig. 3.3. In the absence of impurity (disorder) in the ring, the curves form intersecting parabolas. In the presence of impurity (disorder), gaps open at the points of intersection, in the same way as band gaps form in the band structured problem. Since the band is symmetric in wave vector  $k$  for the one-dimensional lattice problem, the eigenenergies of the closed ring are symmetric in the flux. Using simple tight binding model Cheung et al. [54] showed that for one dimensional ring the persistent current decreases with the increase in impurity (disorder).

The charge current carried by the  $n^{\text{th}}$  energy level is

$$I_n = \frac{-e}{2\pi\hbar} \frac{\partial E_n}{\partial \Phi} \quad (3.21)$$

The total current of the system is then given by summation over all the occupied levels, which leads to

$$I = \sum_n I_n = -\frac{2\pi e\hbar}{mL^2} \left( n + \frac{\phi}{\phi_0} \right) \quad (3.22)$$

This persistent current (Eq. (3.22)) is obtained for dashed curves (without impuri-

ties) in the energy spectrum Fig. 3.3. For solid curves, i.e., in presence of disorder, the total current is given by

$$I = \frac{e}{\hbar} \frac{\sin \frac{2\pi\phi}{\phi_0}}{\frac{\partial}{\partial E} \text{Re}(1/t)} \quad (3.23)$$

where  $t$  is the transmission coefficient.

### 3.3 Summary

In this chapter, the detailed theoretical descriptions of Aharonov-Bohm effect have been given for both open system as well as closed system. We have discussed the basic elastic scattering problem of a one-dimensional ring pierced by a magnetic flux through the centre and connected to two electron reservoirs via perfect leads in both sides. We have solved the Schrödinger equation in detail for this system to get the wavefunctions at different regions of Fig. 3.1. Applying boundary conditions at the junctions J1 and J2 (where the ring and the leads meet) of the one-dimensional ring we got reflection amplitudes, transmission amplitudes and amplitudes in the ring. Then we have discussed one-dimensional closed ring pierced by magnetic flux at the centre. Electrons here can support a current around the ring in thermodynamic equilibrium, even at zero temperature which depends on the magnetic flux  $\phi$  piercing the ring and cannot decay dissipatively.

The current  $I$  in Eq. (3.23) is an equilibrium current quite unlike the current  $dI_{in}$  in Eq. (3.2) which is a transport current. Thus we see that in mesoscopic physics both transport current and equilibrium thermodynamic current are determined by the transmission coefficient  $t$ . So there is no clear demarkation between thermodynamic properties and linear transport properties. In fact we will show in Chapter 6 how a transport current can generate a magnetization.

# Chapter 4

## QUANTUM CAPACITANCE: A MICROSCOPIC DERIVATION

*“We shall not cease from exploration.  
And the end of all our exploring  
Will be to arrive where we started  
And know the place for the first time.”*  
—T. S. Eliot.

In this work we start from microscopic approach to many body physics and will show the analytical steps required to arrive at the concept of quantum capacitance. These approximations are valid only in the semi-classical limit and the quantum capacitance in that case is determined by Lindhard function. The effective capacitance is the geometrical capacitance and the quantum capacitance in series, and this too is established starting from a microscopic theory. Our analysis is independent of model and valid for any geometry in any dimension. However, we will use some models and systems for numerical verification, that are described in Section 4.2. Analytical derivation of quantum capacitance is given in section 4.3. Finally, this chapter is concluded with the summary of results in section 4.4.

### 4.1 Introduction

Several new concepts and ideas have been developed in last few decades on nano-electronics and they are often questioned [57]. AC response of quantum dots in the coherent regime has been measured in recent experiments [58, 59, 60, 61, 62]. A good understanding and control over such phenomenon can lead to many novel devices, specially in metrology [58, 63]. The experimental results are analyzed in a series

of works, using effective variables like quantum capacitance [63, 64, 65, 66, 67, 68]. Capacitance of mesoscopic systems are very different from geometric capacitance. In mesoscopic systems one can differentiate between electrostatic capacitance and electro-chemical capacitance. Although, in principle one can also define a magnetic field induced capacitance, in practice one defines a field dependent electrostatic or electro-chemical capacitance [69]. Ref. [70] gives a detailed analysis of electro-chemical capacitance which gives corrections to the geometrical capacitance due to field penetration into the conductor which occurs over a finite length scale comparable to the dimensions of the sample and ignored in large systems. Electro-chemical capacitance is a property of open systems (systems connected to leads and electron reservoirs). In such open systems, electron-electron interaction cannot be treated exactly and characteristic potentials were introduced to account for Coulomb interaction approximately. The correction term appear as another capacitance in series with the geometric capacitance. Both, open and closed systems can have an electrostatic voltage induced capacitance. A closed system of a finite wire (referred as stub) connected to a closed ring was analysed in Ref. [69]. The system was reduced to a two level system, wherein there is a hybridization of a single level coming from the ring. Coulomb interaction was again treated approximately with the help of characteristic potentials and single particle level approximations. Quantum corrections were again shown to appear as a capacitance that appear in series with the geometric capacitance. The quantum capacitance is given by the Lindhard function [69]. Subsequently, several authors have tried to interpret experimental data and numerical calculations in terms of quantum capacitance [71, 72]. A microscopic analysis stating under what circumstances and assumptions one can use such a parameter is not done so far.

Capacitance of a system is self consistently determined by Coulomb interactions and this is no exceptions for quantum capacitance as well. However, quantum mechanically electrons can also interact via Fermi statistics and so even when Coulomb interaction is ignored, a system can have a quantum capacitance. While geometric or classical capacitance is determined by the volume, shape and dielectric constant of the system, charge in quantum mechanics can reside in orbitals that do not have a space-time description. The existence of an effective variable of quantum capacitance, can simplify the complexity of many body physics.

Unlike that in open systems, electron-electron interaction and statistics can be treated exactly in closed systems. In this work we deal with closed systems so that an analytical proof can be given and exact numerical diagonalization is possible for verification. We would like to analyze the assumptions and concepts required to arrive at a statistical mechanical variable of electrostatic quantum capacitance. When a system is weakly coupled to a reservoir, making it an open system, one can describe the system in terms of the eigen energies of the systems and Fermi-Dirac

distribution function [73]. So our results are also valid for weakly coupled open systems. Electro-chemical potential also works by affecting the electrostatic potential inside the system [70]. So if electrostatic quantum capacitance cannot be proved then electro-chemical quantum capacitance may also not hold.

## 4.2 Model for Numerical Verification and Illustration

We have given in Fig. 4.1, schematic diagrams of a ring (Fig. 4.1(a)), a stub connected to a ring (Fig. 4.1(b)), and a 2D square geometry (Fig. 4.1(c)). Although our analysis is not restricted to these geometries, we will use them as reference and examples. Figs. 4.1 (a), 4.1 (b) and 4.1 (c) represent continuum cases whereas Figs. 4.1 (d), 4.1 (e) and 4.1 (f) represent discrete versions of the same systems as that in 4.1 (a), 4.1 (b) and 4.1 (c), respectively. Discrete models are useful for numerical analysis. The vector potential due to a magnetic field can non-trivially change the electronic state of a system (due to quantum interference) while having very little effect on the bound positive charges that can be assumed to be uniform [69]. It is very easy to see polarization due to vector potential in rings as the magnetic field can remain confined to the center of the ring while the electrons in the ring feel only the vector potential. However, it also occurs in small two dimensional or three dimensional quantum systems where weak magnetic fields have negligible effect (Lorentz's force being weighted down by the velocity of light), but vector potential will drastically change the state of the system due to interference effects. For numerical verification, we use the generalized Hubbard Hamiltonian describing a discrete system consisting of sites.

$$\begin{aligned}
 H = & \sum_{i,\sigma} \epsilon_i C_{i,\sigma}^\dagger C_{i,\sigma} + \sum_{\langle ij \rangle, \sigma} t C_{i,\sigma}^\dagger C_{j,\sigma} + \sum_i U_1 n_{i,\uparrow} n_{i,\downarrow} \\
 & + \sum_{\langle ij \rangle, \sigma, \sigma'} U_2 n_{i,\sigma} n_{j,\sigma'} \quad (4.1)
 \end{aligned}$$

where  $\epsilon_i$  is the site energy of the  $i$ th site.  $t$  is the hopping parameter (in the presence of magnetic field it becomes complex, i.e.,  $t \rightarrow t \exp[i\phi/N\phi_0]$ ).  $U_1$  and  $U_2$  are respectively, the on site and nearest neighbor Coulomb interaction.

In Fig. 4.2, we show a three dimensional ring (shaded region) with a flux  $\phi$  through the center of the ring that can cause polarization. At a particular point  $r$  on the ring we can bring an STM tip at a voltage  $V$  to cause further polarization at the position  $r$  (or  $i$ ) while another STM tip can measure the local potential  $V(r)$

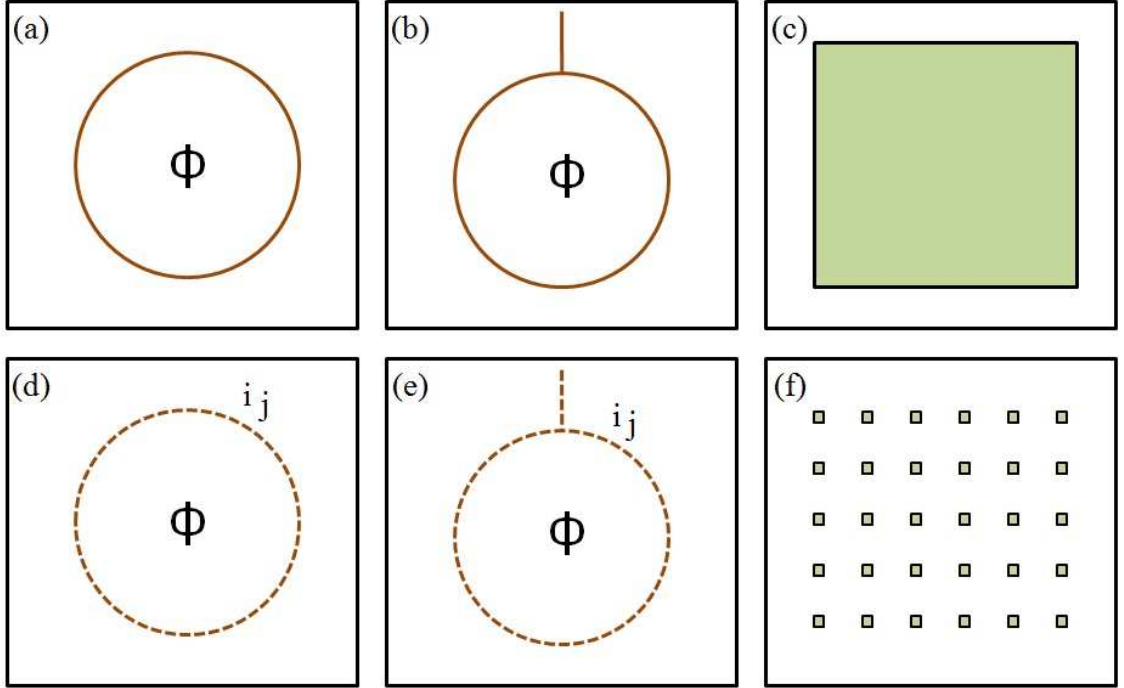


Figure 4.1: Schematic diagrams of some mesoscopic geometries used in this work as examples and also for numerical verifications. (a) represents a one-dimensional ring pierced by a magnetic flux  $\phi$ . (b) represents a one-dimensional ring to which a quantum wire or stub is attached. The ring is again pierced by a magnetic flux  $\phi$ . (c) represents a two dimensional square geometry. Once again a magnetic field can be applied perpendicular to the plane of the geometry. (d-f) is the discrete versions of those in (a), (b) and (c), respectively, that can be described by a generalized Hubbard Hamiltonian and useful for numerical verifications. The dot represents sites. Nearest neighbour sites are marked  $i$  and  $j$ .

or  $(V_i)$  at  $r$  or  $i$ . The polarization charge in a segment of the ring can be measured by a cylinder around the ring by looking at the induced charge on this cylinder (unshaded contour in Fig. 4.2).

### 4.3 Analytical Derivation

We will outline here all the mathematical steps required to describe the polarization of a quantum system in terms of electrostatic quantum capacitance. When assumptions are used, we will give numerical verification and also cite appropriate earlier works. Suppose that the potential  $V(r)$  at a point  $r$  is changed infinitesimally giving rise to a delta potential term in the Hamiltonian, of the form  $dV^{ext}(r) = \sum_n \kappa \delta(r - r_n)$ . Where  $r_n$  is the coordinate of the  $n$ th electron. The Kohn-Hohenberg theorem [74] states that the energy is an unique perturbation cor-

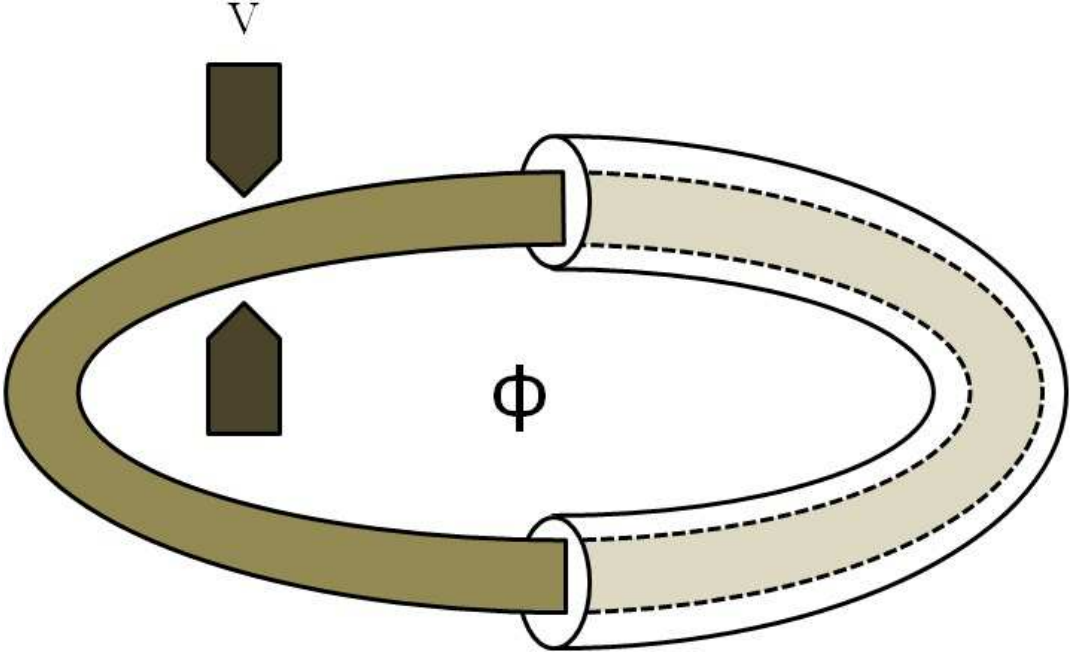


Figure 4.2: A three-dimensional mesoscopic ring pierced by a magnetic flux  $\phi$ . The flux can polarize the ring. The ring can also be polarized by a voltage probe (without making a contact) at site  $r$  at a given voltage  $V$ . Another voltage probe (without making contact) whose voltage is allowed to vary can measure the voltage at the site  $r$ . A solenoid around the ring, as shown in the figure, can measure the induced charge in a segment of the ring due to polarization. The idea of quantum capacitance is valid only when the polarized charge is uniformly distributed in the rest of the ring, apart from the region at  $r$ .

rection to the energy which is in terms of the applied potential only and no self consistency is required. So the increase in energy of the system can be expanded as

$$\Delta E = \sum_n \int d^3r_1 d^3r_2 \dots d^3r_M \psi^*(r_1, r_2, \dots, r_M) \kappa \delta(r - r_n) \psi(r_1, r_2, \dots, r_M) + O(\kappa^2) + O(\kappa^3) + \dots \quad (4.2)$$

As  $\kappa \rightarrow 0$ , then

$$\frac{\partial E}{\partial V(r)} = Q(r) \quad (4.3)$$

where

$$Q(r) = M \int d^3r_2 \dots d^3r_M \psi^*(r, r_2, \dots, r_M) \psi(r, r_2, \dots, r_M) \quad (4.4)$$

is the charge at  $r$ . We verify this numerically for all the geometries shown in Fig. 4.1. A plot is shown in Fig. 4.3 for a disordered ring whose site energies  $\epsilon_i$  vary from  $-0.5t$  to  $0.5t$ . Other parameters are explained in figure caption. We have

used a single disorder configuration as the agreement is equally same for all other configurations. The figure shows the correctness of Eq. (4.3). We stress that we use exact diagonalization using Lanczos algorithm to determine  $E$  and  $Q_i$  and hence this is a numerical verification of Eq. (4.3).

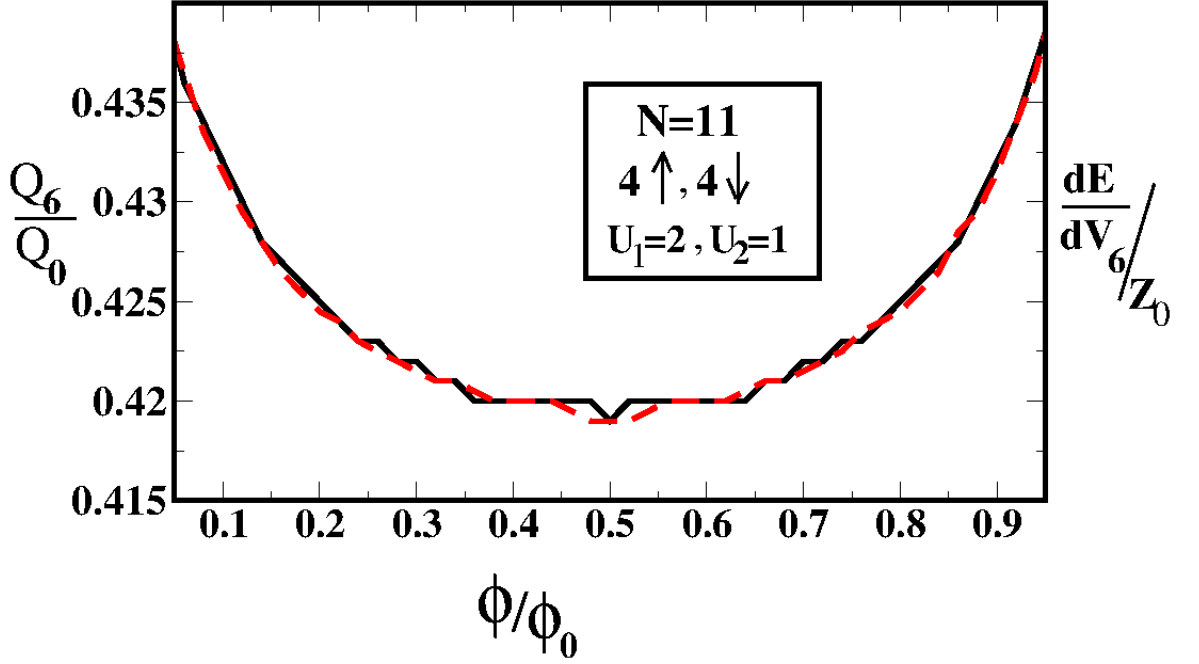


Figure 4.3: The figure shows that for the geometries shown in Fig. 4.1, the Kohn-Hohenberg theorem is valid. In this figure we have used only Fig. 4.1 (d). It consists of 11 sites ( $N = 11$ ), with 4 spin up electrons and 4 spin down electrons. The on-site Hubbard  $U_1 = 2$ , the nearest neighbour Hubbard  $U_2 = 1$ . The hopping parameter  $t = 1$ . The solid line is the charge on the 6th site as a function of the flux in units of  $Q_0$  which is just electronic charge taken to be 1. The dashed line is  $\frac{\partial E}{\partial V_6}$  in units of  $Z_0 =$  electronic charge taken as 1.  $E$  is the ground state eigen-energy of the many body system found by exact diagonalization using Lanczos algorithm. The dimension of the matrix being of the order  $10^5 \times 10^5$ . Here  $\phi_0 = hc/e$ .

Therefore, we can define a Lindhard function  $\eta(r)$ .

$$\eta(r) = -\frac{\partial Q(r)}{\partial V(r)} = -\frac{\partial^2 E}{\partial V(r)^2} \quad (4.5)$$

The last step follows from Eq. (4.3). For the geometry in Fig. 4.1 (a) or 4.1 (b) or

4.1 (d) or 4.1 (e), we can change the magnetic flux  $\phi$  through the center. This will immediately cause a redistribution of electronic charge in every site of the system. This is shown in Fig. 4.4 for the site numbered 8 in a 11 site ring. There is no qualitative difference between Fig. 4.1 (d) and 4.1 (e) even when the stub is weakly coupled to the ring. Also consider a case when an external voltage  $dV_i^{ext}$  is applied at

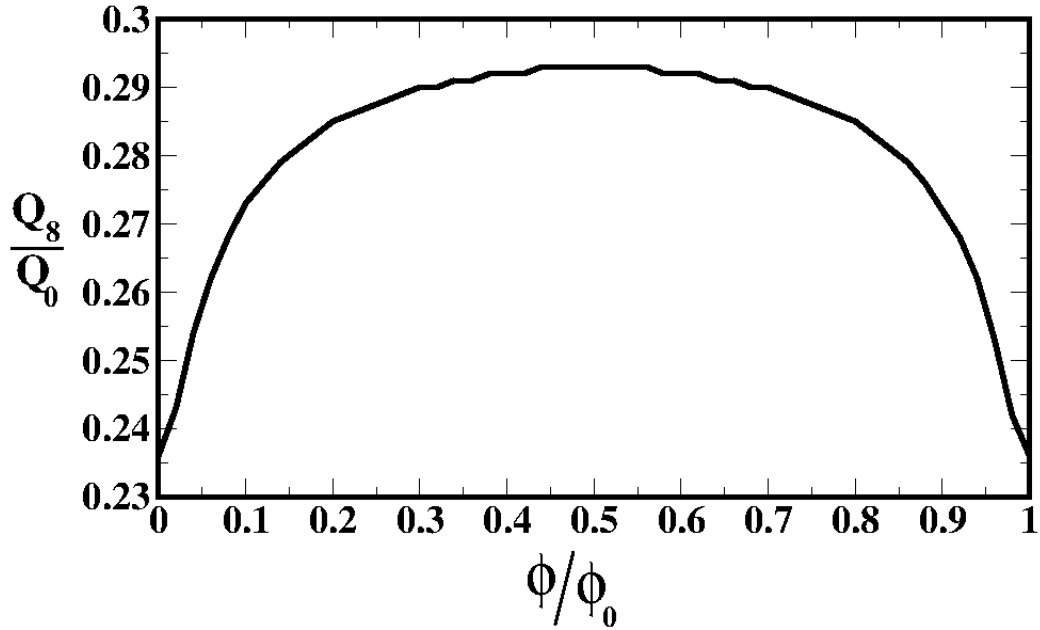


Figure 4.4: The figure shows that a mesoscopic ring can be polarized by an Aharonov-Bohm flux alone. We have used the geometry of Fig 4.1 (d) here. The graphs for other geometries is qualitatively similar and so not shown here.  $Q_8$  is the charge density at the 8th site, in units of  $Q_0$  which is electronic charge. At zero flux we expect the system to be neutral. As the flux changes, strong dispersion of  $Q_8$  suggests polarization of the system wherein the positive charge in the system can be taken to be uniform and independent of flux. Here  $\phi_0 = hc/e$ .

site  $i$  (in the discrete model one can change  $\epsilon_i$  infinitesimally as  $V_i$  and  $\epsilon_i$  are linearly related). Obviously, one can change both,  $\phi$  and  $V_i^{ext}$  simultaneously. Charge at site  $i$ ,  $Q_i$  will change. Due to electron-electron interaction the local potential, that is  $V_i$ , will change. Such a potential change will in turn have a feedback effect on charge displacement to determine  $dV_i$ . This feedback effect is a purely quantum effect as this feedback occurs because the initial charge displacement (in this case induced

by externally changed flux or potential) can change the quantum states or eigen-energies of the system. The externally applied flux and potential also work indirectly by affecting the quantum states of the system. In other words external changes give rise to electron displacements for which potential at site  $i$  (or  $j$ ), change, and this in turn gives rise to further charge displacements that is self consistently determined by Coulomb interactions and Fermi statistics.  $dV_i$  (or  $dV_j$ ) is this self consistently determined increment in potential at site  $i$  (or site  $j$ ). We can begin by writing for the discrete system

$$dQ_i = \frac{\partial Q_i}{\partial \phi} d\phi + \frac{\partial Q_i}{\partial V_i} dV_i + \sum_{j \neq i} \frac{\partial Q_i}{\partial V_j} dV_j \quad (4.6)$$

Although  $Q_i$  is a functional of  $V_i$ , one can change the potential infinitesimally at a particular point without changing the potential at any other point to define a partial derivative and this is in fact done to arrive at the concept of functional derivative [75]. Not to mention that in the standard definition for total derivatives,  $\frac{\partial Q_i}{\partial V_i}$  is changed in  $Q_i$  due to an infinitesimal test change in  $V_i$  (i.e.,  $V_i^{ext}$ ), but  $dQ_i$  on the LHS and  $dV_i$  and  $dV_j$  on the RHS are actual changes which in these systems are determined self consistently. By the virtue of the fact that we are considering a sum over  $j$  makes our treatment valid for any geometry and any dimension, where the sum over  $j$  will run over all the sites making the system. For the continuous system Eq. (4.6) becomes

$$dQ(r) = \frac{\partial Q(r)}{\partial \phi} d\phi + \frac{\partial Q(r)}{\partial V(r)} dV(r) + \int_{r' \neq r} \frac{\partial Q(r)}{\partial V(r')} dV(r') d^3 r' \quad (4.7)$$

Here partial derivatives with respect to  $V(r)$  means we are changing the potential in the region  $r$  to  $r + dr$  infinitesimally [75]. In the following we will argue analytically and numerically that

$$-\sum_{j \neq i} \frac{\partial Q_i}{\partial V_j} \approx -\sum_{j \neq i} \frac{\delta Q_i}{\delta V_j} \quad (4.8)$$

Or by replacing the sum by integration,

$$\int_{r' \neq r} \frac{\partial}{\partial V(r')} d^3 r' \approx \int_{r' \neq r} \frac{\delta}{\delta V(r')} d^3 r' \quad (4.9)$$

While LHS is a sum of partial derivatives, the RHS is a functional derivatives. Integration or sum of all (but one point) partial derivatives on LHS is approximately a total derivative. Had this one point ( $r = r'$ ) been included it would have been an exact total derivative with respect to energy (electronic charge times potential being energy) [76]. So in the above approximation an energy derivative is being replaced by a functional derivative with respect to local potential. This approximation is

known in other context like deriving the semi-classical limit of Friedel sum rule [76]. That means this approximation is valid in the semi-classical regime. Numerical verification of the approximate equality in Eq. (4.8) above is shown in Fig. 4.5. By doing exact numerical diagonalization it is difficult to go to a truly semi-classical limit of Friedel sum rule [76]. If this approximation holds then one can relate induced voltage and polarization charge through quantum capacitance as shown below. Therefore, from Eqs. (4.6) and (4.8),

$$dQ_i \approx \frac{\partial Q_i}{\partial \phi} d\phi + \frac{\partial Q_i}{\partial V_i} dV_i + \sum_{j \neq i} \frac{\delta Q_i}{\delta V_j} dV_j \quad (4.10)$$

Similarly, from Eqs. (4.7) and (4.9),

$$dQ(r) \approx \frac{\partial Q(r)}{\partial \phi} d\phi + \frac{\partial Q(r)}{\partial V(r)} dV(r) + \int_{r' \neq r} \frac{\delta Q(r)}{\delta V(r')} dV(r') d^3 r' \quad (4.11)$$

We have to assume that  $dV_j$  is independent of  $j$  as further explained below. Now it follows from charge conservation that

$$-\eta = \frac{\partial Q_i}{\partial V_i} = - \sum_{j \neq i} \frac{\delta Q_i}{\delta V_j} \quad (4.12)$$

The RHS is the net change in  $Q_i$  due to an infinitesimal functional increase (or decrease) in the potential at all points except at  $i$ . That is equivalent to not changing the potential anywhere but decreasing (or increasing) the potential at  $i$  infinitesimally. Due to charge conservation the change in charge at  $i$  will be the same in both cases. Coulomb repulsion tends to distribute charge uniformly in a system. On the other hand quantum interference effect tends to give rise to un-even distribution of charge. Assuming that in the semi-classical regime, Coulomb interaction dominate over quantum interference effects and distribute the charge uniformly,  $dV_j$  becomes independent of  $j$  and we denote it as  $dV_{rest}$ . Numerical calculations for small size quantum systems show that for an wide range of parameter space the charge distribution is uniform [77, 78]. Only in very low density regime, quantum interference effects dominate and the charge density breaks up into crests and troughs [77, 78]. Any measurement process may not be able to resolve these crests and troughs and may show an average value for the local potential implying  $dV_j$  can be taken to be independent of  $j$ . Transverse variation can be mapped to an effective variation in the longitudinal direction [79, 80]. So one can write to a linear order,

$$dQ_i = C(dV_i - dV_{rest}) \quad (4.13)$$

where  $C$  is the definition of geometric or classical capacitance. We know that when

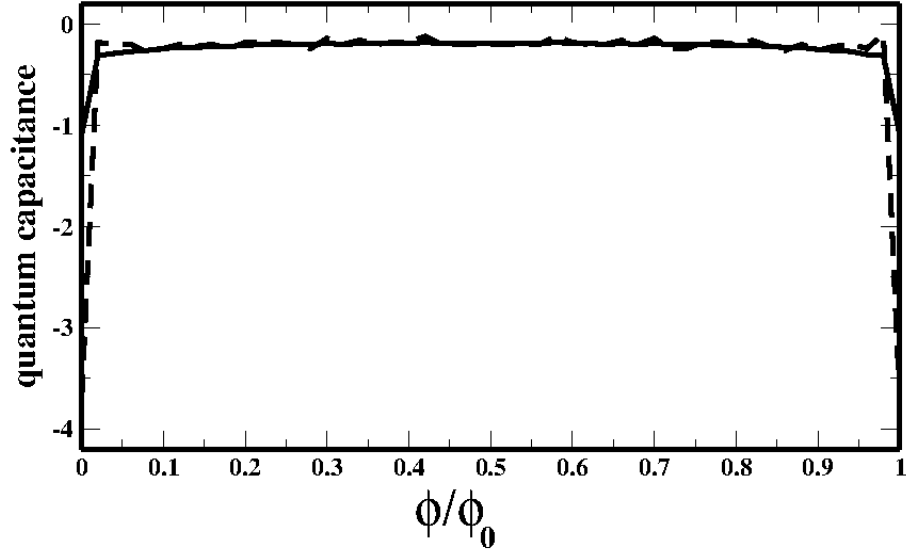


Figure 4.5: Here we are considering a ring in the semi classical limit. That is the potential in the ring varies very slowly compared to de-Broglie wavelength. In particular we have taken a 11 site ring with a single defect,  $\epsilon_1 = 0.3$  and rest of the site energies are 0. The solid line is  $\frac{\partial Q_1}{\partial V_1}$  and the dashed line is  $-\sum_{j \neq 1} \frac{\partial Q_1}{\partial V_j}$ . Both quantities are in units of electronic charge taken as 1. Here  $U_1 = 2$  and  $U_2 = 1$  with 4 spin up and 4 spin down electrons in the ring. Here  $\phi_0 = hc/e$ .

we ignore quantum interference effects (i.e., large systems without boundary and impurity effects averaged out or treated in random phase approximation) we can always get such a linear regime. Substituting Eqs. (4.12) and (4.13) in Eq. (4.10) and simplifying one gets that

$$C(dV_i - dV_{rest}) = \frac{\partial Q_i}{\partial \phi} d\phi + \frac{\partial Q_i}{\partial V_i} dV_i + \sum_{j \neq i} \frac{\delta Q_i}{\delta V_j} dV_j = \frac{\partial Q_i}{\partial \phi} d\phi - \eta dV_i + \eta dV_{rest} \quad (4.14)$$

$$(C + \eta) \frac{d(V_i - V_{rest})}{d\phi} = \frac{\partial Q_i}{\partial \phi} = \frac{\partial Q_i}{\partial V_{rest}} \frac{\partial V_{rest}}{\partial \phi} \quad (4.15)$$

Now since  $V_{rest}$  can be changed by changing  $V_i$  or  $\phi$ , one can write  $V_{rest}(\phi, V_i)$ .

Therefore,

$$dV_{rest} = \frac{\partial V_{rest}}{\partial \phi} d\phi + \frac{\partial V_{rest}}{\partial V_i} dV_i \quad (4.16)$$

Since, the region indexed  $i$  is very small compared to the rest of the system,

$$\frac{\partial V_{rest}}{\partial V_i} \rightarrow 0.$$

Therefore,

$$\frac{dV_{rest}}{d\phi} = \frac{\partial V_{rest}}{\partial \phi} \quad (4.17)$$

From Eq. (4.15) it follows that

$$(C + \eta) \frac{(dV_i - dV_{rest})}{d\phi} = \eta \frac{\partial V_{rest}}{\partial \phi} = \eta \frac{dV_{rest}}{d\phi} \quad (4.18)$$

Multiplying both sides of the above equation by  $C$  we get,

$$C \frac{(dV_i - dV_{rest})}{d\phi} = \frac{C\eta}{(C + \eta)} \frac{dV_{rest}}{d\phi} \quad (4.19)$$

or on using Eq. (4.13)

$$dQ_i = \frac{C\eta}{(C + \eta)} dV_{rest}$$

or

$$dQ_i = -dQ_{rest} = C_{eff} dV_{rest}$$

where,  $C_{eff} = \frac{C\eta}{(C+\eta)}$ . That is

$$\frac{1}{C_{eff}} = \frac{1}{C} + \frac{1}{\eta} \quad (4.20)$$

When we define capacitance we do not consider the sign of the charge. Normally one plate of the capacitor has charge  $+Q$  and the other has charge  $-Q$ , wherein we write  $Q = CV$ . Hence if we want to include quantum effects then only in the semi-classical regime we find it possible to describe polarization in terms of capacitance. A quantum capacitor of capacitance  $\eta$  in series with the classical capacitance determines the effective capacitance of the system. The characteristic potential (or the potential difference between two parts of the ring) is determined by this effective variable. The AC response of the ring is also determined by this effective variable along with the inductance. For a purely capacitive response,  $I(t) = dQ_i/dt$  or  $dI_\omega = -i\omega C_{eff} dV_\omega$  [69]. Such an effective variable will exist only if assumptions given in Eqs. (4.3), (4.8), and (4.17) are valid. Although quantum capacitance was introduced first by Serge Luryi [81], he introduced it on very general grounds and the above relation was not obtained. The above relation was obtained only in the frame work of single particle two level system [69]. We have derived it generally for

any arbitrary system including many body effects and outlined the assumptions and regime in which such an effective variable will exist.

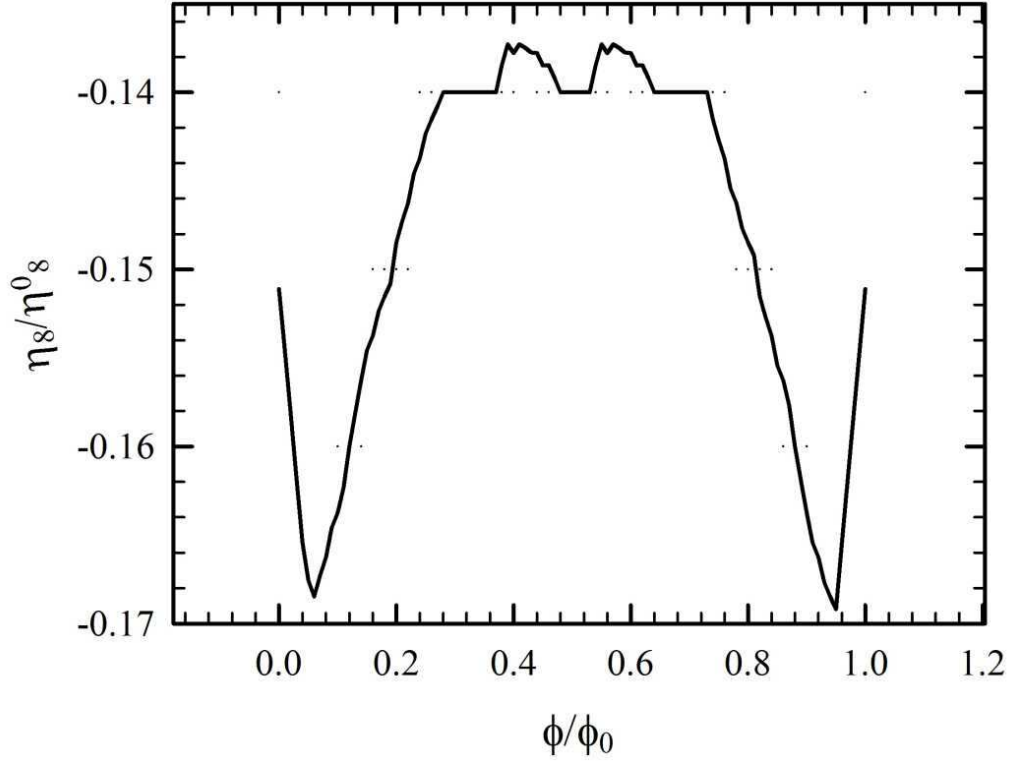


Figure 4.6: The figure shows a plot of  $\eta_8 = \partial Q_8 / \partial V_8$  as a function of flux. Here  $\eta_8^0 = e/t$  where  $e$  is electronic charge.  $\phi_0 = hc/e$ . This is for an eleven site disordered ring with site energies varying from  $-0.5t$  to  $+0.5t$ . In this case  $U_1 = 0$  and  $U_2 = 0$ . Here  $\phi_0 = hc/e$ .

In Figs. 4.6 and 4.7 we have made a comparison of quantum capacitance at site 8, i.e.,  $\eta_8$  in the non-interacting system and the interacting system to show that  $\eta$  is a good parameter to effectively capture the effect of electron-electron interactions. Here again we are considering the 11 site disordered ring considered in Figs. 4.3 and 4.4. We have applied a small external potential at the 8th site to evaluate  $\partial Q_8 / \partial V_8 = \eta_8$ . Fig. 4.6 is for the non-interacting case i.e.,  $U_1 = 0$  and  $U_2 = 0$  although the electrons still interact through Fermi statistics. In Fig. 4.7 we have made  $U_1 = 2$  with all other parameters remaining the same. There is a large qualitative as well as quantitative difference between the two figures which shows the importance of including Coulomb interaction and many body effects in defining capacitance.  $dQ_i = -dQ_{rest}$  can be measured as outlined in Fig. 4.2.  $\partial Q_i / \partial V_i = -\eta$  can also be measured as outlined in Fig. 4.2. Geometrical capacitance  $C$  is

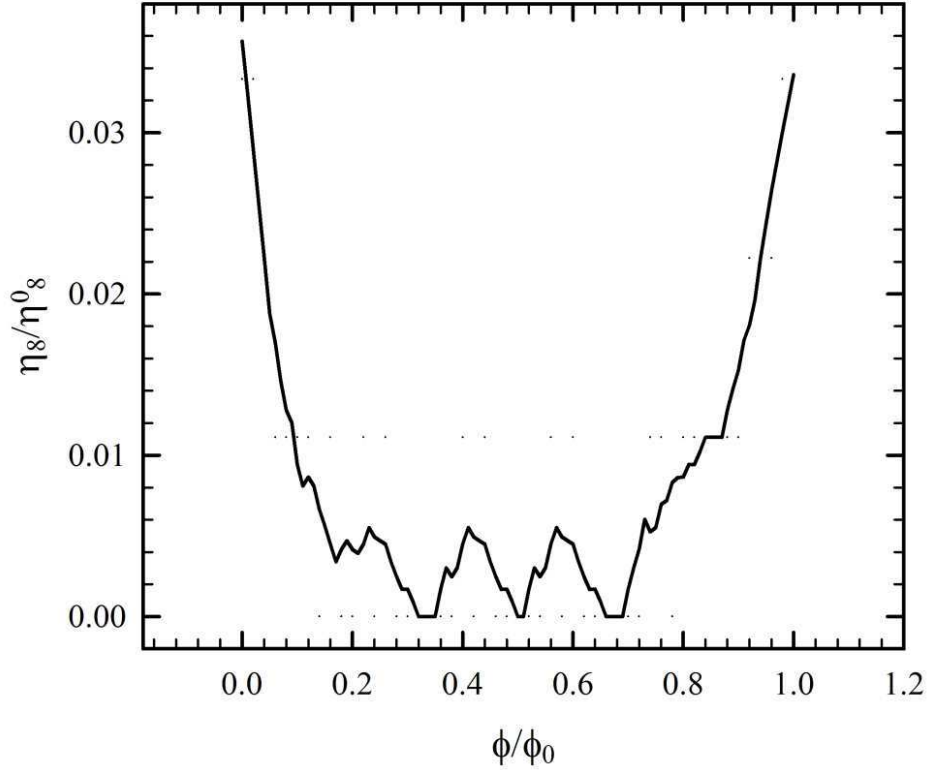


Figure 4.7: The figure shows a plot of  $\eta_8 = \partial Q_8 / \partial V_8$  as a function of flux. Here  $\eta_8^0 = e/t$  where  $e$  is electronic charge.  $\phi_0 = hc/e$ . This is for an eleven site disordered ring with site energies varying from  $-0.5t$  to  $+0.5t$ . In this case  $U_1 = 2$  and  $U_2 = 0$ . Here  $\phi_0 = hc/e$ .

independent of finite size or quantum interference effects and is known for an given sample from its bulk properties. So one can determine  $C_{eff}$ . Thus  $dV_i$  and  $d_{rest}$  can be known for any applied external potentials as  $C_{eff}$  is the single parameter that determine this.

## 4.4 Conclusion

In the semi-classical regime we prove polarization charge and induced potential of a mesoscopic isolated sample are related by an effective capacitance  $C_{eff}$ . Effective capacitance can be decoupled as a linear combination of classical capacitance and quantum capacitance. The quantum capacitance is given by the Lindhard function. In this regime, we can design quantum circuits in terms of this parameter  $C_{eff}$  just as classical circuits are built in terms of parameters like resistance, capacitance and inductance. While in earlier works, Eq. (4.20) was derived for single particle theory for a two level system, we have started from the principles of many body physics and

derived Eq. (4.20) for any arbitrary geometry in any dimension. We have shown the approximations necessary to get this in the framework of fully interacting fermions that can be described by Density Functional theory or Hartree-Fock theory. All these approximations are justified in the semi-classical limit. So Eq. (4.20) can provide a simple way to understand DC and AC response of quantum finite sized many body electronic systems in the semi-classical limit, in terms of an effective variable.

# Chapter 5

## STABLE SWITCH ACTION BASED ON QUANTUM INTERFERENCE EFFECT

*“Frequently, I have been asked if an experiment I have planned is pure or applied science, to me it is more important to know if the experiment will yield new and probably enduring knowledge about nature. If it is likely to yield such knowledge, it is in my opinion good fundamental research; and this is more important than whether the motivation is purely aesthetic satisfaction on the part of the experimenter on the one hand or the improvement of the stability of a high power transistor on the other.”*

–William B. Shockley.

Although devices working on quantum principles can revolutionize the electronic industry, they have not been achieved yet as it is difficult to control their stability, which supports Landauer’s claim that devices based on quantum interference principles cannot be achieved. In this chapter we consider a multichannel Aharonov-Bohm interferometer connected to two reservoirs of different chemical potentials to understand the quantum interference effect. In Section 5.1, we have mentioned earlier experimental as well as theoretical works as a motivation to study multichannels junctions which is very difficult to account for theoretically. In Section 5.2, we have described our model for calculation, shown theoretical analysis for a multichannel Aharonov-Bohm ring including channel mixing and evanescent modes. We have proposed a new  $S$  matrix for multichannel junctions to solve the scattering problem. In Section 5.3, using Landauer’s formula we have calculated the conductance and discussed that the operational characteristics of a quantum switch can be made independent of impurity configuration, temperature, Fermi energy etc. This chapter

is concluded with a summary of results discussed in Section 5.4.

## 5.1 Introduction

Advances in electron beam lithography within the last few years have made it possible to fabricate nano sized or mesoscopic artificial structures with good control over design parameters and probe the quantum transport properties [6]. These include very narrow quasi one-dimensional quantum wires, zero-dimensional electron systems or quantum dots, rings, etc., constructed at a semiconductor interface. Typical sizes of these systems vary between 1 to 10  $\mu\text{m}$ . At very low temperatures (typically mK), the scattering by phonons is significantly suppressed, and the phase coherence length can become large compared to the system size. In this regime the electron maintains the single particle phase coherence across the entire sample. The sample becomes an electron waveguide where the transport properties are solely determined by the impurity configuration and the geometry of the conductor and by the principles of quantum mechanics [6].

Such advances in mesoscopic structures have led to the possibility of new quantum semiconductor devices. These active quantum devices rely on quantum effects for their operation based on interferometric principles, and are quantum analog of well-known optical and microwave devices [6]. The mechanism of switch action by quantum interference is a new idea in electronic application. Several potential switching devices have been proposed, wherein one controls the relative phase difference between different interfering paths (say, in semiconducting loop structures) by applying electrostatic or magnetic fields [82, 83, 84, 85]. The possibility of achieving transistor action in T-shaped structure by varying the effective length of the vertical open ended lead has also been explored [86, 87]. Devices in which electrons carry current without being scattered either elastically or inelastically (ballistic devices) promise to be much faster and will consume less power than the conventional devices. It should also be noted that quantum devices can exhibit multifunctional property (e.g., single stage frequency multiplier) wherein the functions of an entire circuit within a single element can be performed [88]. They can also lead to tremendous down sizing of electronic devices. The conventional transistors operate in a classical diffusive regime and are not very sensitive to variations in material parameters such as dimensions or the presence of small impurities or non-uniformity in size and shape. These devices operate by controlling the carrier density of quasi-particles. However, proposed quantum devices are not very robust in the sense that the operational characteristics depend very sensitively on material parameters, impurity configuration, shape and size, temperature and Fermi energy [89]. For example, incorporation of a single impurity in the mesoscopic device can change, non-trivially, the interference of partial electron waves propagating through

the sample, and hence the electron transmission (operational characteristics) across the sample [90]. In such devices the actual problem of control and reproducibility of operating thresholds becomes highly nontrivial. These devices can be exploited if we achieve the technology that can reduce or control the phase fluctuations to a small fraction of  $2\pi$  [91]. A lot of work has been done in one dimensional quantum rings [91, 92, 93, 94, 95, 96, 97, 98, 99, 100]. However, the experimental rings are always in two dimension or in three dimension. Such systems have not received any theoretical attention because multichannel junctions are very difficult to account for theoretically. Earlier models either do not account for channel mixing or do not allow the inclusion of evanescent modes.

## 5.2 Theoretical Analysis

Fig. 5.1 represents the schematic diagram of a finite thickness mesoscopic quantum ring under consideration. It is made up of normal metal or semiconductor and electronic transport in such systems can be well described by an effective mass theory [6]. Incident electrons coming from the source reservoir on the left (say), gets scattered by the ring. Division of wave front occurs at junction J1; a partial wave propagates along the upper arm of the ring and another partial wave propagates along the lower arm of the ring. These two partial waves recombine and give a transmittance that bears the signature of interference between the two partial waves along the two arms of the ring. This interference can be modified by an Aharonov - Bohm flux through the center of the ring. The description of the figure is given in further detail in the figure caption.

The Schrödinger equation for a quasi one dimensional wire is (the third degree of freedom, i.e., z-direction, is usually frozen by creating a strong quantization [6])

$$-\frac{\hbar^2}{2m^*}\left(\frac{\partial^2\psi}{\partial x^2} + \frac{\partial^2\psi}{\partial y^2}\right) + V(x, y)\psi(x, y) = E\psi(x, y) \quad (5.1)$$

Here the  $x$  coordinate is along the wire,  $y$  coordinate is perpendicular to it,  $m^*$  is the electron effective mass and  $E$  is the electron energy. In regions I and IV (see Fig. 5.1) we have only the confinement potential. That is

$$V(x, y) = V(y).$$

Whereas in regions II and III apart from the confinement potential we take a constant potential  $V_0$  that can be used to excite evanescent modes inside the ring. That is

$$V(x, y) = V(y) + V_0.$$

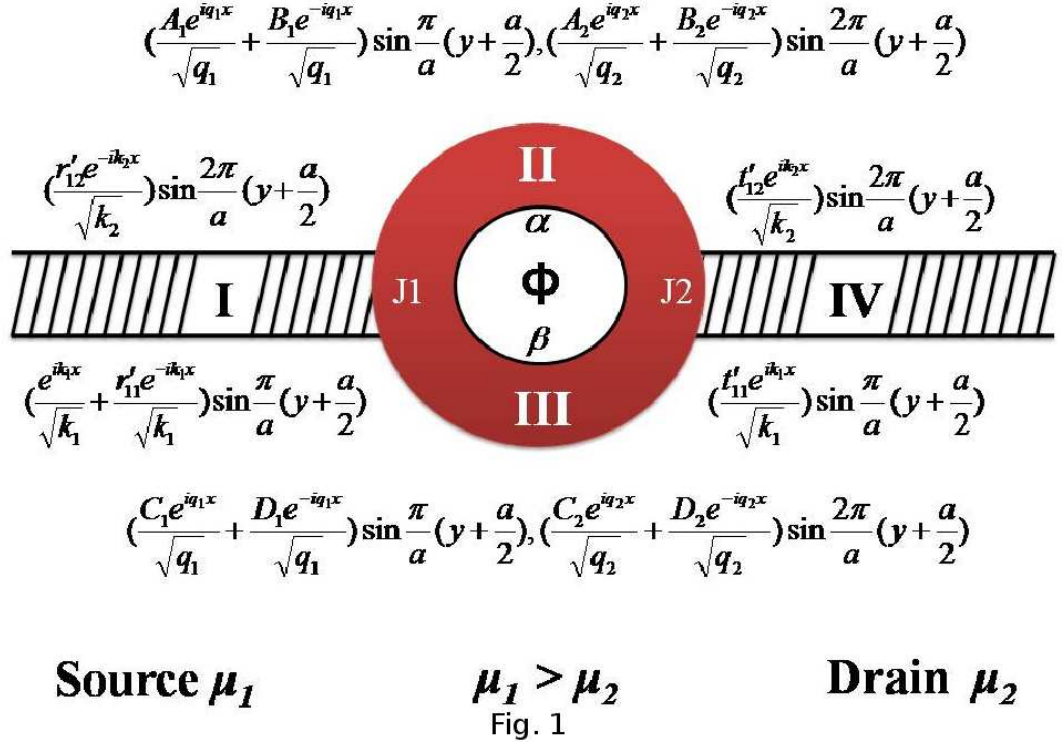


Figure 5.1: A finite thickness quantum ring of width  $a$  made up of normal metal or semiconductor is indicated by the red region. On either sides the quantum ring is attached with quantum wires made up of normal metal or semiconductor. It is indicated by the striped regions. On the left of the above system there is the source reservoir with chemical potential  $\mu_1$  and on the right there is the drain reservoir with chemical potential  $\mu_2$ . A potential difference  $(\mu_1 - \mu_2)$  between the source reservoir and the drain reservoir drives a transport current. The wave functions of the electron in different regions is shown in the figure at their respective places. Different regions are marked as I, II, III and IV. The ring is pierced by an Aharonov - Bohm flux  $\phi$ .  $\alpha$  is the Aharonov-Bohm phase an electron picks up in region II and  $\beta$  is that in region III.  $J1$  is the junction where the regions I, II and III meet and  $J2$  is the junction where the regions II, III and IV meet.

Without any loss of generality we take  $V(y)$  to be an infinite square well potential of width  $a$ . That is

$$V(y) = 0 \quad \text{for } -a/2 \leq y \leq a/2$$

and

$$V(y) = \infty \quad \text{for } |y| > a/2 \quad (5.2)$$

The wave functions in the ring can be obtained by solving Eq. (5.1) where we assume the ring to be so large compared to the de Broglie wave length that its curvature

can be neglected [101]. The length of the ring is  $L = l_1 + l_2$ , where  $l_1$  is the length of the upper arm and  $l_2$  is the length of the lower arm. The magnetic field appears just as a phase of  $\psi(x, y)$  and will be accounted for while applying the boundary conditions [54]. In regions I and IV Eq. (5.1) can be separated as

$$\psi(x, y) = \phi(x)\xi(y) \quad (5.3)$$

to give

$$-\frac{\hbar^2}{2m^*} \frac{\partial^2 \phi(x)}{\partial x^2} = \frac{\hbar^2 k^2}{2m^*} \phi(x) \quad (5.4)$$

and

$$-\frac{\hbar^2}{2m^*} \frac{\partial^2 \xi(y)}{\partial y^2} + V(y)\xi(y) = \varepsilon \xi(y) \quad (5.5)$$

Since  $V(y)$  is a square well potential of width  $a$ , Eq. (5.5) gives

$$\xi_n(y) = \sin \frac{n\pi}{a} \left( \frac{a}{2} + y \right) \quad (5.6)$$

and

$$\varepsilon_n = \frac{n^2 \pi^2 \hbar^2}{2m^* a^2} \quad (5.7)$$

Eq. (5.4) has solution of the form

$$\phi_n(x) = e^{\pm i k_n x}$$

with

$$k_n = \sqrt{\frac{2m^* E}{\hbar^2} - \frac{n^2 \pi^2}{a^2}} \quad (5.8)$$

or

$$E = \varepsilon_n + \frac{\hbar^2 k_n^2}{2m^*} \quad (5.9)$$

So wave functions in regions I and IV can be written as

$$\psi_I^{(1)} = \left( \frac{e^{i k_1 x}}{\sqrt{k_1}} + \frac{r'_{11} e^{-i k_1 x}}{\sqrt{k_1}} \right) \sin \frac{\pi}{a} \left( y + \frac{a}{2} \right) \quad (5.10)$$

$$\psi_I^{(2)} = \left( \frac{r'_{12} e^{-i k_2 x}}{\sqrt{k_2}} \right) \sin \frac{2\pi}{a} \left( y + \frac{a}{2} \right) \quad (5.11)$$

$$\psi_{IV}^{(1)} = \left( \frac{t'_{11} e^{i k_1 x}}{\sqrt{k_1}} \right) \sin \frac{\pi}{a} \left( y + \frac{a}{2} \right) \quad (5.12)$$

$$\psi_{IV}^{(2)} = \left( \frac{t'_{12} e^{i k_2 x}}{\sqrt{k_2}} \right) \sin \frac{2\pi}{a} \left( y + \frac{a}{2} \right) \quad (5.13)$$

$\psi_I^{(1)}$  is the wave function of region I in channel  $n = 1$  and so on. From Eq. (5.8),

in the first mode

$$k_1 = \sqrt{\frac{2m^*E}{\hbar^2} - \frac{\pi^2}{a^2}} \quad (5.14)$$

is the propagating wave vector and in the second mode

$$k_2 = \sqrt{\frac{2m^*E}{\hbar^2} - \frac{4\pi^2}{a^2}} \quad (5.15)$$

is the propagating wave vector. For

$$\frac{4\pi^2}{a^2} < E < \frac{9\pi^2}{a^2} \quad (5.16)$$

both  $k_1$  and  $k_2$  are real as can be seen from Eq. (5.14) and Eq. (5.15).  $k_n$  for  $n > 2$  are imaginary as can be seen from Eq. (5.8) implying that there are two propagating channels. In the leads we can not have evanescent modes [24, 27]. Now for the regions II and III the potential is  $V(x, y) = V(y) + V_0$ . Wave functions in these regions can be similarly written as

$$\psi_{II}^{(1)} = \left( \frac{A_1 e^{iq_1 x}}{\sqrt{q_1}} + \frac{B_1 e^{-iq_1 x}}{\sqrt{q_1}} \right) \sin \frac{\pi}{a} \left( y + \frac{a}{2} \right) \quad (5.17)$$

$$\psi_{II}^{(2)} = \left( \frac{A_2 e^{iq_2 x}}{\sqrt{q_2}} + \frac{B_2 e^{-iq_2 x}}{\sqrt{q_2}} \right) \sin \frac{2\pi}{a} \left( y + \frac{a}{2} \right) \quad (5.18)$$

$$\psi_{III}^{(1)} = \left( \frac{C_1 e^{iq_1 x}}{\sqrt{q_1}} + \frac{D_1 e^{-iq_1 x}}{\sqrt{q_1}} \right) \sin \frac{\pi}{a} \left( y + \frac{a}{2} \right) \quad (5.19)$$

$$\psi_{III}^{(2)} = \left( \frac{C_2 e^{iq_2 x}}{\sqrt{q_2}} + \frac{D_2 e^{-iq_2 x}}{\sqrt{q_2}} \right) \sin \frac{2\pi}{a} \left( y + \frac{a}{2} \right) \quad (5.20)$$

In these regions the energy can be similarly written as

$$E - V_0 = \frac{\hbar^2 q_n^2}{2m^*} + \frac{n^2 \pi^2 \hbar^2}{2m^* a^2}$$

or

$$q_n = \sqrt{\frac{2m^*(E - V_0)}{\hbar^2} - \frac{n^2 \pi^2}{a^2}}$$

Hence, in the first mode

$$q_1 = \sqrt{\frac{2m^*(E - V_0)}{\hbar^2} - \frac{\pi^2}{a^2}} \quad (5.21)$$

is the wave vector and in the second mode

$$q_2 = \sqrt{\frac{2m^*(E - V_0)}{\hbar^2} - \frac{4\pi^2}{a^2}} \quad (5.22)$$

is the wave vector. Depending on the choice of energy  $E$  and potential  $V_0$ ,  $q_1$  and  $q_2$  can be real (propagating mode) as well as imaginary (evanescent mode). Such evanescent states can always be excited in the internal regions of the system but not in leads [24, 27].

Note that a two dimensional quantum wire can be also converted into a Aharonov-Bohm set up as shown in Fig. 5.2. Essentially one can form a cylinder that can enclose a flux [102]. In this case all the analysis given above remains the same. For

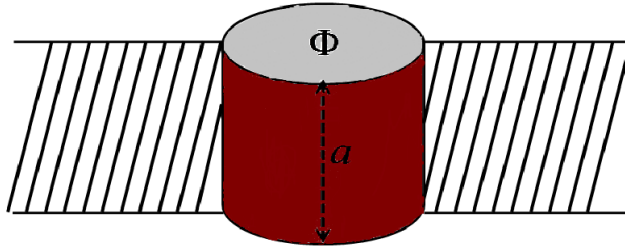


Figure 5.2: Cylindrical Aharonov-Bohm set up

example if now we choose cylindrical coordinates the wave function in Eq. (5.17) becomes

$$\psi_{II}^{(1)} = \left( \frac{A_1 e^{im_1 \theta}}{\sqrt{m_1}} + \frac{B_1 e^{-im_1 \theta}}{\sqrt{m_1}} \right) \sin \frac{\pi}{a} \left( z + \frac{a}{2} \right) \quad (5.23)$$

In fact this makes analysis much simpler because  $m_1$  stands for angular momentum and takes into account the curvature of the ring. The boundary conditions Eq. (5.29) to Eq. (5.40) (shown later) remain unchanged because replacing  $k_1$  by  $m_1$  or  $x$  by  $\theta$  or  $y$  by  $z$  do not affect boundary conditions. Advantage with this set up is that one can make width of the ring  $a$  much larger than the length of the ring  $L$ .

### $S$ - matrix for the Junction

Earlier works have proposed junction  $S$  matrix for solving the scattering problem of a ring [92, 93, 94, 95, 96, 97, 98, 99, 73, 103] where the following conditions [104]

are satisfied at the junction:

- (a) conservation of current,
- (b) continuity of wave function and
- (c) unitarity of  $S$  matrix.

However, earlier models do not account for channel mixing and also do not allow us to include evanescent modes. We give below a simple way to obtain an  $S$  matrix for a 3 legged two channel junction shown in Fig. 5.3, that satisfy the three conditions stated above. For our junction  $S$  matrix channel mixing occurs and evanescent modes can also be accounted for. The approach can be generalized to any numbers of channels. For details of the  $S$ -matrix elements for a multi-channel scattering problem see Ref. [105]. Note that the different elements of the  $S$ -matrix contain informations about the propagating modes as well as the evanescent modes arising out of transverse confinement [105].

Fig. 5.3 represents schematic diagram of a three-legged scatterer that we find at J1 or J2 of Fig. 5.1. All the legs or leads are made up of normal metal or semiconductor. Incident electrons coming from the left of the lead labeled I, gets scattered at the junction where the three leads meet. Division of wave front occurs and partial waves propagate along the upper arm labeled II and along the lower arm labeled III. The wave functions of the electron in different regions are again obtained from Eq. (5.1) and shown in their respective places for two propagating channels in each lead. Potential in region I (stripped region) is zero whereas potential in regions II and III (red colored region) is  $V_0$ . Taking the clue from reflection and transmission

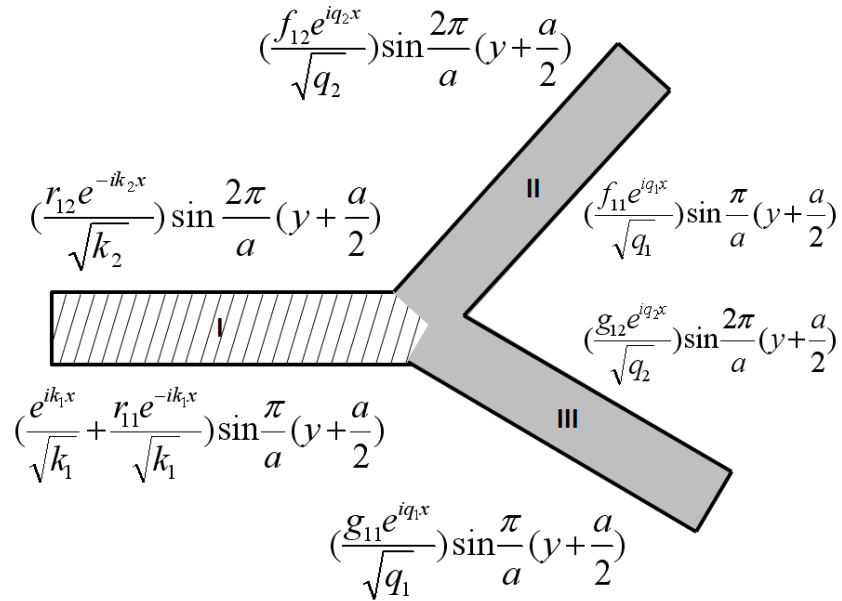


Figure 5.3: A three-legged two-channel junction that exists at J1 and J2 of Fig. 5.1.

amplitudes for a one dimensional step potential [106] we can write for the different reflection amplitudes  $r_{mn}$  and transmission amplitudes  $f_{mn}$  and  $g_{mn}$  shown in Fig. 5.3 as

$$\begin{aligned}
r_{11} &= \left( \frac{k_1 - k_2 - 2q_1 - 2q_2}{k_1 + k_2 + 2q_1 + 2q_2} \right) \\
r_{12} &= \left( \frac{2\sqrt{k_1 k_2}}{k_1 + k_2 + 2q_1 + 2q_2} \right) \\
f_{11} = g_{11} &= \left( \frac{2\sqrt{k_1 q_1}}{k_1 + k_2 + 2q_1 + 2q_2} \right) \\
f_{12} = g_{12} &= \left( \frac{2\sqrt{k_1 q_2}}{k_1 + k_2 + 2q_1 + 2q_2} \right) \\
r_{22} &= \left( \frac{k_2 - k_1 - 2q_1 - 2q_2}{k_1 + k_2 + 2q_1 + 2q_2} \right) \\
r_{21} &= \left( \frac{2\sqrt{k_1 k_2}}{k_1 + k_2 + 2q_1 + 2q_2} \right) \\
f_{21} = g_{21} &= \left( \frac{2\sqrt{k_2 q_1}}{k_1 + k_2 + 2q_1 + 2q_2} \right) \\
f_{22} = g_{22} &= \left( \frac{2\sqrt{k_2 q_2}}{k_1 + k_2 + 2q_1 + 2q_2} \right)
\end{aligned}$$

$S$  matrix for the junction  $S_j$  is therefore

$$S_j = \begin{bmatrix} r_{11} & r_{12} & f_{11} & f_{12} & g_{11} & g_{12} \\ r_{21} & r_{22} & f_{21} & f_{22} & g_{21} & g_{22} \\ f_{11} & f_{12} & r_{11} & r_{12} & g_{11} & g_{12} \\ f_{21} & f_{22} & r_{21} & r_{22} & g_{21} & g_{22} \\ g_{11} & g_{12} & g_{11} & g_{12} & r_{11} & r_{12} \\ g_{21} & g_{22} & g_{21} & g_{22} & r_{21} & r_{22} \end{bmatrix} \quad (5.24)$$

One can check that the following conditions of unitarity are satisfied

$$|r_{11}|^2 + |r_{12}|^2 + |f_{11}|^2 + |f_{12}|^2 + |g_{11}|^2 + |g_{12}|^2 = 1 \quad (5.25)$$

$$|r_{22}|^2 + |r_{21}|^2 + |f_{21}|^2 + |f_{22}|^2 + |g_{21}|^2 + |g_{22}|^2 = 1 \quad (5.26)$$

Given an  $S$  matrix one can always solve the inverse scattering problem and find for what potential at the junction or for what angle of connecting the three legs of the junction one gets this  $S$  matrix. However, that would not be a relevant exercise.

The ring wave functions and the lead wave functions at the junction J1 of Fig. 5.1

can be matched as

$$\begin{pmatrix} \frac{r'_{11}}{\sqrt{k_1}} \\ \frac{r'_{12}}{\sqrt{k_2}} \\ \frac{A_1}{\sqrt{q_1}} \\ \frac{A_2}{\sqrt{q_2}} \\ \frac{D_1 e^{-iq_1 l_2}}{\sqrt{q_1}} \\ \frac{D_2 e^{-iq_2 l_2}}{\sqrt{q_2}} \end{pmatrix} = S_j \begin{pmatrix} \frac{1}{\sqrt{k_1}} \\ 0 \\ \frac{B_1 e^{-i\alpha}}{\sqrt{q_1}} \\ \frac{B_2 e^{-i\alpha}}{\sqrt{q_2}} \\ \frac{C_1 e^{iq_1 l_2 + i\beta}}{\sqrt{q_1}} \\ \frac{C_2 e^{iq_2 l_2 + i\beta}}{\sqrt{q_2}} \end{pmatrix} \quad (5.27)$$

and that at the junction J2 of the Fig. 5.1 can be matched as

$$\begin{pmatrix} \frac{B_1 e^{-iq_1 l_1}}{\sqrt{q_1}} \\ \frac{B_2 e^{-iq_2 l_1}}{\sqrt{q_2}} \\ \frac{C_1}{\sqrt{q_1}} \\ \frac{C_2}{\sqrt{q_2}} \\ \frac{t'_{11}}{\sqrt{k_1}} \\ \frac{t'_{12}}{\sqrt{k_2}} \end{pmatrix} = S_j \begin{pmatrix} \frac{A_1 e^{iq_1 l_1 + i\alpha}}{\sqrt{q_1}} \\ \frac{A_2 e^{iq_2 l_1 + i\alpha}}{\sqrt{q_2}} \\ \frac{D_1 e^{-i\beta}}{\sqrt{q_1}} \\ \frac{D_2 e^{-i\beta}}{\sqrt{q_2}} \\ 0 \\ 0 \end{pmatrix} \quad (5.28)$$

One can match the wavefunctions at the junction J2 to give a set of equations given below

$$1 + r'_{11} - \sqrt{\frac{k_1}{q_1}} A_1 - \sqrt{\frac{k_1}{q_1}} B_1 e^{-i\alpha} = 0 \quad (5.29)$$

$$r'_{12} - \sqrt{\frac{k_2}{q_2}} A_2 - \sqrt{\frac{k_2}{q_2}} B_2 e^{-i\alpha} = 0 \quad (5.30)$$

$$1 + r'_{11} - \sqrt{\frac{k_1}{k_2}} r'_{12} = 0 \quad (5.31)$$

$$1 + r'_{11} - \sqrt{\frac{k_1}{q_1}} C_1 e^{iq_1 l_2 + i\beta} - \sqrt{\frac{k_1}{q_1}} D_1 e^{-iq_1 l_2} = 0 \quad (5.32)$$

$$r'_{12} - \sqrt{\frac{k_2}{q_2}} C_2 e^{iq_2 l_2 + i\beta} - \sqrt{\frac{k_2}{q_2}} D_2 e^{-iq_2 l_2} = 0 \quad (5.33)$$

$$\begin{aligned} ik_1 - ik_1 r'_{11} - iq_1 \sqrt{\frac{k_1}{q_1}} A_1 + iq_1 \sqrt{\frac{k_1}{q_1}} B_1 e^{-i\alpha} - iq_2 \sqrt{\frac{k_1}{q_2}} A_2 + \\ iq_2 \sqrt{\frac{k_1}{q_2}} B_2 e^{-i\alpha} - iq_1 \sqrt{\frac{k_1}{q_1}} C_1 e^{iq_1 l_2 + i\beta} - iq_1 \sqrt{\frac{k_1}{q_1}} D_1 e^{-iq_1 l_2} + \\ iq_2 \sqrt{\frac{k_1}{q_2}} C_2 e^{iq_2 l_2 + i\beta} - iq_2 \sqrt{\frac{k_1}{q_2}} D_2 e^{-iq_2 l_2} - ik_2 \sqrt{\frac{k_1}{k_2}} r'_{12} = 0 \end{aligned} \quad (5.34)$$

$$t'_{11} - \sqrt{\frac{k_1}{q_1}} A_1 e^{iq_1 l_1 + i\alpha} - \sqrt{\frac{k_1}{q_1}} B_1 e^{-iq_1 l_1} = 0 \quad (5.35)$$

$$t'_{12} - \sqrt{\frac{k_2}{q_2}} A_2 e^{iq_2 l_1 + i\alpha} - \sqrt{\frac{k_2}{q_2}} B_2 e^{-iq_2 l_1} = 0 \quad (5.36)$$

$$t'_{11} - \sqrt{\frac{k_1}{k_2}} t'_{12} = 0 \quad (5.37)$$

$$t'_{11} - \sqrt{\frac{k_1}{q_1}} C_1 - \sqrt{\frac{k_1}{q_1}} D_1 e^{-i\beta} = 0 \quad (5.38)$$

$$t'_{12} - \sqrt{\frac{k_2}{q_2}} C_2 - \sqrt{\frac{k_2}{q_2}} D_2 e^{-i\beta} = 0 \quad (5.39)$$

$$\begin{aligned} & iq_1 \sqrt{\frac{k_1}{q_1}} A_1 e^{iq_1 l_1 + i\alpha} - iq_1 \sqrt{\frac{k_1}{q_1}} B_1 e^{-iq_1 l_1} + iq_2 \sqrt{\frac{k_1}{q_2}} A_2 e^{iq_2 l_1 + i\alpha} - \\ & iq_2 \sqrt{\frac{k_1}{q_2}} B_2 e^{-iq_2 l_1} - iq_1 \sqrt{\frac{k_1}{q_1}} C_1 + iq_1 \sqrt{\frac{k_1}{q_1}} D_1 e^{i\beta} - iq_2 \sqrt{\frac{k_1}{q_2}} C_2 + \\ & iq_2 \sqrt{\frac{k_1}{q_2}} D_2 e^{-i\beta} - ik_1 t'_{11} - ik_2 \sqrt{\frac{k_1}{k_2}} t'_{12} = 0 \end{aligned} \quad (5.40)$$

Solving them we can find the  $S$  matrix elements  $r'_{11}$ ,  $r'_{12}$ ,  $t'_{11}$  and  $t'_{12}$  for the Aharonov - Bohm ring. Similarly we can find  $r'_{22}$ ,  $r'_{21}$ ,  $t'_{22}$ , and  $t'_{21}$ .

### 5.3 Results and Discussions

Here we are considering two channel Aharonov-Bohm ring that are characterized by four transmission amplitudes  $t'_{11}$ ,  $t'_{12}$ ,  $t'_{21}$  and  $t'_{22}$  and four reflection amplitudes  $r'_{11}$ ,  $r'_{12}$ ,  $r'_{21}$  and  $r'_{22}$ . Landauer's formula gives the two probe conductance  $G$  as

$$G = \frac{2e^2}{h} \sum_{i,j} |t'_{ij}|^2. \quad (5.41)$$

The transmission amplitude from mode  $j$  to mode  $i$  is  $t'_{ij}$ .  $G$  is a strongly oscillating function of  $\phi/\phi_0$  implying we can use flux to drive the system from a conducting state to an insulating state that can be identified with 1 and 0 of a switch as will be exemplified. Such a switch will therefore be working entirely on quantum mechanical principles. Such devices if achieved will be a major technological breakthrough. First of all, it will transcend Moore's law [3, 4] by leaps and bounds to result in extremely small devices. Secondly, such devices will consume very little

power and will solve the problem of present day computers dissipating a lot of energy and getting heated up. Other advantages are mentioned in Section 5.1. However, such devices have not been achieved so far because switches based on quantum interference principles as the one we are discussing here in our work are not stable [89]. Small changes in temperature or incorporation of a single impurity can drastically change the operational characteristics of the switch. One can understand this in terms of the fact that impurity cause additional reflections or temperature increases Fermi energy and hence wavelength and therefore imply changes in path lengths in an interference set up. We demonstrate below how changes in path lengths can drastically alter the operational characteristics of an Aharonov-Bohm ring. Finally we will show that there is a solution to the problem.

Note, a periodic system can not have two minima and one maximum within one period. In the following when we refer to it we mean two different kinds of minima and only one kind of maximum. In Fig. 5.4, we show  $\frac{G}{2e^2/h}$  for a two

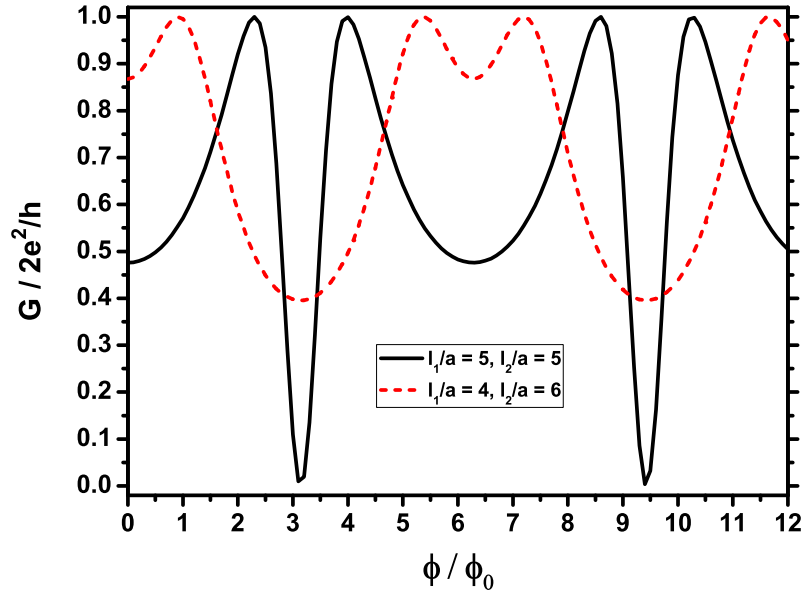


Figure 5.4: The figure shows a plot of  $\frac{G}{2e^2/h}$  as a function of  $\phi/\phi_0$ . Here  $\phi_0 = hc/e$ . The incoming electrons have energy  $E = \frac{55h^2}{m^*a^2}$  and the constant potential  $V_0$  of the ring is 0. We are considering in this case two propagating modes. The solid line is  $\sum_{i,j} |t'_{ij}|^2$  for  $l_1/a = 5$ ,  $l_2/a = 5$  and the dashed line is  $\sum_{i,j} |t'_{ij}|^2$  for  $l_1/a = 4$ ,  $l_2/a = 6$ .

channel Aharonov-Bohm ring with  $l_1/a = 5$ ,  $l_2/a = 5$  (solid line) and with  $l_1/a = 4$ ,  $l_2/a = 6$  (dashed line). We choose incident energy in the range given by Eq. (5.16) and so we are considering a two channel scattering problem. We take the potential inside the ring  $V_0$  to be 0 implying that both channels are propagating inside the

ring. Solid line shows two conductance minima, one is shallow at flux  $\phi/\phi_0 = 0$  (approx) and another is deep at flux  $\phi/\phi_0 = 3.1$  (approx) and it also shows one conductance maximum at flux  $\phi/\phi_0 = 2.4$  (approx). Dashed line also shows two conductance minima, one is shallow at flux  $\phi/\phi_0 = 0$  (approx) and another is deep at flux  $\phi/\phi_0 = 3.1$  (approx) and it shows one conductance maximum at flux  $\phi/\phi_0 = 1.0$  (approx). We can assign the conductance minimum as off state and conductance maximum as on state of a switch. Fig. 5.4 shows that with changing the arm length the minimum is not shifting but maximum is shifting a lot. The shallow minimum for dashed line is so shallow that it may not be observed in measurement. Much more non-systematic behavior will be shown in subsequent plots. Now we will plot the individual  $|t'_{ij}|^2$  s as a function of  $\phi/\phi_0$  and shown in Fig. 5.5. All the plots

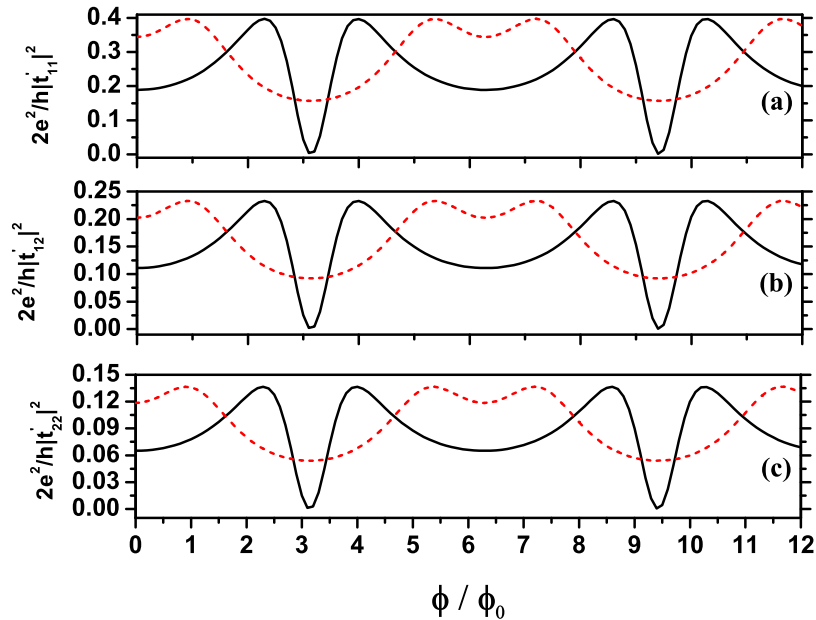


Figure 5.5: We use same parameters as in Fig. 5.4 and plot individual scattering cross sections. (a) shows a plot of  $|t'_{11}|^2$  as a function of  $\phi/\phi_0$ . (b) shows a plot of  $|t'_{12}|^2$  as a function of  $\phi/\phi_0$ .  $|t'_{21}|^2$  as a function of  $\phi/\phi_0$  is identical to  $|t'_{12}|^2$  as a function of  $\phi/\phi_0$  due to Onsager reciprocity relation, so  $|t'_{21}|^2$  is not shown. (c) shows a plot of  $|t'_{22}|^2$  as a function of  $\phi/\phi_0$ . Here  $\phi_0 = hc/e$ . The solid lines are for  $l_1/a = 5$ ,  $l_2/a = 5$  and the dashed lines are for  $l_1/a = 4$ ,  $l_2/a = 6$ .

of individual partial scattering cross sections ( $|t'_{11}|^2$ ,  $|t'_{12}|^2 = |t'_{21}|^2$  and  $|t'_{22}|^2$ ) are qualitatively same as the plot of  $\sum_{i,j} |t'_{ij}|^2$  as a function of  $\phi/\phi_0$ . Peaks are expected to occur at resonance [107] when integral wave numbers fit into the total length of the Aharonov-Bohm ring. However in presence of channel mixing the two channels are not independent. Resonance in one channel builds up density of states in the other channel and so  $|t'_{11}|^2$ ,  $|t'_{12}|^2$ ,  $|t'_{21}|^2$  and  $|t'_{22}|^2$  peak at same flux values. Conductance is

determined by the addition of these individual scattering cross sections. Since they are qualitatively same they add up coherently. When all these partial scattering cross sections are coherently added the difference between the on state and the off state becomes 100% for deep minimum and it is 50 % for shallow minimum in case of solid line in Fig. 5.4, while it is only 60% for deep minimum and 12% for shallow minimum in case of dashed line in Fig. 5.4. Such variations in magnitudes of drops in conductance apart from variations in peak positions already discussed indicates that it is not so efficient to make stable switches. In Fig. 5.6, we show  $\frac{G}{2e^2/h}$  for a two

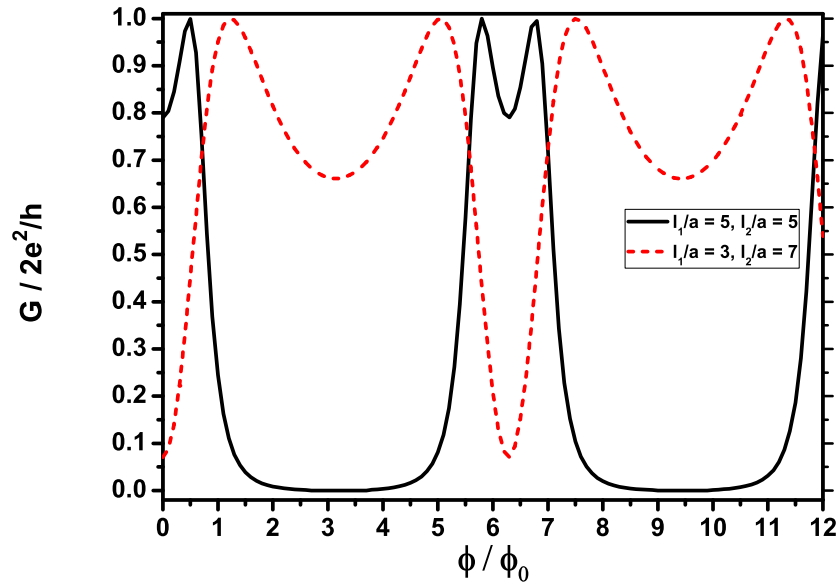


Figure 5.6: The figure shows a plot of  $\frac{G}{2e^2/h}$  as a function of  $\phi/\phi_0$ . Here  $\phi_0 = hc/e$ . The incoming electrons have energy  $E = \frac{45\hbar^2}{m^*a^2}$ , the constant potential  $V_0$  of the ring is such that  $V_0 = \frac{10\hbar^2}{em^*a^2}$ . With this choice  $q_1$  is real and  $q_2$  is imaginary. Thus, we are considering in this case one propagating mode and one evanescent mode. The solid (black) line is  $\frac{G}{2e^2/h}$  for  $l_1/a = 5$ ,  $l_2/a = 5$  and the dashed (red) line is  $\frac{G}{2e^2/h}$  for  $l_1/a = 3$ ,  $l_2/a = 7$ .

channel Aharonov-Bohm ring with  $l_1/a = 5$ ,  $l_2/a = 5$  (solid line) and with  $l_1/a = 3$ ,  $l_2/a = 7$  (dashed line). Again we choose energy in the range given by Eq. (5.16). However now we also take a non zero electrostatic potential  $V_0$  inside the ring such that  $q_1$  is real and  $q_2$  is imaginary (see Eq. (5.21) and Eq. (5.22)). In other words one channel is propagating and the other is evanescent. We have checked that such a situation result in just as much diversity as that with two propagating modes. Here we demonstrate one particular case and give arguments why the behavior is general. Solid line shows two conductance minima and one conductance maximum like the solid line in Fig. 5.4. It has first a shallow minimum and then has a deep

minimum similar to solid line in Fig. 5.4. Dashed line shows two conductance minima and one conductance maximum like the dashed line in Fig. 5.4. Here one that was shallow minimum in Fig. 5.4 has become a deep minimum and the one that was deep minimum in Fig. 5.4 has become shallow minimum. Unlike in Fig. 5.4, there is wave propagation in only one channel and since the other channel is evanescent, it has no wave propagation. Peaks occur for propagating channel when integral wave numbers fit into the total length of the ring [107]. But here we can see  $|t'_{22}|^2$  peak at same flux values as  $|t'_{11}|^2$  because again in presence of channel mixing the two modes are not independent. Resonance in the propagating channel boost up density of states in the evanescent channel and hence the evanescent channel also becomes highly conducting. Thus the diversity results from the random behavior of the propagating channel.

We show the individual  $|t'_{ij}|^2$ s corresponding to Fig. 5.6 in Fig. 5.7. They are again qualitatively same as the curves obtained in Fig. 5.6 which means the individual components add up coherently just as it happened for two propagating modes. Conduction along the evanescent mode is equally strong and diverse due to the presence of the propagating mode.

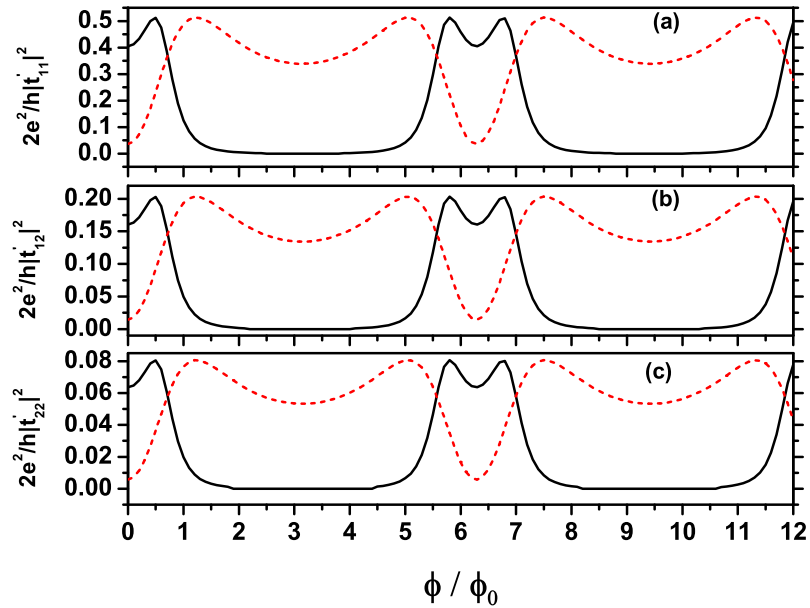


Figure 5.7: We use same parameters as in Fig. 5.5 and plot individual scattering cross sections. (a) shows a plot of  $|t'_{11}|^2$  as a function of  $\phi/\phi_0$ . (b) shows a plot of  $|t'_{12}|^2$  as a function of  $\phi/\phi_0$ .  $|t'_{21}|^2$  as a function of  $\phi/\phi_0$  is identical to  $|t'_{12}|^2$  as a function of  $\phi/\phi_0$  due to Onsager reciprocity relation, so  $|t'_{21}|^2$  is not shown. (c) shows a plot of  $|t'_{22}|^2$  as a function of  $\phi/\phi_0$ . Here  $\phi_0 = hc/e$ . The solid (black) lines are for  $l_1/a = 5$ ,  $l_2/a = 5$  and the dashed (red) lines are for  $l_1/a = 3$ ,  $l_2/a = 7$ .

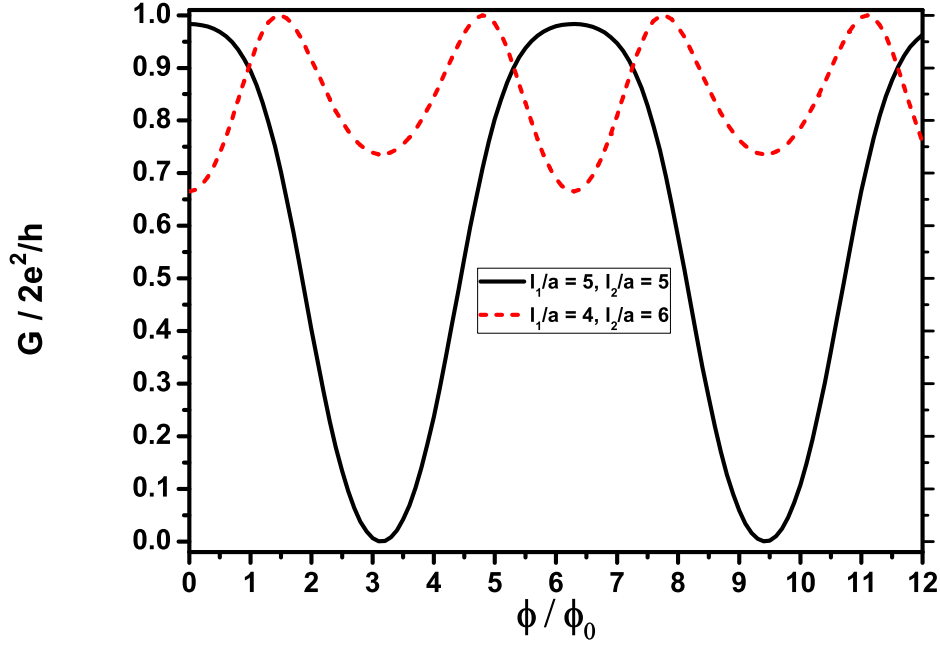


Figure 5.8: The figure shows a plot of  $\frac{G}{2e^2/h}$  as a function of  $\phi/\phi_0$ . Here  $\phi_0 = hc/e$ . The incoming electrons have energy  $E = \frac{47\hbar^2}{m^*a^2}$ , the constant potential  $V_0$  of the ring is such that  $V_0 = \frac{10\hbar^2}{em^*a^2}$ . With this choice  $q_1$  is real and  $q_2$  is imaginary. Thus, we are considering in this case one propagating mode and one evanescent mode. The solid line is  $\frac{G}{2e^2/h}$  for  $l_1/a = 5$ ,  $l_2/a = 5$  and the dashed (red) line is  $\frac{G}{2e^2/h}$  for  $l_1/a = 4$ ,  $l_2/a = 6$ .

In Fig. 5.8, we show  $\frac{G}{2e^2/h}$  for a two channel Aharonov-Bohm ring with  $l_1/a = 5$ ,  $l_2/a = 5$  (solid line) and with  $l_1/a = 4$ ,  $l_2/a = 6$  (dashed line). Incident energy and the electrostatic potential are so chosen that like in Fig. 5.6 one channel is propagating and another is evanescent. Solid line shows one conductance maximum and one conductance minimum instead of two conductance minima seen in earlier figures. Only difference is that we have slightly changed the energy of the incoming electrons from  $E = \frac{45\hbar^2}{m^*a^2}$  (Fig. 5.6) to  $E = \frac{47\hbar^2}{m^*a^2}$  (Fig. 5.8) keeping  $l_1, l_2$  same. Dashed line shows two conductance minima and one conductance maximum. The drops of two minima are comparable which gives the appearance of a  $\phi_0/2$  periodicity. This is unlike what we saw in earlier figures. Here too all the plots of individual partial scattering cross sections are qualitatively same as the plot of  $\sum_{i,j} |t'_{ij}|^2$  as a function of  $\phi/\phi_0$  and so not shown. The random behavior of conductance changes when we make both the modes to be evanescent. An electron in an evanescent mode do not acquire phase changes associated with propagation. Only phase changes are due to Aharonov-Bohm effect and we find that within a period (0 to  $2\pi$ ) conductance is

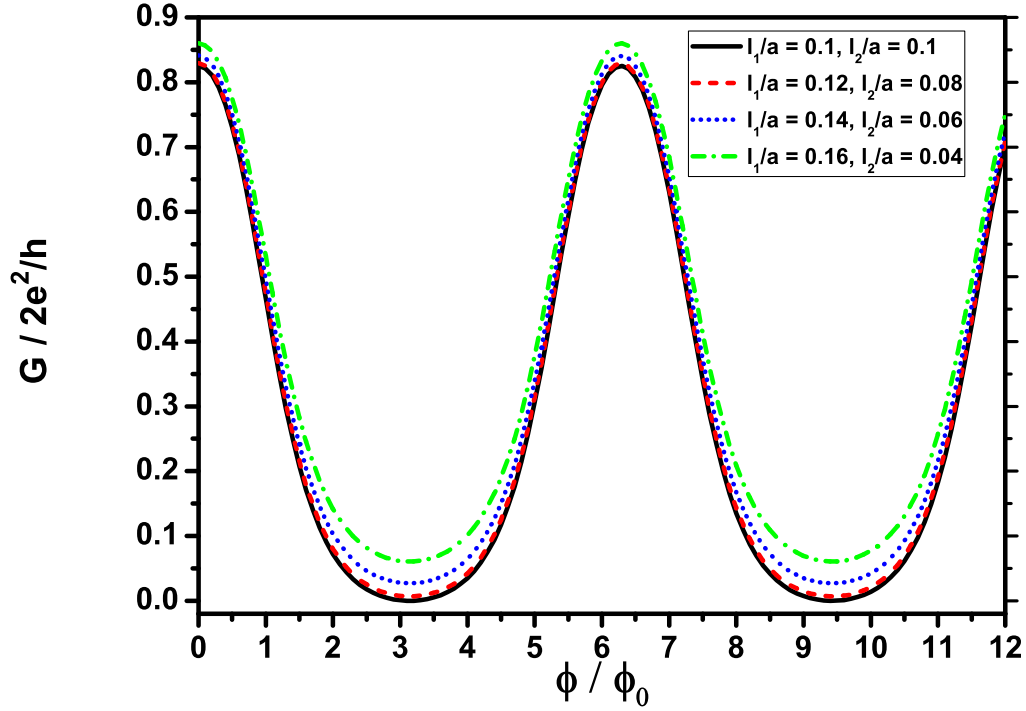


Figure 5.9: The figure shows a plot of  $\frac{G}{2e^2/h}$  as a function of  $\phi/\phi_0$  for different arm lengths. Here  $\phi_0 = hc/e$ . The incoming electrons have energy  $E = \frac{49\hbar^2}{m^*a^2}$ . The constant potential  $V_0$  of the ring is such that  $V_0 = \frac{40\hbar^2}{em^*a^2}$ . With this choice  $q_1$  and  $q_2$  are both imaginary. Thus, we are considering in this case two evanescent modes. The exact value of  $l_1$  and  $l_2$  are given in the figure inset. For all arm length  $\frac{G}{2e^2/h}$  as a function of  $\phi/\phi_0$  have the same nature. That means switching action is independent of  $l_1 : l_2$ .

maximum at zero flux, then it goes through a deep minimum and rise again to a maximum value. One can explain this as follows. Conductance being a symmetric function of flux (Onsager reciprocity relation), is a function of  $(\cos n\phi/\phi_0)$ . So it maximizes at 0 flux and then decreases with flux. Periodicity is always  $\phi_0$  in absence of other competing source of phase changes and absence of resonances. This behavior is independent of all parameters as will be demonstrated below. However since evanescent modes are not very conducting we have to take smaller rings to get same order of magnitude in conductance variations as that of propagating modes. But the magnitude can be enhanced by taking a ring that can support many evanescent modes as all modes add up coherently.

In Fig. 5.9, we have taken many choices of arm length and we have seen that there is only one conductance maximum at flux  $\phi/\phi_0 = 0$  (approx) and only one

conductance minimum at flux  $\phi/\phi_0 = 2.5$  (approx). Thus, here the behavior remains uniform with changing the arm length. Conductance variation from maximum to minimum is 82%. The individual  $|t'_{ij}|^2$  s as a function of  $\phi/\phi_0$  show similar behavior

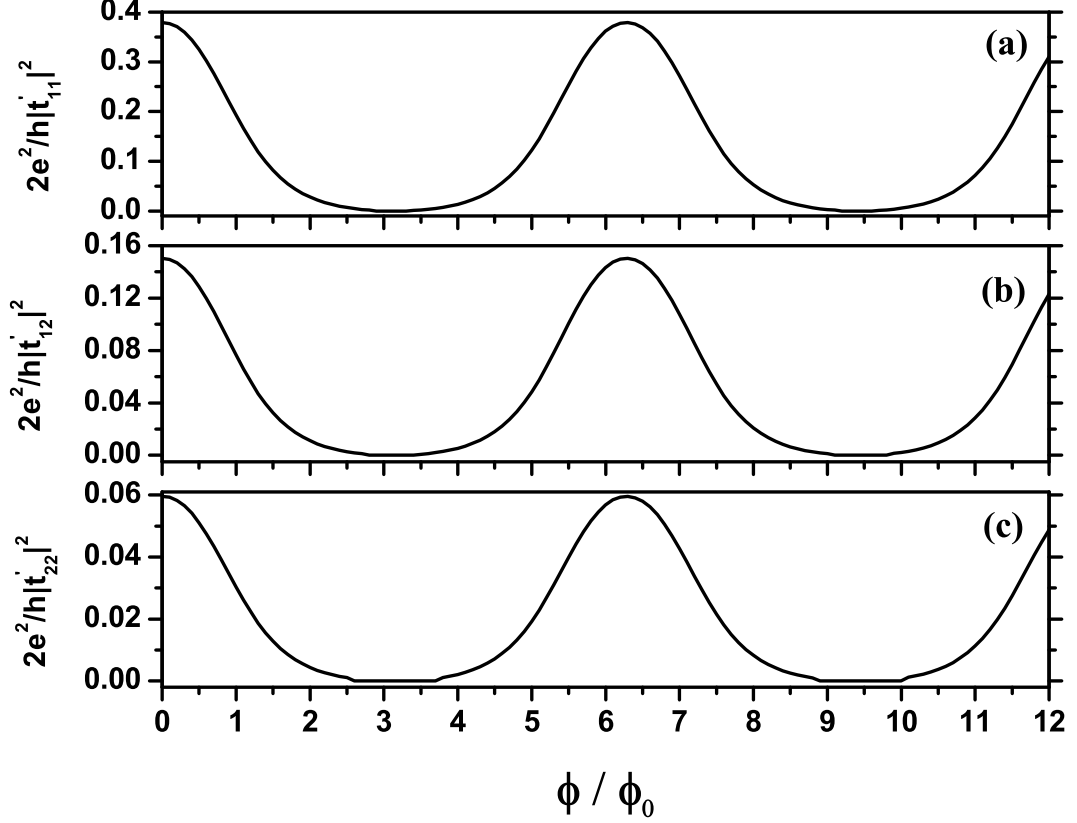


Figure 5.10: We use same parameters as in Fig. 5.9 and plot individual scattering cross sections. (a) shows a plot of  $|t'_{11}|^2$  as a function of  $\phi/\phi_0$ . (b) shows a plot of  $|t'_{12}|^2$  as a function of  $\phi/\phi_0$ .  $|t'_{21}|^2$  as a function of  $\phi/\phi_0$  is identical to  $|t'_{12}|^2$  as a function of  $\phi/\phi_0$  due to Onsager reciprocity relation, so  $|t'_{21}|^2$  is not shown. (c) shows a plot of  $|t'_{22}|^2$  as a function of  $\phi/\phi_0$ . Here  $\phi_0 = hc/e$ . The solid lines are for  $l_1/a = 0.1$ ,  $l_2/a = 0.1$ .

as that of Fig. 5.9 and shown in Fig. 5.10. In case of Fig. 5.10 (a), conductance drops by 38%, in case of Fig. 5.10 (b), conductance drops by 18% and for Fig. 5.10 (c), conductance drops by 8%. When different channels add up coherently percentage drop of conductance becomes 82%. By using larger and larger number of evanescent channels percentage drop in conductance can thus be enhanced and efficiency of switch can be increased.

It is not always possible to maintain the incidence energy ( $\frac{Em^*a^2}{\hbar^2}$ ) values constant due to statistical fluctuation in voltage of the battery or due to temperature changes. Now we will plot  $\sum_{i,j} |t'_{ij}|^2$  as a function of  $\phi/\phi_0$  for different  $\frac{Em^*a^2}{\hbar^2}$  values and we

will show that the behavior is also independent of incident energy when we employ evanescent modes. This is not the case with propagating modes where changes of incident energy result in just as much diversity that we get on changing  $l_1$  and  $l_2$  and hence not shown here. In Fig. 5.11, two values of incident energy and electrostatic

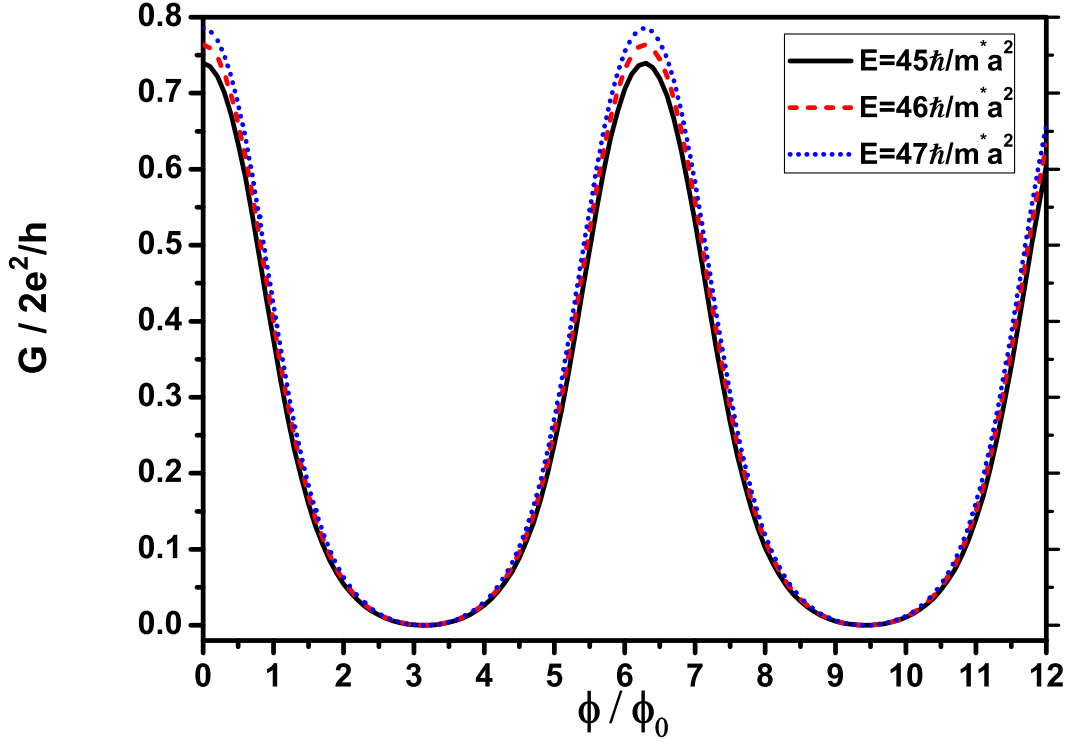


Figure 5.11: The figure shows a plot of  $\frac{G}{2e^2/h}$  as a function of  $\phi/\phi_0$  for different incoming energy. Here  $\phi_0 = hc/e$ . The constant potential  $V_0$  of the ring is such that  $V_0 = \frac{40\hbar^2}{em^*a^2}$ . With this choice  $q_1$  and  $q_2$  are both imaginary. Thus, we are considering in this case two evanescent modes. The solid (black) line is  $\frac{G}{2e^2/h}$  for  $E = \frac{45\hbar^2}{m^*a^2}$ . The dashed (red) line is  $\frac{G}{2e^2/h}$  for  $E = \frac{46\hbar^2}{m^*a^2}$ . The dotted (blue) line is  $\frac{G}{2e^2/h}$  for  $E = \frac{47\hbar^2}{m^*a^2}$ . For all energy values  $\sum_{i,j} |t'_{ij}|^2$  as a function of  $\phi/\phi_0$  have the same nature. That means switching action is independent of incident energy.

potential are so chosen that both channels are evanescent. Here again we find that  $\sum_{i,j} |t'_{ij}|^2$  as a function of  $\phi/\phi_0$  is roughly independent of incident energy and the drop is almost 75-80%. Since in the evanescent mode switching action is independent of all parameters, switch can become stable, efficient and robust.

So far we have considered two propagating, one propagating - one evanescent and two evanescent modes separately. For all these cases the total ring length were the same and we only changed the relative ratio of arm lengths. In these cases we

have shown that when there are propagating modes then the peaks are shifting and the depth of the valleys are changing from shallow to deep. We have also shown that in presence of channel mixing the conductance peaks are not determined by resonance alone as thought before. However peaks are determined by the total ring length. If we consider cases where the total ring length does not remain same then one can get even more diverse behavior. Impurity scattering and temperature changes can affect the total length as well. In Fig. 5.12 we have considered both the

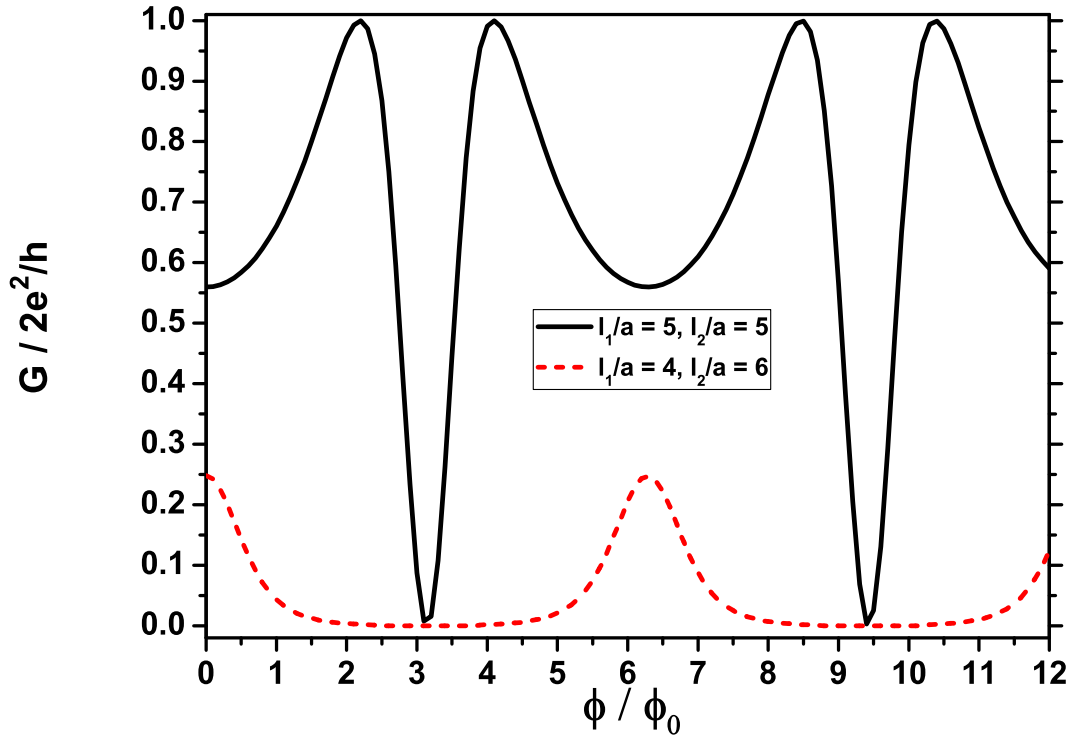


Figure 5.12: The figure shows a plot of  $\frac{G}{2e^2/h}$  as a function of  $\phi/\phi_0$  for two choice of total ring lengths. Here  $\phi_0 = hc/e$ . The incoming electrons have energy  $E = \frac{45\hbar^2}{m^*a^2}$ , the constant potential  $V_0$  of the ring is 0. With this choice  $q_1$  and  $q_2$  are both real. Thus, we are considering in this case two propagating modes. The solid line is  $\frac{G}{2e^2/h}$  for  $L/a = 10$  ( $l_1/a = 5, l_2/a = 5$ ) and the dashed line is  $\frac{G}{2e^2/h}$  for  $L/a = 8$  ( $l_1/a = 4, l_2/a = 4$ ).

channels to be propagating with two choices of  $(l_1 + l_2)$ . We have shown here that resonance position of the solid line is different from the resonance position of the dashed line. The solid line has a valley where the dashed line has a peak. But again if we use evanescent modes then changes in total ring length can not result in diverse behavior. So in Fig. 5.13 we have considered both the channels to be evanescent

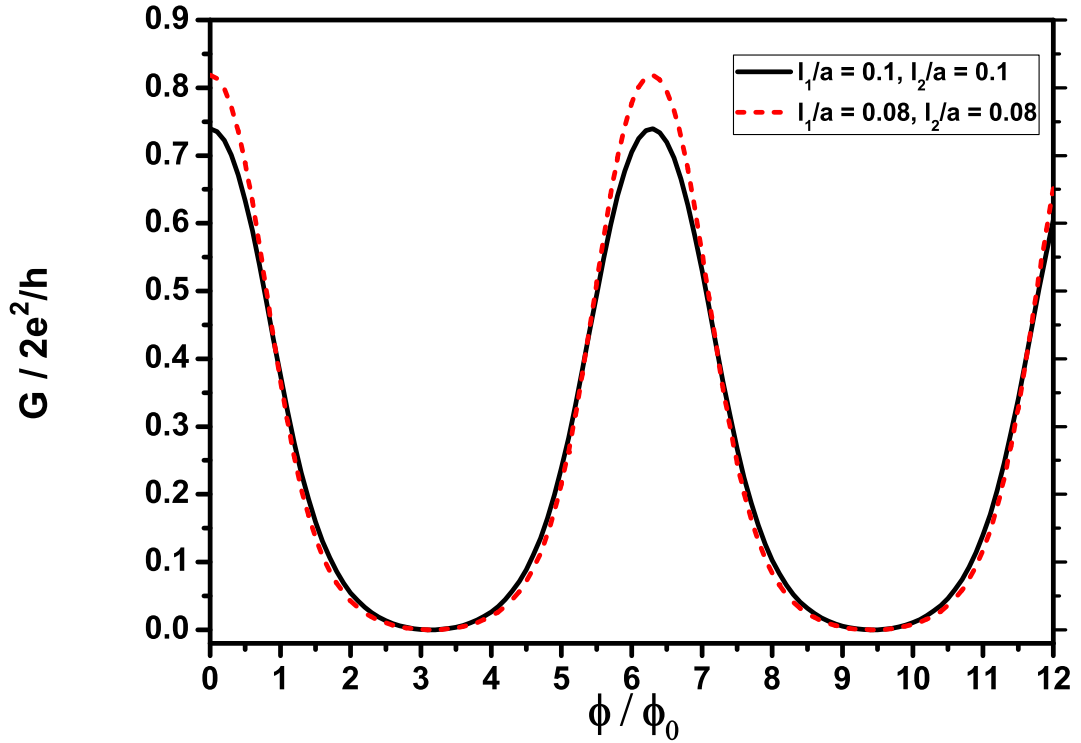


Figure 5.13: The figure shows a plot of  $\frac{G}{2e^2/h}$  as a function of  $\phi/\phi_0$ . Here  $\phi_0 = hc/e$ . The incoming electrons have energy  $E = \frac{45\hbar^2}{m^*a^2}$ , the constant potential  $V_0$  of the ring is such that  $V_0 = \frac{40\hbar^2}{em^*a^2}$ . With this choice  $q_1$  and  $q_2$  are both imaginary. Thus, we are considering in this case two evanescent modes. The solid line is  $\frac{G}{2e^2/h}$  for  $L/a = 0.2$  ( $l_1/a = 0.1$ ,  $l_2/a = 0.1$ ) and the dashed line is  $\frac{G}{2e^2/h}$  for  $L/a = 0.16$  ( $l_1/a = 0.08$ ,  $l_2/a = 0.08$ ).

with two choices of  $(l_1 + l_2)$ . Here the nature of the solid curve and the dotted curve are the same as that obtained so far. We have shown in previous figures that if we use evanescent modes, conductance does not depend on the relative ratios of arm lengths and Fermi energy and in this Fig. 5.13 we have shown that the conductance also does not depend on the total ring length of the Aharonov-Bohm ring.

## 5.4 Conclusion

In this work we have studied two channel (transverse modes) Aharonov-Bohm ring. When we consider both the channels to be propagating then we have shown that if we change the parameters such as the total ring length, relative ratio of arm lengths, Fermi energy etc., the behavior of the conductance becomes diverse in nature in dif-

ferent cases. Similar situation arises if we take one propagating and one evanescent modes. In presence of channel mixing the modes are not independent. Resonance in the propagating channel boost up density of states in the evanescent channel and hence the evanescent channel also becomes highly conducting. Such diverse behavior supports Landauer's claim that switch action based on interference principle are not stable and practical. Finally we have considered both the modes to be evanescent along the Aharonov-Bohm ring. Here we have found that conductance is qualitatively as well as quantitatively same for all variations in parameters like total ring length, relative ratio of arm lengths, Fermi energy etc. We can obtain appreciable changes in conductance when using evanescent modes. Different channels add up coherently and so by using larger and larger number of evanescent channels we can enhance the percentage drop in conductance and hence efficiency of the switch. Change in impurity configuration effectively changes the total ring length and the relative ratio of arm lengths. Rise or drop in temperature effectively changes Fermi energy and hence wavelength. Therefore, conductance behavior will be same if we change the impurity configuration or temperature when we use evanescent modes. Propagation is associated with phase changes which do not arise in case of evanescent modes. In evanescent modes, phase changes are due to Aharonov - Bohm effect only. Periodicity is always  $\phi_0$  in absence of other competing source of phase changes. Conductance being a symmetric function of flux is a function of  $\cos(n\phi/\phi_0)$ . Therefore within a period (0 to  $2\pi$ ) conductance is maximum at zero flux, then it goes through a deep minimum and rise again to a maximum value. We can assign the conductance maximum as on state and conductance minimum as off state of a switch signifying 1 and 0 operation in Boolean algebra. Thus we can conclude that if we employ evanescent modes only, we may be able to build stable, efficient and robust quantum switches. In an experimental situation one does not apply an Aharonov-Bohm flux but a uniform magnetic field [35] to obtain Aharonov-Bohm oscillation. Lorentz force being weighted down by the velocity of light, uniform magnetic field results in Aharonov-Bohm effect alone [35]. So in a device where one has to employ many switches and can also require that one switch is on while an adjacent switch is off can be achieved by intelligently designing the lengths of the rings so that their areas are different and they capture different amounts of flux.

Earlier works have proposed the possibility of switch action with other geometric configurations apart from Aharonov - Bohm ring such as T - shaped structure [86] etc. We may also expect that if we employ evanescent modes in other geometries, conductance will be independent of sample parameters. This is because propagation along evanescent channels are not associated with phase changes. Phase changes can only be induced by external stimuli which is electrostatic potential in case of Ref. [86, 87].

## Chapter 6

# CURRENT CARRIED BY EVANESCENT MODES AND POSSIBLE DEVICE APPLICATIONS

*“Any intelligent fool can make things  
bigger and more complex.....,  
it takes a touch of genius..... and a lot of courage.....  
to move in the opposite direction.”*

–Albert Einstein.

Quantum tunneling of an electron through a classically forbidden regime has no classical analogue and several aspects of it is still not understood. In this chapter we analyze a situation where electronic current under the barrier can be measured without disturbing the states under the barrier. In Section 6.2, we consider a multichannel Aharonov-Bohm ring and develop the correct formalism to calculate the currents inside the ring when the states are evanescent. In Section 6.3, we have discussed various transport phenomena like conductance current, circulating current, persistent current etc as well as non-transport phenomenon like magnetization using propagating as well as evanescent states. We also show unlike other proposed quantum devices that such currents are not very sensitive to changes in material parameters and environment. Finally this chapter is concluded in Section 6.4 with the summary of the results and we have shown that there is possibility of robust device action based on magnetic response using only evanescent mode.

## 6.1 Introduction

In the last three decades, there has been a major interest in the properties of mesoscopic systems [108]. Most of the experimental and theoretical studies of these systems have involved transport measurements, usually of the resistance as a function of temperature or magnetic field. However, there is increasing interest in other non-transport properties, such as magnetization. This has prompted a lot of experimental works, including the study of arrays of mesoscopic systems, and the use of very small Hall sensors and microsquid magnetometers. These studies give us an unique opportunity to understand and explore manifestations of quantum mechanics like persistent current, circulating current etc.

Besides recent advances in mesoscopic structures have led to the possibility of new quantum semiconductor devices. These active quantum devices rely on quantum effects for their operation based on interferometric principles, and are quantum analog of well-known optical and microwave devices [6]. Several potential magnetic devices have been proposed [109, 110], viz., Hall devices, magnetoresistors, inductive proximity and distance sensors, fluxgate sensors, other magnetic sensors such as magnetodiodes, magFETs, magnetotransistors and carrier domain magnetometers. Some commonly seen devices that work in classical regime and use magnetic properties are magnetic tape used for data storage, magnetic card reader, keycard lock etc. The conventional devices operate in a classical diffusive regime and are not very sensitive to variations in material parameters such as dimensions or the presence of small impurities or non-uniformity in size and shape. These devices operate by controlling the carrier density of quasi-particles. So far no quantum devices in mesoscopic or nanoscopic length have been achieved practically because quantum devices have an inherent shortcoming. Proposed quantum devices are not very robust in the sense that the operational characteristics depend very sensitively on material parameters, impurity configuration, shape and size of sample, temperature and Fermi energy [89]. For example, incorporation of a single impurity in the mesoscopic device can change, non-trivially, the interference of partial electron waves propagating through the sample, and hence the electron transmission (operational characteristics) across the sample [90]. In such devices the actual problem of control and reproducibility of operating thresholds become highly nontrivial. These devices can be exploited if we achieve the technology that can reduce or control the phase fluctuations [91] to a small fraction of  $2\pi$ . Devices in which electrons carry current without being scattered either elastically or inelastically (ballistic devices) promise to be much faster and will consume less power than the conventional devices. It should also be noted that quantum devices can exhibit multifunctional property (e.g., single stage frequency multiplier) wherein the functions of an entire circuit within a single element can be performed [88]. They can also lead to

tremendous down sizing of electronic devices. The magnetization of the ring has a spatial variation. This spatial variation can be used to store information just like a spatial array of capacitors store information in present day computers or spatially varying magnetic field in magnetic tapes. There can be an array of many quantum rings of different sizes. These can cause a magnetization which has complex spatial variation. A lot of work has been done in one dimensional quantum rings [91, 92, 93, 94, 98, 99, 100, 107]. However, the experimental rings are always in two dimension or in three dimension. Such systems have not received much theoretical attention because multichannel junctions are very difficult to treat theoretically. Also open rings where particle exchange can occur and temperature can be defined (a mesoscopic grand canonical system) is more general as closed ring properties can be seen as a special case [111]. This will be more realistic to study. Besides, such an open ring can exhibit some novel properties like current magnification or an evanescent mode that have no analogies in closed systems. Earlier models either do not account for channel mixing or do not allow the inclusion of evanescent modes. In our present work we account for both of these allowing us to study evanescent states in realistic two-dimensional and three-dimensional systems. Evanescent states have no classical analogs or classical interpretation in terms of wave packets. So current carried by an evanescent mode, time of flight in evanescent mode, velocity of evanescent mode etc are not well established. We show that magnetization due to such evanescent states has very interesting manifestation of quantum effects. We also argue that such effects can be used to build stable devices that uses quantum interference effects. We also study current magnification effect.

## 6.2 Theoretical Analysis

Fig. 6.1 represents the schematic diagram of a finite thickness mesoscopic quantum ring under consideration. Electronic transport in such systems can be well described by an effective mass theory [6]. Incident electrons coming from the source reservoir on the left (say), gets scattered by the ring. Division of wave front occurs at junction J1; a partial wave propagates along the upper arm of the ring and another partial wave propagates along the lower arm of the ring. These two partial waves recombine and give a transmittance that bears the signature of interference between the two partial waves along the two arms of the ring. This interference can be modified by an Aharonov-Bohm (A-B) flux through the center of the ring. The description of the figure is given in further detail in the figure caption.

The Schrödinger equation for a quasi one dimensional wire is (the third degree

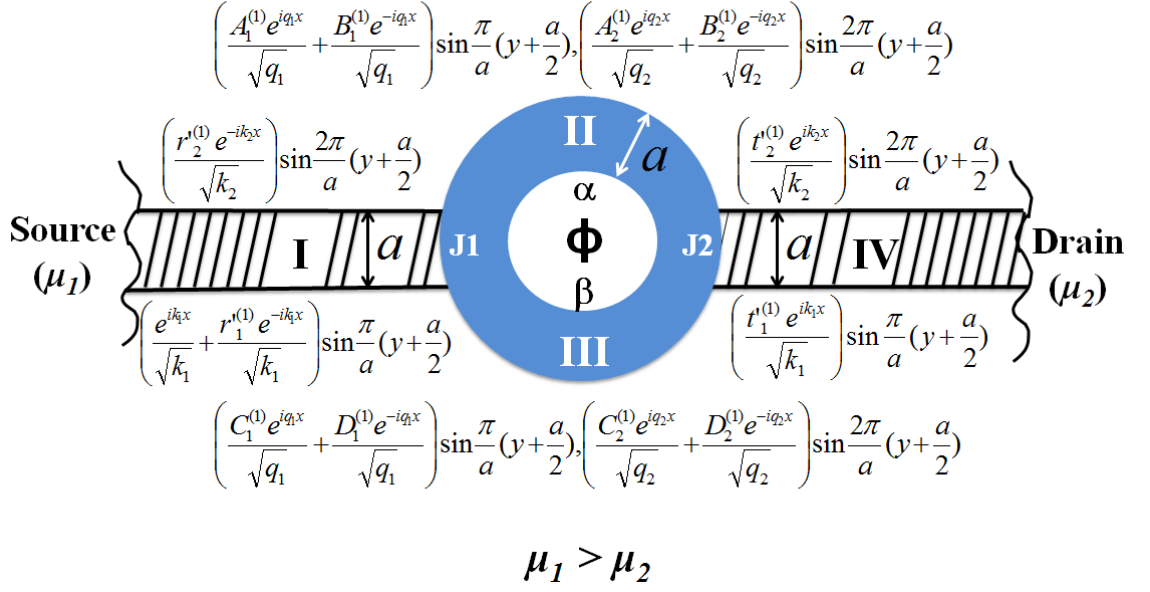


Figure 6.1: A finite thickness quantum ring of width  $a$  made up of normal metal or semiconductor is indicated by the blue colored region. On either sides the quantum ring is attached with quantum wires (stripped region) made up of normal metal or semiconductor. On the left of the above system there is the source reservoir whose chemical potential is  $\mu_1$  and on the right there is the drain reservoir whose chemical potential is  $\mu_2$ . A potential difference ( $\mu_1 - \mu_2$ ) between the source reservoir and the drain reservoir drives a transport current. The wave functions of the electron in different regions is shown in the figure at their respective places. Different regions are marked as I, II, III and IV. The ring is pierced by an Aharonov-Bohm (A-B) flux  $\phi$ .  $\alpha$  is the A-B phase an electron picks up in region II and  $\beta$  is that in region III. J1 is the junction where the regions I, II and III meets and J2 is the junction where the regions II, III and IV meets.

of freedom, i.e., z-direction, is usually frozen by creating a strong quantization [6])

$$-\frac{\hbar^2}{2m^*} \left( \frac{\partial^2 \psi}{\partial x^2} + \frac{\partial^2 \psi}{\partial y^2} \right) + V(x, y) \psi(x, y) = E \psi(x, y) \quad (6.1)$$

Here the  $x$  coordinate is along the wire,  $y$  coordinate is perpendicular to it,  $m^*$  is the electron effective mass and  $E$  is the electron energy. In regions I and IV (see Fig. 6.1) we have only the confinement potential. That is

$$V(x, y) = V(y).$$

Whereas in regions II and III apart from the confinement potential we take a constant

potential  $V_0$  that can be used to excite evanescent modes inside the ring. That is

$$V(x, y) = V(y) + V_0.$$

Without any loss of generality we take  $V(y)$  to be an infinite square well potential of width  $a$ . That is

$$V(y) = \begin{cases} 0 & \text{if } -a/2 < y < a/2; \\ \infty & \text{if } |y| \geq a/2. \end{cases}$$

The wave functions in the ring can be obtained by solving Eq. (6.1) where we assume the ring to be so large compared to the de Broglie wave length that its curvature can be neglected [101]. The length of the ring is  $L = l_U + l_L$ , where  $l_U$  is the length of the upper arm and  $l_L$  is the length of the lower arm. The magnetic field appears just as a phase of  $\psi(x, y)$  and will be accounted for while applying the boundary conditions [54]. In regions I and IV Eq. (6.1) can be separated as

$$\psi(x, y) = \phi(x)\xi(y) \quad (6.2)$$

to give

$$-\frac{\hbar^2}{2m^*} \frac{\partial^2 \phi(x)}{\partial x^2} = \frac{\hbar^2 k^2}{2m^*} \phi(x) \quad (6.3)$$

and

$$-\frac{\hbar^2}{2m^*} \frac{\partial^2 \xi(y)}{\partial y^2} + V(y)\xi(y) = \varepsilon \xi(y) \quad (6.4)$$

Since  $V(y)$  is an infinite square well potential of width  $a$ , Eq. (6.4) gives

$$\xi_n(y) = \sin \frac{n\pi}{a} \left( \frac{a}{2} + y \right) \quad (6.5)$$

and

$$\varepsilon_n = \frac{n^2 \pi^2 \hbar^2}{2m^* a^2} \quad (6.6)$$

Eq. (6.3) has solution of the form

$$\phi_n(x) = e^{\pm i k_n x}$$

with

$$k_n = \sqrt{\frac{2m^* E}{\hbar^2} - \frac{n^2 \pi^2}{a^2}} \quad (6.7)$$

or

$$E = \varepsilon_n + \frac{\hbar^2 k_n^2}{2m^*} \quad (6.8)$$

So wave function in region I assuming electron incidence occurs along channel 1 and

electrons are also reflected to channel 1, can be written as

$$\psi(I)_1^{(1)} = \left( \frac{e^{ik_1x}}{\sqrt{k_1}} + \frac{r_1^{(1)} e^{-ik_1x}}{\sqrt{k_1}} \right) \sin \frac{\pi}{a} \left( y + \frac{a}{2} \right) \quad (6.9)$$

Wave function in region I assuming electron incidence occurs along channel 1 and electrons are reflected to channel 2, can be written as

$$\psi(I)_2^{(1)} = \left( \frac{r_2^{(1)} e^{-ik_2x}}{\sqrt{k_2}} \right) \sin \frac{2\pi}{a} \left( y + \frac{a}{2} \right) \quad (6.10)$$

Wave function in region IV assuming electron incidence occurs along channel 1 and electrons are transmitted to channel 1 can be written as

$$\psi(IV)_1^{(1)} = \left( \frac{t_1^{(1)} e^{ik_1x}}{\sqrt{k_1}} \right) \sin \frac{\pi}{a} \left( y + \frac{a}{2} \right) \quad (6.11)$$

Wave function in region IV assuming electron incidence occurs along channel 1 and electrons are transmitted to channel 2 can be written as

$$\psi(IV)_2^{(1)} = \left( \frac{t_2^{(1)} e^{ik_2x}}{\sqrt{k_2}} \right) \sin \frac{2\pi}{a} \left( y + \frac{a}{2} \right) \quad (6.12)$$

From Eq. (6.7), in the first mode

$$k_1 = \sqrt{\frac{2m^*E}{\hbar^2} - \frac{\pi^2}{a^2}} \quad (6.13)$$

is the propagating wave vector and in the second mode

$$k_2 = \sqrt{\frac{2m^*E}{\hbar^2} - \frac{4\pi^2}{a^2}} \quad (6.14)$$

is the propagating wave vector. For

$$\frac{4\pi^2}{a^2} < E < \frac{9\pi^2}{a^2} \quad (6.15)$$

both  $k_1$  and  $k_2$  are real as can be seen from Eq. (6.13) and Eq. (6.14). In this energy range  $k_n$  for  $n > 2$  are imaginary as can be seen from Eq. (6.7) implying that there are two propagating channels. In the leads we can not have evanescent modes [24, 27].

Now for the regions II and III the potential is  $V(x, y) = V(y) + V_0$ . In these regimes using  $q_n$  as wave vector, the energy can be written similarly like region I

and IV as follows

$$E - V_0 = \frac{\hbar^2 q_n^2}{2m^*} + \frac{n^2 \pi^2 \hbar^2}{2m^* a^2} \quad (6.16)$$

or

$$q_n = \sqrt{\frac{2m^*(E - V_0)}{\hbar^2} - \frac{n^2 \pi^2}{a^2}}$$

Hence, in the first mode

$$q_1 = \sqrt{\frac{2m^*(E - V_0)}{\hbar^2} - \frac{\pi^2}{a^2}} \quad (6.17)$$

is the wave vector and in the second mode

$$q_2 = \sqrt{\frac{2m^*(E - V_0)}{\hbar^2} - \frac{4\pi^2}{a^2}} \quad (6.18)$$

is the wave vector. In regions II and III, three different situations can arise depending on the choice of energy,  $E$ , potential  $V_0$  and  $n$ . Wave functions in these regimes for  $E > V_0 + \frac{n^2 \pi^2 \hbar^2}{2m^* a^2}$  can be written similarly as in Eqs. (6.9) - (6.12).

$$\psi(II)_1^{(1)} = \left( \frac{A_1^{(1)} e^{iq_1 x}}{\sqrt{q_1}} + \frac{B_1^{(1)} e^{-iq_1 x}}{\sqrt{q_1}} \right) \sin \frac{\pi}{a} \left( y + \frac{a}{2} \right) \quad (6.19)$$

$$\psi(II)_2^{(1)} = \left( \frac{A_2^{(1)} e^{iq_2 x}}{\sqrt{q_2}} + \frac{B_2^{(1)} e^{-iq_2 x}}{\sqrt{q_2}} \right) \sin \frac{2\pi}{a} \left( y + \frac{a}{2} \right) \quad (6.20)$$

$$\psi(III)_1^{(1)} = \left( \frac{C_1^{(1)} e^{iq_1 x}}{\sqrt{q_1}} + \frac{D_1^{(1)} e^{-iq_1 x}}{\sqrt{q_1}} \right) \sin \frac{\pi}{a} \left( y + \frac{a}{2} \right) \quad (6.21)$$

$$\psi(III)_2^{(1)} = \left( \frac{C_2^{(1)} e^{iq_2 x}}{\sqrt{q_2}} + \frac{D_2^{(1)} e^{-iq_2 x}}{\sqrt{q_2}} \right) \sin \frac{2\pi}{a} \left( y + \frac{a}{2} \right) \quad (6.22)$$

$A_1^{(1)}$ ,  $B_1^{(1)}$ ,  $A_2^{(1)}$ ,  $B_2^{(1)}$  are the amplitudes of wave functions in upper arm and  $C_1^{(1)}$ ,  $D_1^{(1)}$ ,  $C_2^{(1)}$ ,  $D_2^{(1)}$  are the amplitudes of wave functions in lower arm for incidence of current along channel 1. Similarly,  $A_1^{(2)}$ ,  $B_1^{(2)}$ ,  $A_2^{(2)}$ ,  $B_2^{(2)}$  are the amplitudes of wave functions in upper arm and  $C_1^{(2)}$ ,  $D_1^{(2)}$ ,  $C_2^{(2)}$ ,  $D_2^{(2)}$  are the amplitudes of wave functions in lower arm for incidence of current along channel 2. Depending on the choice of energy  $E$  and potential  $V_0$ ,  $q_1$  and  $q_2$  can be real (propagating mode) as well as imaginary (evanescent mode). Such evanescent states can always be excited in the internal regions of the system but not in leads [24, 27]. In the regimes II and III, we can choose  $V_0$  to be non-zero such that for  $n = 1, 2$ ,  $E < V_0 + \frac{n^2 \pi^2 \hbar^2}{2m^* a^2}$ . Then we are considering both channels (modes) as evanescent channels.  $q_n$  is replaced by

$is_n$  and wave functions can be similarly written as

$$\psi(II)_1^{(1)} = \left( \frac{A_1^{(1)} e^{-s_1 x}}{\sqrt{is_1}} + \frac{B_1^{(1)} e^{s_1 x}}{\sqrt{is_1}} \right) \sin \frac{\pi}{a} \left( y + \frac{a}{2} \right) \quad (6.23)$$

$$\psi(II)_2^{(1)} = \left( \frac{A_2^{(1)} e^{-s_2 x}}{\sqrt{is_2}} + \frac{B_2^{(1)} e^{s_2 x}}{\sqrt{is_2}} \right) \sin \frac{2\pi}{a} \left( y + \frac{a}{2} \right) \quad (6.24)$$

$$\psi(III)_1^{(1)} = \left( \frac{C_1^{(1)} e^{-s_1 x}}{\sqrt{is_1}} + \frac{D_1^{(1)} e^{s_1 x}}{\sqrt{is_1}} \right) \sin \frac{\pi}{a} \left( y + \frac{a}{2} \right) \quad (6.25)$$

$$\psi(III)_2^{(1)} = \left( \frac{C_2^{(1)} e^{-s_2 x}}{\sqrt{is_2}} + \frac{D_2^{(1)} e^{s_2 x}}{\sqrt{is_2}} \right) \sin \frac{2\pi}{a} \left( y + \frac{a}{2} \right) \quad (6.26)$$

Note that this form of the wave functions along with its imaginary normalization constant is necessary to give the correct expression for current in evanescent modes. We can also choose the constant potential  $V_0$  and the integer value of  $\frac{n^2 \pi^2 \hbar^2}{2m^* a^2}$  in such a fashion that one channel (or mode) is propagating and the other channel (or mode) is evanescent and we can describe the wavefunctions appropriately.

In Fig. 6.1 the potential  $V_0$  in the shaded region need not be made by an electrostatic field. One can do it by designing the system as shown in Fig. 6.2. Fig. 6.2 represents the schematic diagram of a mesoscopic interferometer (made up of normal metal or semiconductor). The width of the quantum wire  $a$ , is greater than the width of quantum ring  $w$ . For the regions II and III in Fig. 6.2, one can obtain just like in Eq. (6.17) and (6.18),

$$q'_1 = \sqrt{\frac{2m^* E}{\hbar^2} - \frac{\pi^2}{w^2}} = \sqrt{\frac{2m^* E}{\hbar^2} - \frac{\pi^2}{a^2} + \frac{\pi^2}{a^2} - \frac{\pi^2}{w^2}} = \sqrt{\frac{2m^*(E - V'_0)}{\hbar^2} - \frac{\pi^2}{a^2}} \quad (6.27)$$

where  $\frac{\pi^2}{a^2} - \frac{\pi^2}{w^2} = -\frac{2m^* V'_0}{\hbar^2}$ . Similarly, in the second mode

$$q'_2 = \sqrt{\frac{2m^*(E - V''_0)}{\hbar^2} - \frac{4\pi^2}{a^2}} \quad (6.28)$$

where  $\frac{4\pi^2}{a^2} - \frac{4\pi^2}{w^2} = -\frac{2m^* V''_0}{\hbar^2}$ . Therefore,  $V'_0$  and  $V''_0$  play the same role as  $V_0$  in Eq. (6.17) and (6.18). However, it simply originates from geometric parameters and not from an electrostatic potential. The dispersion relations for different regions (I, II and III, IV) are also shown in Fig. 6.2. (i) In regions I and IV, from Eq. (6.8) we see that E is given by  $E(k_n) = \frac{\hbar^2 k_n^2}{2m^*} + \frac{n^2 \pi^2 \hbar^2}{2m^* a^2}$ , where  $n = 1, 2, 3, \dots$ , denotes the modes. These dispersion relations for different modes indexed by  $n$  are indicated by solid lines (see Fig. 6.2). The offset values are obtained at  $\frac{\pi^2}{a^2}$  (for  $n = 1$ ),  $\frac{4\pi^2}{a^2}$  (for  $n = 2$ ) etc and are indicated by dotted lines. (ii) In regions II and III, from Eq. (6.27) and Eq. (6.28) E is given by  $E(q'_n) - V'_0$  (or  $V''_0$ ) =  $\frac{\hbar^2 q_n'^2}{2m^*} + \frac{n^2 \pi^2 \hbar^2}{2m^* a^2}$ , where  $n = 1, 2, 3, \dots$ ,

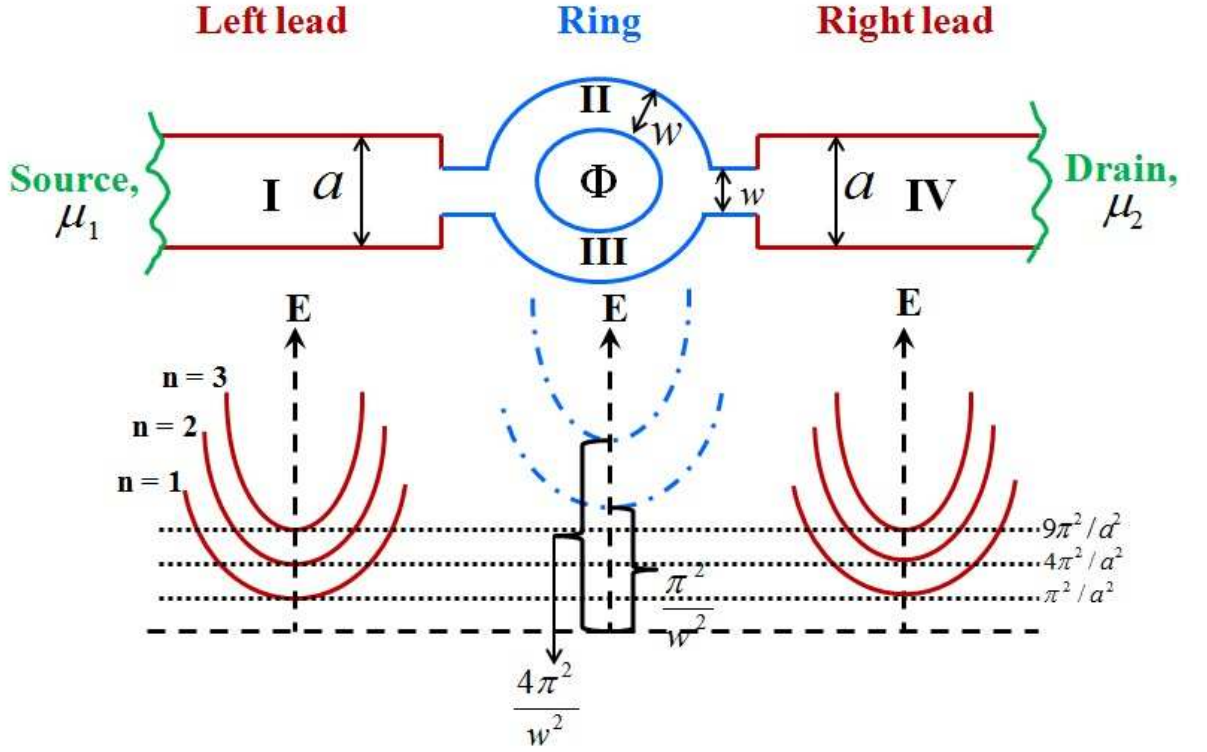


Figure 6.2: Top: Another schematic diagram of mesoscopic interferometer coupled to the left and right electron reservoirs. Electrostatic potential is zero everywhere. Bottom: Energy level dispersion curve for each region. Dispersion relation,  $E(k_n)$  vs.  $k_n$  obtained from Eq. (6.8) for propagating modes in regions I and IV, indicated by solid lines. Dispersion relation,  $E(q_n)$  vs.  $q_n$  obtained from Eq. (6.27) and Eq. (6.28) for evanescent modes in regions II and III, indicated by dash-dotted lines.

denotes the modes. The dispersion relations,  $E(q'_n)$  vs.  $q'_n$  obtained from Eq. (6.27) for different modes indexed by  $n$  are indicated by dash-dotted lines (see Fig. 6.2). Here the offset values are obtained at  $\frac{\pi^2}{w^2}$  (for  $n = 1$ ),  $\frac{4\pi^2}{w^2}$  (for  $n = 2$ ), and indicated by the second brackets between the dotted lines. There are no energy levels between the dotted lines at  $\frac{\pi^2}{a^2}$  (for  $n = 1$ ) and at  $\frac{9\pi^2}{a^2}$  (for  $n = 3$ ) within the ring but there are propagating states in the leads. In these energy regimes, the electrons tunnel through as evanescent modes described by Eq. (6.23) - Eq. (6.26).

Note that a two dimensional quantum wire can be also converted into a Aharonov-Bohm set up as shown in Fig. 6.3. Essentially one can form a cylinder that can enclose a flux [102]. In this case all the analysis given above remains the same. For example if now we choose cylindrical coordinates the wave function in Eq. (6.19) becomes

$$\psi_{(II)_1}^{(1)} = \left( \frac{A_1^{(1)} e^{im_1\theta}}{\sqrt{m_1}} + \frac{B_1^{(1)} e^{-im_1\theta}}{\sqrt{m_1}} \right) \sin \frac{\pi}{a} \left( z + \frac{a}{2} \right) \quad (6.29)$$

In fact this makes analysis much simpler because  $m_1$  stands for angular momentum

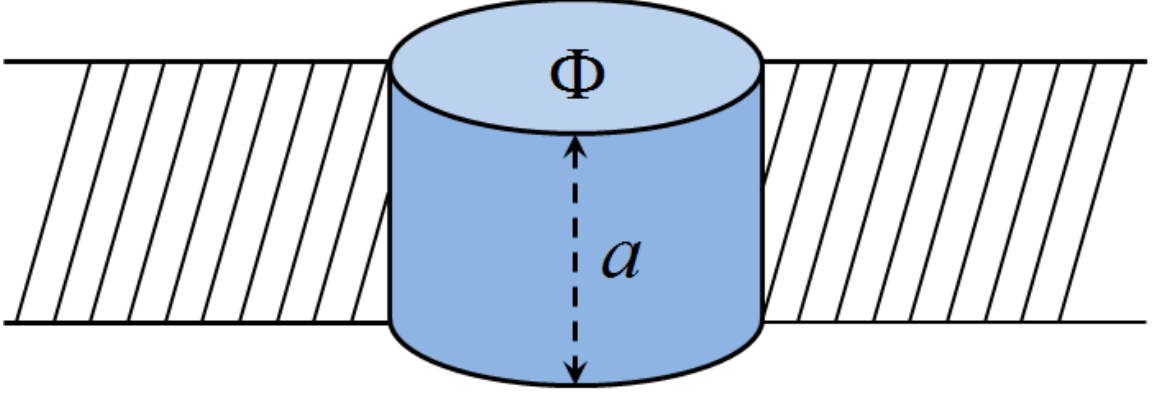


Figure 6.3: Cylindrical Aharonov-Bohm set up

and takes into account the curvature of the ring. The advantage of this set up is already described by S. Mukherjee et al. [112, 113].

In our work (see Ref. [112, 113]) we proposed a junction scattering matrix  $S$  for a multi-channel junction that can be easily generalized to any number of channels. One can match the wave functions depicted in Fig. 6.1 at junction J1 and J2 and conserve the currents by using these  $S$ -matrices that give us a set of linear equations. For evanescent modes the internal wavefunctions has to be appropriately chosen, given by Eqs. (6.23) - (6.26). We can calculate the coefficients  $A_1^{(1)}$ ,  $A_2^{(1)}$ ,  $B_1^{(1)}$ ,  $B_2^{(1)}$ ,  $A_1^{(2)}$ ,  $A_2^{(2)}$ ,  $B_1^{(2)}$ ,  $B_2^{(2)}$ ,  $C_1^{(1)}$ ,  $C_2^{(1)}$ ,  $D_1^{(1)}$ ,  $D_2^{(1)}$ ,  $C_1^{(2)}$ ,  $C_2^{(2)}$ ,  $D_1^{(2)}$  and  $D_2^{(2)}$  by matrix inversion.

The general definition of current ( $I$ ) is given by

$$I = \int_{-\frac{a}{2}}^{\frac{a}{2}} \frac{e\hbar}{2im^*} (\Psi^\dagger \vec{\nabla} \Psi - \Psi \vec{\nabla} \Psi^\dagger) dy \quad (6.30)$$

We are considering that there are two channels (modes) in the ring, which are both propagating. The current ( $I$ ) in propagating mode is obtained by calculating Eq. (6.30) for wave functions given by equations from Eq. (6.19) to Eq. (6.22). For such propagating mode in upper arm, for incidence along channel 1, the partial current is given by

$$I_U^{(1)}(pro) = \frac{e\hbar}{m^*} [|A_1^{(1)}|^2 - |B_1^{(1)}|^2 + |A_2^{(1)}|^2 - |B_2^{(1)}|^2] \quad (6.31)$$

For propagating mode in upper arm, for incidence along channel 2, the partial current is given by

$$I_U^{(2)}(pro) = \frac{e\hbar}{m^*} [|A_1^{(2)}|^2 - |B_1^{(2)}|^2 + |A_2^{(2)}|^2 - |B_2^{(2)}|^2] \quad (6.32)$$

Similarly, for propagating mode in lower arm, for incidence along channel 1 and 2,

the partial currents are given by

$$I_L^{(1)}(pro) = \frac{e\hbar}{m^*}[|C_1^{(1)}|^2 - |D_1^{(1)}|^2 + |C_2^{(1)}|^2 - |D_2^{(1)}|^2] \quad (6.33)$$

and

$$I_L^{(2)}(pro) = \frac{e\hbar}{m^*}[|C_1^{(2)}|^2 - |D_1^{(2)}|^2 + |C_2^{(2)}|^2 - |D_2^{(2)}|^2] \quad (6.34)$$

When both modes are propagating using Eqs. (6.31) and (6.32) we can write the net current in upper arm as

$$I_U = I_U^{(1)}(pro) + I_U^{(2)}(pro) \quad (6.35)$$

When both modes are propagating using Eqs. (6.33) and (6.34) we can write the net current in lower arm as

$$I_L = I_L^{(1)}(pro) + I_L^{(2)}(pro) \quad (6.36)$$

Next we consider that there are two channels (modes) in the ring, one being propagating and other being evanescent. The current ( $I$ ) using one propagating mode and one evanescent mode is obtained by calculating Eq. (6.30) choosing the wavefunctions appropriately for propagating mode and evanescent mode given in Eq. (6.19) to Eq. (6.26). In this case in upper arm for incidence along channel 1 the partial current is given by

$$I_U^{(1)}(pe) = \frac{e\hbar}{m^*}[|A_1^{(1)}|^2 - |B_1^{(1)}|^2] + \frac{e\hbar}{im^*}[A_2^{(1)*} B_2^{(1)} e^{-i\alpha} - A_2^{(1)} B_2^{(1)*} e^{i\alpha}] \quad (6.37)$$

For one propagating mode and one evanescent mode in upper arm, for incidence along channel 2, the partial current is given by

$$I_U^{(2)}(pe) = \frac{e\hbar}{m^*}[|A_1^{(2)}|^2 - |B_1^{(2)}|^2] + \frac{e\hbar}{im^*}[A_2^{(2)*} B_2^{(2)} e^{-i\alpha} - A_2^{(2)} B_2^{(2)*} e^{i\alpha}] \quad (6.38)$$

Similarly, for one propagating mode and one evanescent mode in lower arm, for incidence along channel 1 and 2, the partial currents are given by

$$I_L^{(1)}(pe) = \frac{e\hbar}{m^*}[|C_1^{(1)}|^2 - |D_1^{(1)}|^2] + \frac{e\hbar}{im^*}[C_2^{(1)*} D_2^{(1)} e^{-i\alpha} - C_2^{(1)} D_2^{(1)*} e^{i\alpha}] \quad (6.39)$$

and

$$I_L^{(2)}(pe) = \frac{e\hbar}{m^*}[|C_1^{(2)}|^2 - |D_1^{(2)}|^2] + \frac{e\hbar}{im^*}[C_2^{(2)*} D_2^{(2)} e^{-i\beta} - C_2^{(2)} D_2^{(2)*} e^{i\beta}] \quad (6.40)$$

For using one propagating mode and one evanescent mode the net current in upper

arm is given by

$$I_U = I_U^{(1)}(pe) + I_U^{(2)}(pe) \quad (6.41)$$

For using one propagating mode and one evanescent mode the net current in lower arm is given by

$$I_L = I_L^{(1)}(pe) + I_L^{(2)}(pe) \quad (6.42)$$

Next we consider that both the channels are evanescent. The current ( $I$ ) for two evanescent modes is obtained by calculating Eq. (6.30) choosing the wavefunctions appropriately for evanescent modes given in Eq. (6.23) to Eq. (6.26). For such evanescent modes the partial current in upper arm, for incidence along channel 1 is given by

$$I_U^{(1)}(eva) = \frac{e\hbar}{im^*} [A_1^{(1)*} B_1^{(1)} e^{-i\alpha} - A_1^{(1)} B_1^{(1)*} e^{i\alpha} + A_2^{(1)*} B_2^{(1)} e^{-i\alpha} - A_2^{(1)} B_2^{(1)*} e^{i\alpha}] \quad (6.43)$$

For evanescent mode the partial current in upper arm, for incidence along channel 2 is given by

$$I_U^{(2)}(eva) = \frac{e\hbar}{im^*} [A_1^{(2)*} B_1^{(2)} e^{-i\alpha} - A_1^{(2)} B_1^{(2)*} e^{i\alpha} + A_2^{(2)*} B_2^{(2)} e^{-i\alpha} - A_2^{(2)} B_2^{(2)*} e^{i\alpha}] \quad (6.44)$$

Similarly, for evanescent mode in lower arm and incidence along channel 1 and 2, the partial currents are given by

$$I_L^{(1)}(eva) = \frac{e\hbar}{im^*} [C_1^{(1)} D_1^{(1)*} e^{i\beta} - C_1^{(1)*} D_1^{(1)} e^{-i\beta} + C_2^{(1)} D_2^{(1)*} e^{i\beta} - C_2^{(1)*} D_2^{(1)} e^{-i\beta}] \quad (6.45)$$

and

$$I_L^{(2)}(eva) = \frac{e\hbar}{im^*} [C_1^{(2)} D_1^{(2)*} e^{i\beta} - C_1^{(2)*} D_1^{(2)} e^{-i\beta} + C_2^{(2)} D_2^{(2)*} e^{i\beta} - C_2^{(2)*} D_2^{(2)} e^{-i\beta}] \quad (6.46)$$

From Eqs. (6.43) and (6.44) we can write for evanescent modes the net current in upper arm is given by

$$I_U = I_U^{(1)}(eva) + I_U^{(2)}(eva) \quad (6.47)$$

Similarly, from Eqs. (6.45) and (6.46) we can write for evanescent modes net current in lower arm is given by

$$I_L = I_L^{(1)}(eva) + I_L^{(2)}(eva) \quad (6.48)$$

The magnetic induction  $\vec{B}$  at the position  $\vec{x}$  generated by the current induced by A-B flux is given by the Biot and Savart law [114]

$$d\vec{B} = \frac{kI(d\vec{l} \times \vec{x})}{|\vec{x}|^3}$$

where  $\vec{x}$  is the position vector. For the geometry described in Fig. 6.1 we will calculate  $(I_U.l_U + I_L.l_L)$  taking two propagating modes using Eq. (6.35) and Eq. (6.36), taking one propagating and one evanescent mode using Eq. (6.41) and Eq. (6.42) and taking two evanescent modes using Eq. (6.47) and Eq. (6.48) which will give the strength of magnetization.

## 6.3 Results and Discussions

### 6.3.1 Conductance of a multi-channel A-B ring

We are considering two channel A-B ring that are characterized by four transmission amplitudes  $t_1^{(1)}$ ,  $t_2^{(1)}$ ,  $t_1^{(2)}$  and  $t_2^{(2)}$  and four reflection amplitudes  $r_1^{(1)}$ ,  $r_2^{(1)}$ ,  $r_1^{(2)}$  and  $r_2^{(2)}$ . Landauer's formula gives the two probe conductance  $G$  as

$$G = \frac{2e^2}{h} \sum_{i,j} |t_j^{(i)}|^2. \quad (6.49)$$

The transmission amplitude from mode  $i$  to mode  $j$  is  $t_j^{(i)}$ .  $G$  is a strongly oscillating function of  $\phi/\phi_0$  implying we can use flux to drive the system from a conducting state to an insulating state. In case of a triode, we can use grid voltage to change the current flow from cathode to anode and therefore use it as a switch or a transistor. Similarly, in this A-B set up we can use magnetic field to control the current from source to drain and similarly we can use it as a switch or a transistor.

In an A-B ring, switching action is based on constructive and destructive interference and is extremely sensitive to small changes in parameters like Fermi energy, ring length, arm lengths etc. They are practically impossible to control [89]. This fact changes completely if we use evanescent modes [112]. An electron in an evanescent mode do not acquire phase changes associated with propagation or impurity scattering. Only phase changes are due to A-B effect and we find that within a period (0 to  $2\pi$ ) conductance is maximum (or minimum) at zero flux, then it goes through a deep minimum (or a maximum) and rises (or falls) again to a maximum (or minimum) value. One can explain this as follows. Conductance being a symmetric function of flux (Onsager reciprocity relation), is a function of  $(\cos n\phi/\phi_0)$ . So it maximizes (or minimizes) at 0 flux and then decreases (or increases) with flux. Periodicity is always  $\phi_0$  in absence of other competing source of phase changes and absence of resonance. This behavior is independent of all parameters. Since evanescent modes are not very conducting we have to take smaller rings. A plot of the conductance is shown in Fig. 6.4 that exhibits this.

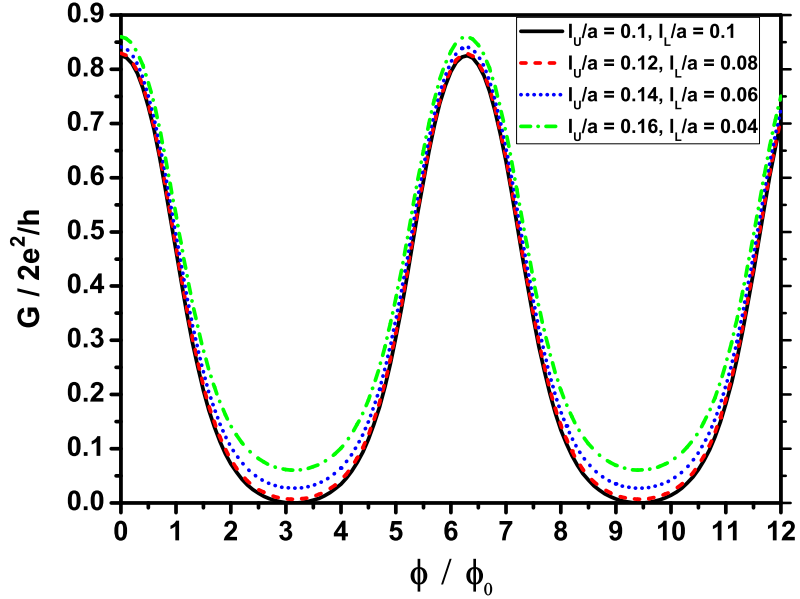


Figure 6.4: The figure shows plot of conductance,  $G/\frac{2e^2}{h}$  as a function of  $\phi/\phi_0$  using evanescent modes for different arm lengths. Total ring length is the same in all cases. Here  $\phi_0 = hc/e$ . The energy of incident electrons,  $E = \frac{49\hbar^2}{m^*a^2}$ . The exact values of  $l_U$  and  $l_L$  are given in the figure inset. For all sets of arm lengths  $G/\frac{2e^2}{h}$  as a function of  $\phi/\phi_0$  have the same nature.

### 6.3.2 Circulating current in a multi-channel A-B ring

According to Landauer-Büttiker formalism, when  $l_U = l_L$ , the current through the entire system (or sample) ( $I_S$ ) splits at junction J1 and divides into two parts, the upper arm current,  $I_U$  (i.e.,  $I_S/2$ ) flows in clockwise direction along upper arm of the ring and the lower arm current,  $I_L$  (i.e.,  $I_S/2$ ) flows in anti-clockwise direction along lower arm of the ring. These two currents are equal in magnitude. When  $l_U \neq l_L$ , in absence of flux, these two currents are different in magnitude. Büttiker [115] suggested that this difference arises due to a circulating current,  $I_c$ , such that the current in the upper arm is then given by  $I_U = I_S/2 + I_c$ , and the current in the lower arm is given by  $I_L = I_S/2 - I_c$ . However, if this definition is taken seriously, then even in a classical ring with different resistances in different arms one obtains different currents in the presence of a dc current and hence circulating current. It is clear then that with this definition one can obtain circulating current even classically without invoking quantum mechanics at all. However, ten years after Büttiker's discussion, in 1995, Jayannavar and Deo [116] showed that there exists two distinct possibilities depending on the choice of  $l_U, l_L$  ( $l_U \neq l_L$ ) and Fermi energy. In the first possibility, for a certain range of incident Fermi energies (or wave vectors),

the current in the two arms  $I_U$  and  $I_L$  are individually less than the total current through the system (or sample)  $I_S$ , such that  $I_S = (I_U + I_L)$ . (the conservation of current or Kirchhoff's law). Then currents in two arms flow in the direction of the applied field. In such a situation we do not assign any circulating current flowing in the ring. However, in a certain energy interval, it turns out that current in one arm is larger than the total current  $I_S$  (*magnification property*). This implies that, to conserve the total current at the junctions, the current in the other arm must be negative or should flow against the applied external field induced by difference in the chemical potentials. In such a situation one can interpret that the negative current flow in one arm of the ring continues to flow in the ring as a circulating current. The direction of circulating current can be inferred as follows. First we consider a case when the net current flows in the right direction, i.e.,  $\mu_1 > \mu_2$ . If for this case, the negative current flows in the lower arm, then the circulating current flows in a clockwise (or positive) direction. If, on the other hand, the negative current flows in the upper arm, then the circulating current flows in an anti-clockwise (or negative) direction. The negative current in one arm is a purely quantum mechanical effect. This procedure of assigning circulating current only when negative current flows in one of the arms is the same procedure that is well known in classical ac network analysis [117]. It is well known that, when a parallel resonant circuit (capacitance  $C$  connected parallel with a combination of inductance  $L$  and resistance  $R$ ) is driven by external electromotive force (generator), the circulating current arises in an LCR circuit at a resonant frequency. This effect is sometimes referred to as a *current magnification*. In this classical network, when the external driving frequency is around a resonance frequency, circulating currents are possible. Moreover, at the resonance the total net current amplitude in the circuit is at its minimum value. It turns out that even in quantum problem the circulating current arises near the antiresonances or transmission zeros of the ring structure coupled to leads. Interestingly this circulating current can lead to a large orbital magnetic moment in absence of magnetic field, however in a non-equilibrium situation. Based on the constraints on the local currents, Jayannavar et al. [116, 118] showed the existence of a circulating current in a one dimensional mesoscopic ring with asymmetric arm lengths in the absence of an Aharonov-Bohm flux. This circulating current had nothing to do with the Aharonov-Bohm flux but it was named the persistent current in the presence of a transport current. The unique behaviors of circulating currents have been studied in various types of interferometers, such as single loop interferometers with a stub [119] or impurity potential [120, 121] embedded in one of arm, an evanescent wave interferometer with a potential well [122], a multichannel interferometer with an impurity [123], double-loop interferometers [124, 125], double quantum dot interferometers [126, 127], multiple-arm interferometers [128, 129], and spin-dependent interferometers [129, 130, 131]. In such interferometers, circulating heat [127] and

spin [129, 130, 131] currents have been reported, as well as electric circulating currents. In 2010, Su et. al. [132] formulated the constraint condition for circulating current as follows:

$$I_c = \frac{1}{2} \text{sign}[I_U] (|I_U| + |I_L| - I(S)) \quad (6.50)$$

The above equation (there is a missing factor,  $\text{sign}[I_U]$  or  $-\text{sign}[I_L]$ , which is responsible for the direction of the circulating current, in the expression for the circulating current which was introduced for the first time in Ref. [124]) shows that not just any classical parallel resistor can have a circulating current. The definition then allows us to capture a pure quantum mechanical effect for electron transport through a two-terminal interferometer.

We plot circulating current as well as transmission coefficient as a function of incident Fermi energy for the mesoscopic ring considered in Fig. 6.1. The transmis-

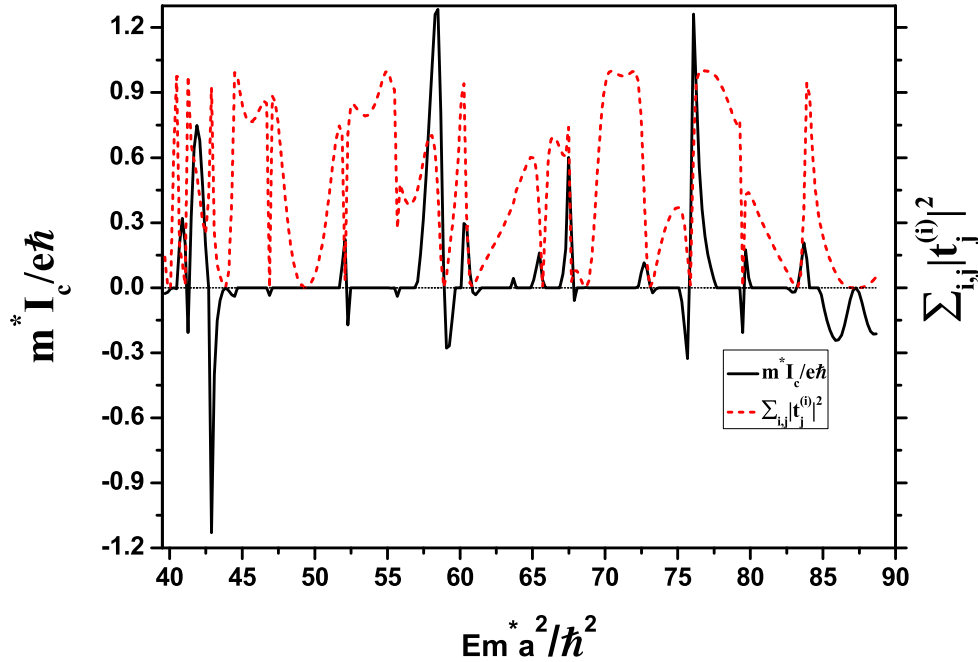


Figure 6.5: The figure shows plot of circulating current ( $I_c$ ) in the dimensionless units as a function of incident Fermi energy (solid curve) and transmission coefficient ( $\sum_{i,j} |t_j^{(i)}|^2$ ) as a function of incident Fermi energy (dashed curve) using two propagating modes. Here upper arm length,  $l_U/a = 3$  and lower arm length,  $l_L/a = 7$ .

sion coefficient across a metallic ring connected to two reservoirs and in the presence of magnetic flux has been investigated by several authors [133, 134], in connection with the Aharonov-Bohm effect. We first consider a case where both the channels (modes) in the ring are propagating described in Eq. (6.35) and Eq. (6.36). In

Fig. 6.5 we have plotted the circulating current,  $I_c$  (solid curve) as a function of incident Fermi energy. We have taken  $l_U/a = 3$  and  $l_L/a = 7$ . In Fig. 6.5 we have also plotted the transmission coefficient,  $\sum_{i,j} |t_j^{(i)}|^2$  as a function of incident Fermi energy (dashed curve). We notice that the circulating current appears as we cross the energy at  $I_S = 0$ .

Now we will consider the case where one mode is propagating and the other mode is evanescent described in Eq. (6.41) and Eq. (6.42). In Fig. 6.6 we have plotted circulating current, ( $I_c$ ) (solid curve) as a function of Fermi energy of incident electrons. We have taken  $l_U/a = 3$  and  $l_L/a = 7$ . In Fig. 6.6 we have also plotted the transmission coefficient,  $\sum_{i,j} |t_j^{(i)}|^2$  as a function of Fermi energy (dashed curve). We notice that the circulating current appears as we cross the energy at  $I_S = 0$ .

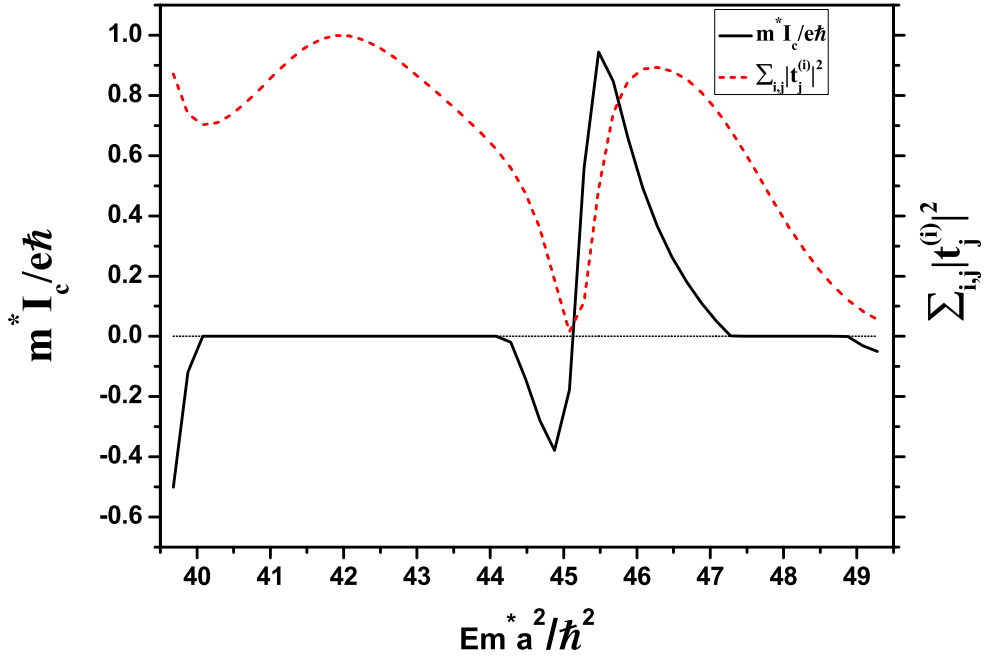


Figure 6.6: The figure shows plot of circulating current ( $I_c$ ) in dimensionless unit as a function of incident Fermi energy (solid curve) and transmission coefficient ( $\sum_{i,j} |t_j^{(i)}|^2$ ) as a function of Fermi energy of incident electrons (dashed curve) using one propagating mode and one evanescent mode. Here upper arm length is  $l_U/a = 3$  and lower arm length is  $l_L/a = 7$ .

When both modes are evanescent then there is no circulating current in the system.

### 6.3.3 Magnetization of a multi-channel A-B ring

The geometry in consideration (Fig. 6.1, Fig. 6.2, Fig. 6.3) can have a magnetization due to internal currents in regions II and III. A proper formulation for evaluating such internal currents in the regime of evanescent modes is still not well established [116, 118] and the correct formalism that gives consistent results in every situation is given in Eqs. (6.31) - (6.48). This internal current can induce a magnetic field that can be measured. There are two different origins for this magnetization. The first origin of magnetization is due to transport current and this magnetization can be there even in absence of the A-B flux. The sample current  $I_S$  splits up into  $I_U$  and  $I_L$  in upper arm and lower arm, respectively. For  $l_U \neq l_L$ ,  $I_U \neq I_L$  and thus the clockwise current is different from anticlockwise current. This can result in a magnetization, magnetization strength is given by  $(I_U.l_U + I_L.l_L)$ . The current in lower arm,  $I_L$  by definition is negative. In regimes of circulating current  $I_L$  becomes positive leading to a huge enhancement in magnetization which is shown in Fig. 6.7 where we have plotted magnetization strength as a function of Fermi energy where flux value is taken as 0 using two propagating modes.

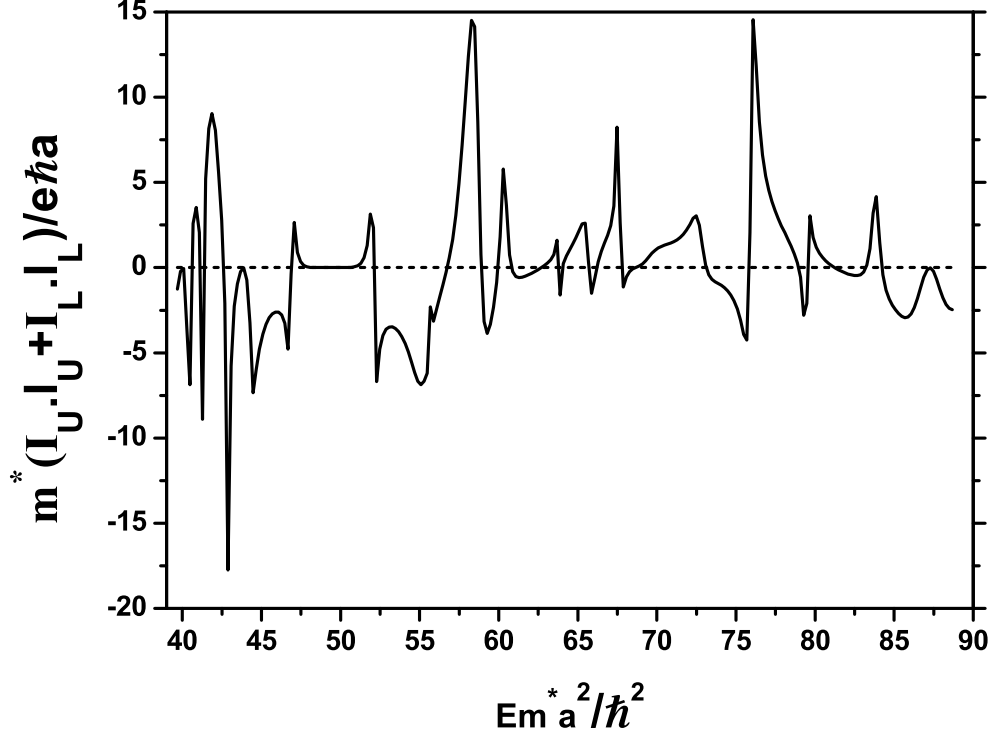


Figure 6.7: The figure shows plot of magnetization strength in dimensionless unit as a function of Fermi energy using two propagating modes. Here upper arm length,  $l_U/a = 3$  and lower arm length,  $l_L/a = 7$ .

The second origin of magnetization is due to the A-B flux and this magnetization can exist even if  $\mu_1 = \mu_2$  and there is no incident current. A-B flux induces an equilibrium current and this current is always an odd function of flux [103]. The first kind of magnetization is further modified by the flux but is always an even function of flux. It is known that the odd component can be determined from the even component [111]. Besides, the even component can give the odd component in the analytically continued regime where the even component is absent. Therefore, if one decides to construct a device with closed rings without any connection to external reservoirs our analysis is general to give the magnetization even in that regime. The total magnetization is therefore a linear combination of an even and an odd function of flux and hence can be any arbitrary function of flux. It will be a function of  $\cos(n\phi/\phi_0)$  as well as  $\sin(n\phi/\phi_0)$ . Therefore unlike the conductance it will not maximize (or minimize) at 0 flux and then decreases (or increases) with flux. It can maximize at any arbitrary flux. Therefore it remains to be seen if magnetization due to evanescent modes remain independent of material parameters. If it does then one can build stable devices that rely on magnetization instead of conductance.

In Fig. 6.8 (a), (b) and (c), we have plotted the strength of magnetization, i.e.,  $I_U.l_U + I_L.l_L$  as a function of  $\phi/\phi_0$  for different parameters like different arm lengths, different Fermi energies, different ring lengths, respectively using two propagating modes. In Fig. 6.8 (a), we are taking Fermi energy of the incident electrons as  $E = \frac{55\hbar^2}{m^*a^2}$ . Keeping the total ring length ( $L = l_U + l_L$ ) same we have taken two different choices of arm length ratio ( $l_U : l_L$ ) indicated by solid line and dashed lines. Upper and lower arm lengths for solid and dashed lines are shown in figure caption. The maximum of the solid line and the maximum of the dashed line are not obtained at the same flux value. Similar situation arises for the minimum also. Thus, the behavior of the solid line and the dashed line is not uniform. In Fig. 6.8 (b), we are choosing two different Fermi energies of the incident electrons keeping the arm length value as  $l_U/a = 5$ ,  $l_L/a = 5$ , indicated by the solid and dashed lines. The energy values are shown in figure caption. The maximum and the minimum for solid and dashed lines are not obtained at the same flux values. Thus, the behavior of the solid and the dashed lines are not uniform. In Fig. 6.8 (c) keeping the arm length ratio ( $l_U : l_L$ ) same we have taken two different choices of total ring length ( $L/a = l_U/a + l_L/a$ ) for incident Fermi energy,  $E = \frac{55\hbar^2}{m^*a^2}$ . The ring lengths for solid and dashed lines are shown in figure caption. The maximum of the solid line and the maximum of the dashed line are not obtained at the same flux value. Similar situation arises for the minimum also. While the solid line goes up with increasing flux values, the dashed line goes down, reaches the minimum and then rises up. Fig. 6.8 (c) is also showing non uniform behavior. Thus we can conclude that using propagating modes we can not build reliable devices based on magnetic properties.

In Fig. 6.9 (a), (b) and (c), we have plotted the strength of magnetization,

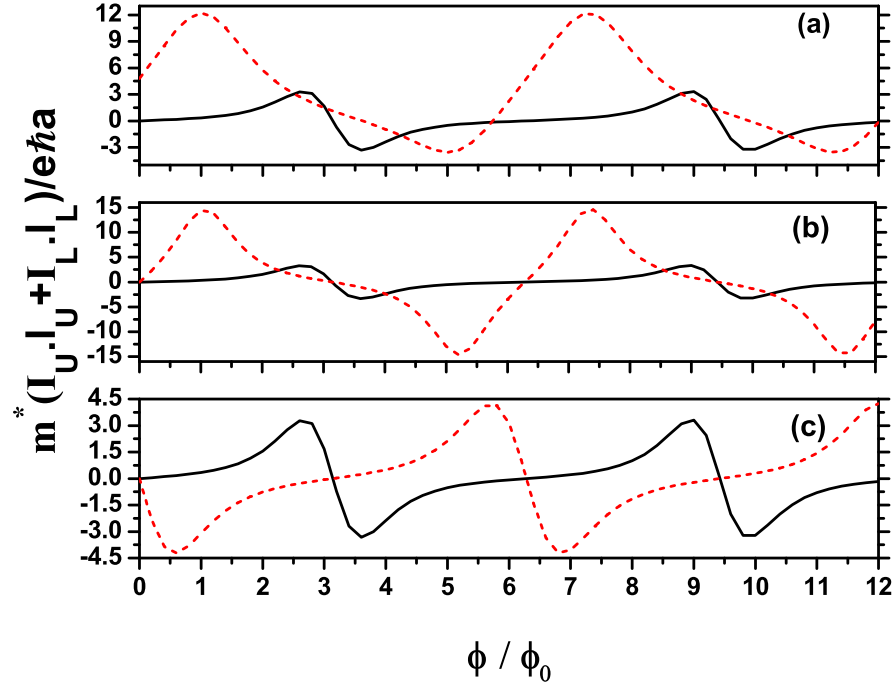


Figure 6.8: The figures (a) - (c) show plot of magnetization strength in dimensionless unit as a function of  $\phi/\phi_0$  for different choice of parameters. Here  $\phi_0 = hc/e$ . The constant potential  $V_0$  is taken as 0, so that both the modes are propagating. In (a), the incoming electrons have energy  $E = \frac{55\hbar^2}{m^*a^2}$ . The solid line is for  $l_U/a = 5, l_L/a = 5$  and the dashed line is for  $l_U/a = 4, l_L/a = 6$ . In (b) the arm length ratio is taken as  $l_U : l_L = 5 : 5$ . The solid line is for  $E = \frac{55\hbar^2}{m^*a^2}$  and the dashed line is for  $E = \frac{57\hbar^2}{m^*a^2}$ . In (c), the incoming electrons have energy  $E = \frac{55\hbar^2}{m^*a^2}$ . Keeping the arm length ratio same ( $l_U : l_L = 1 : 1$ ) we have taken here different ring lengths. The solid line is for  $L/a = 10$  and the dashed line is for  $L/a = 8$ .

i.e.,  $I_U.l_U + I_L.l_L$  as a function of  $\phi/\phi_0$  for different parameters like different arm lengths, different Fermi energies and different ring lengths, respectively using one propagating mode and one evanescent mode. We have demonstrated that such a situation results in just as much diversity as that with two propagating modes. In Fig. 6.9 (a), we have taken Fermi energy  $E = \frac{45\hbar^2}{m^*a^2}$  and keeping the total ring length same, we have taken two different choices of arm lengths ratio indicated by the solid and dashed lines. Upper and lower arm lengths for solid and dashed lines are shown in figure caption. With increasing the flux values, the solid line goes down whereas the dashed line rises up steeply. The solid line has no well defined maximum whereas the dashed line has sharp maximum. Thus the behavior of the solid line and the dashed line is not uniform. In Fig. 6.9 (b) we are choosing two different Fermi energies of the incident electrons keeping the arm length value as  $l_U/a = 1, l_L/a = 1$ , indicated by the solid and the dashed lines. The energy values are shown in figure

caption. The solid line goes down with increasing the flux whereas the dashed line rises up with increasing the flux value and has sharp maximum. Similar situation arises for the minimum also. Thus the behavior of the solid line and the dashed line is not uniform. In Fig. 6.9 (c), keeping the arm length ratio same we have taken two different choices of total ring length ( $L = l_U + l_L$ ), for incident Fermi energy  $E = \frac{45\hbar^2}{m^*a^2}$ . The ring length for solid line and dashed lines are shown in figure caption. The solid line goes down with increasing the flux value, but has no sharp maximum. The dashed line goes down with increasing the flux value, after reaching minimum it again goes up, but it has sharp maximum and minimum unlike the solid line. Thus the behavior of the solid and the dashed line is not uniform in all three Figs. 6.9 (a), (b) and (c). Thus we can conclude that using one propagating mode and one evanescent mode also we can not build reliable devices based on magnetic properties.

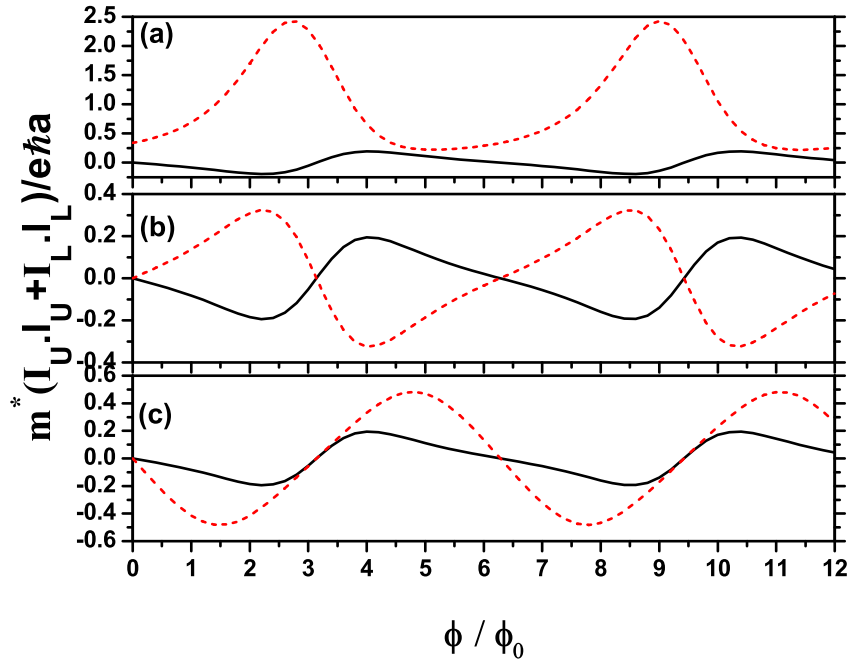


Figure 6.9: The figures (a) - (c) show plot of magnetization strength in dimensionless unit as a function of  $\phi/\phi_0$ . The constant potential  $V_0$  of the ring is such that  $V_0 = 10\hbar^2/em^*a^2$ . With this choice  $q_1$  is real and  $q_2$  is imaginary. Thus we are considering in this case one propagating mode and one evanescent mode. In (a), the incoming electrons have energy  $E = \frac{45\hbar^2}{m^*a^2}$ . The solid line is for  $l_U/a = 1, l_L/a = 1$  and the dashed line is for  $l_U/a = 1.2, l_L/a = 0.8$ . In (b) the arm length ratio is taken as  $l_U : l_L = 1 : 1$ . The solid line is for  $E = \frac{45\hbar^2}{m^*a^2}$  and the dashed line is for  $E = \frac{47\hbar^2}{m^*a^2}$ . In (c), the incoming electrons have energy  $E = \frac{45\hbar^2}{m^*a^2}$ . Keeping the arm length ratio same ( $l_U : l_L = 1 : 1$ ) we have taken here different ring lengths. The solid line is for  $L/a = 2$  and the dashed line is for  $L/a = 1.6$ .

Taking both the current carrying modes as propagating modes, we have shown in Fig. 6.8 (a), (b) and (c), that the magnetization behavior is not uniform for different parameters like different arm lengths, different Fermi energies, different ring lengths, respectively. Thereafter, taking one current carrying mode as propagating and the other mode as evanescent, we have shown in Fig. 6.9 (a), (b) and (c) that the magnetization behavior is not uniform for different parameters like different arm lengths, different Fermi energies, different ring lengths, respectively. Thus, using two propagating modes or using one propagating and one evanescent mode we can not build stable devices based on magnetic properties which supports earlier works [89] in one-dimension.

In Fig. 6.10 (a), (b) and (c), we have plotted magnetization strength  $I_U.l_U + I_L.l_L$  as a function of  $\phi/\phi_0$  for different parameters using two evanescent modes ( $V_0 = 40\hbar^2/em^*a^2$ ). In Fig. 6.10 (a), we have chosen the energy  $E = \frac{45\hbar^2}{m^*a^2}$  and taken three cases indicated by the solid, dashed and dotted lines where the arm length ratios are different keeping the total ring length value same. The arm length ratio for these three cases are described in figure caption. All three cases gives  $I_U.l_U + I_L.l_L$  value similar as a function of flux,  $\phi/\phi_0$ . In Fig. 6.10 (b), we have taken A-B ring length as  $L/a = 0.2$ . It is not always possible to maintain the Fermi energy ( $Em^*a^2/\hbar^2$ ) values constant due to statistical fluctuation in voltage of the battery or due to temperature changes. In this figure we have taken three cases where the Fermi energy values for incoming electrons (described in figure caption) are different. Here we have shown the value of magnetization strength as a function of flux is independent of incident energy when we employ evanescent modes. In Fig. 6.10 (c), we have taken the incidence energy as  $E = \frac{45\hbar^2}{m^*a^2}$  and have chosen three different total ring length values keeping the ratio of arm lengths same. The ring length for solid, dashed and dotted lines are described in figure caption. Here the nature of these three lines are the same as that obtained so far. In Fig. 6.10 (a), (b) and (c) we have shown that the strength of magnetization  $I_U.l_U + I_L.l_L$  as a function of  $\phi/\phi_0$  is qualitatively as well as quantitatively same for all variations in parameters like different ratio of arm lengths (Fig. 6.10 (a)), different Fermi energy (Fig. 6.10 (b)), different total ring length (Fig. 10 (c)) etc. So there is possibility of robust device action based on magnetic response using only evanescent modes which contradicts earlier works that devices based on quantum interference effects cannot be achieved. Note that the maximum or the minimum in figures (Fig. 6.10 (a), (b) and (c)) is not at 0 flux as we have argued. However the maxima and minima are fixed and do not change with change in parameters. The reason for this is explained as for evanescent modes the two arms behave as classical resistor.

So far we have considered three different cases - (i) keeping Fermi energy value and ring length fixed, we have chosen three different sets of arm lengths, (ii) keeping arm length and ring length fixed, we have chosen three different sets of Fermi

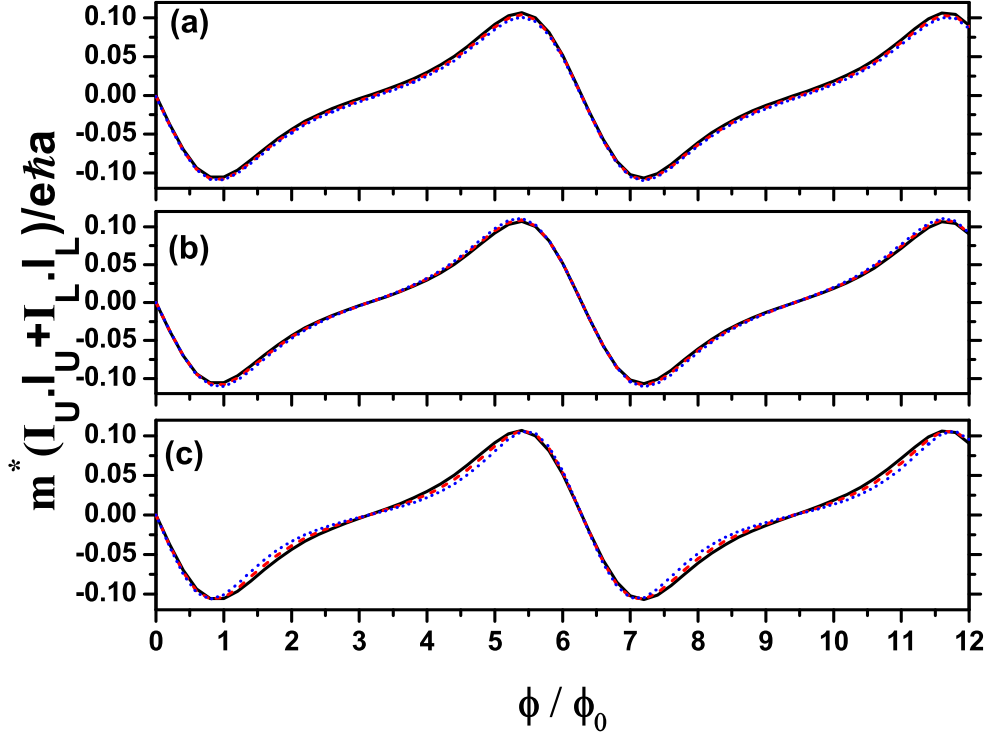


Figure 6.10: The figures (a) - (c) show plots of magnetization strength as a function of  $\phi/\phi_0$  for an Aharonov-Bohm interferometer where all the current carrying modes are evanescent. Here  $\phi_0 = hc/e$ . In (a), the incoming electrons have energy  $E = \frac{45\hbar^2}{m^*a^2}$ . The solid line is for  $l_U/a = 0.1, l_L/a = 0.1$ , the dashed line is for  $l_U/a = 0.12, l_L/a = 0.08$  and the dotted line is for  $l_U/a = 0.14, l_L/a = 0.06$ . All three plots show nature of magnetization is independent of relative ratio of arm lengths. In (b), the arm length ratio is taken as  $l_U : l_L = 0.1 : 0.1$ . The solid line is for  $E = \frac{45\hbar^2}{m^*a^2}$ , the dashed line is for  $E = \frac{46\hbar^2}{m^*a^2}$  and the dotted line is for  $E = \frac{47\hbar^2}{m^*a^2}$ . All three plots show nature of magnetization is independent of Fermi energy. In (c), the incoming electrons have energy  $E = \frac{45\hbar^2}{m^*a^2}$ . Keeping the arm length ratio same ( $l_U : l_L = 1 : 1$ ) we have taken here different ring lengths. The solid line is for  $L/a = 0.2$ , the dashed line is for  $L/a = 0.18$  and the dotted line is for  $L/a = 0.16$ . All three plots show nature of magnetization is independent of total ring length.

energies, and (iii) keeping Fermi energy value and arm length fixed, we have chosen three different sets of ring lengths. Now we will discuss another set of plots where we have chosen incident Fermi energy and electrostatic potentials inside the ring in such a fashion that both the channels are evanescent and sample parameters being chosen randomly. In Fig. 6.11 (a) and (b), we have plotted magnetization strength as a function of  $\phi/\phi_0$  for different parameters. In Fig. 6.11 (a), we have chosen the energy  $E = \frac{45\hbar^2}{m^*a^2}$  and taken two different cases indicated by solid and dashed lines. The ring length and arm length ratio are described in figure caption. The solid line

and the dashed lines are qualitatively as well as quantitatively same. In Fig. 6.11 (b), we have chosen the energy  $E = \frac{47\hbar^2}{m^*a^2}$  and taken two different cases indicated by solid and dashed lines. The ring length and arm length ratio are described in figure caption. Here also the solid lines and the dashed lines are qualitatively as well as quantitatively same.

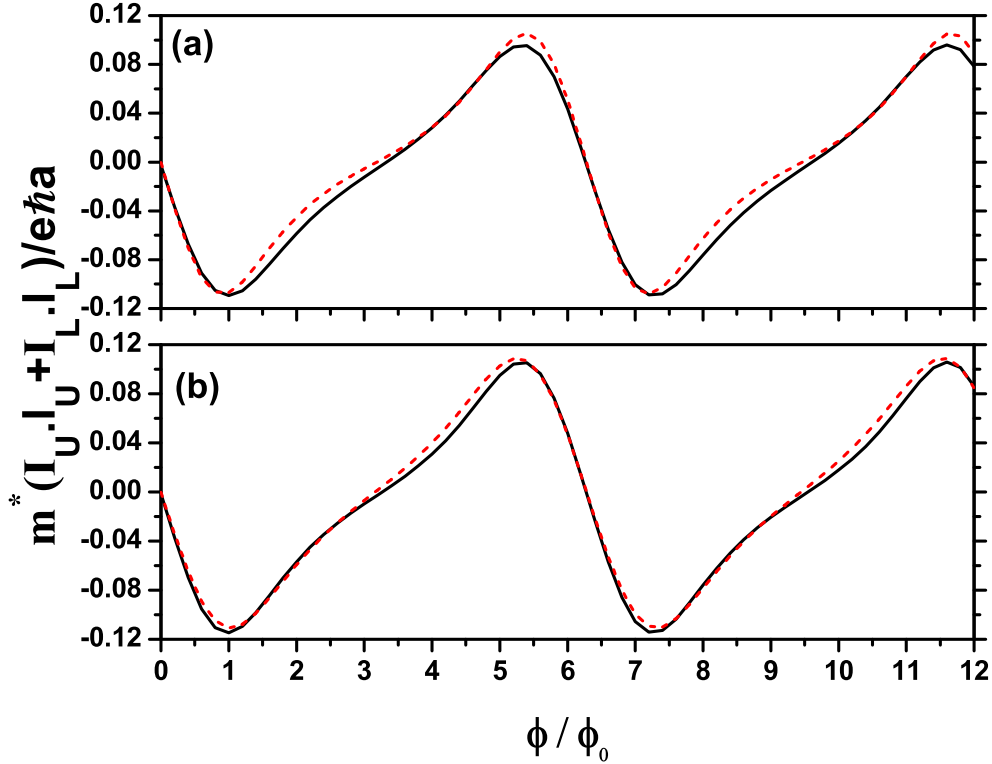


Figure 6.11: The figures (a) - (b) show plot of magnetization strength as a function of  $\phi/\phi_0$  for an Aharonov-Bohm interferometer where all the current carrying modes are evanescent. Here  $\phi_0 = hc/e$ . In (a), the incoming electrons have energy  $E = \frac{45\hbar^2}{m^*a^2}$ . The solid line is for  $L/a = 0.24$  and the dashed line is for  $l_U/a = 0.11, l_L/a = 0.09$ . In (b), the incoming electrons have energy  $E = \frac{47\hbar^2}{m^*a^2}$ . The solid line is for  $L/a = 0.22$  and the dashed line is for  $l_U/a = 0.13, l_L/a = 0.12$ . Here (a) and (b) shows that plots are independent of material parameters.

As we have argued before the current in the upper arm ( $I_U$ ) and that in the lower arm ( $I_L$ ) has an even (in  $\phi$ ) contribution and an odd contribution. Now we analyze the even current and the odd current separately. The even current is transport current which is given by

$$I_{U,L}^{even} = \frac{I_{U,L}(\phi) + I_{U,L}(-\phi)}{2}$$

and plotted in Fig. 6.12. In Fig. 6.12 (a), we have plotted the transport current

of the upper arm ( $I_U^{even}$ ) as a function of flux and in Fig. 6.12 (b), we have plotted transport current of the lower arm ( $I_L^{even}$ ) as a function of flux. Keeping the total ring length same we have taken four different choices of arm length ratio and in all four cases we have shown that the nature of the transport current (in terms of position of maximum and minimum) in both upper arm and lower arm remains the same that is independent of arm length ratio. In both these figures peak value, i.e.,  $I^{max}$  is obtained at  $\phi/\phi_0 = 6.2$ . In Fig. 6.12 (a), with the increasing value of the upper arm length the  $I_U^{max}$  value decreases and in Fig. 6.12 (b), with the decreasing value of the lower arm length the  $I_L^{max}$  value increases.

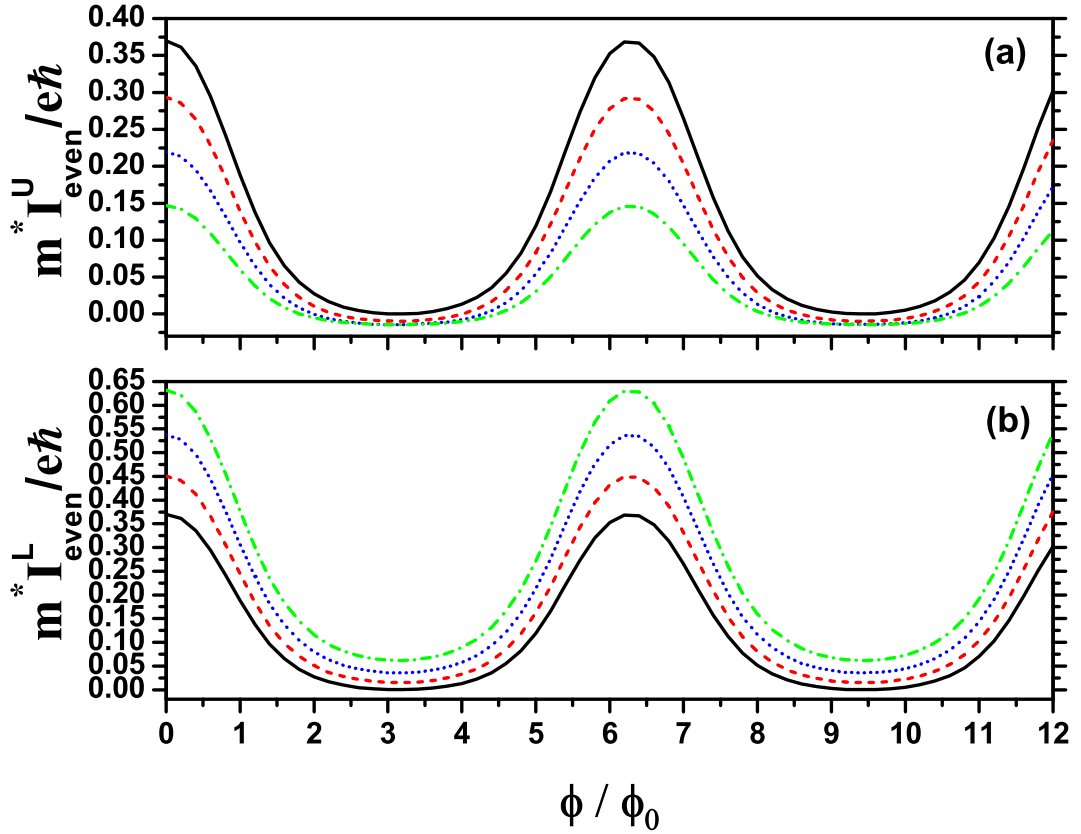


Figure 6.12: The figures (a) - (b) show plots of transport current  $I_{U/L}^{even}$  in dimensionless unit as a function of  $\phi/\phi_0$  for different arm lengths keeping the ring length same. In (a) and (b), the solid line is for arm length values of  $l_U/a = 0.1, l_L/a = 0.1$ , the dashed line is for arm length values of  $l_U/a = 0.12, l_L/a = 0.08$ , the dotted line is for arm length values of  $l_U/a = 0.14, l_L/a = 0.06$ , and the dash-dotted line is for arm length values of  $l_U/a = 0.16, l_L/a = 0.04$ .

One would have thought that since the evanescent modes decay exponentially inside the barrier,  $I_{U/L}^{max}$  would have scaled exponentially with the length. But counterintuitively they scale linearly. The peak value ( $I_{U/L}^{max}$ ), obtained at  $\phi/\phi_0 = 6.2$ , is

plotted along the arm length in Fig. 6.13. The solid line indicates the peak values of the upper arm ( $I_U^{max}$ ) for different arm length and the dashed line indicates the peak values for the lower arm ( $I_L^{max}$ ). With increasing the upper arm length,  $I_U^{max}$  linearly decreases whereas  $I_L^{max}$  linearly increases. This phenomenon has been reported earlier for evanescent modes in one dimension. We find it to occur even in presence of multiple modes with mixing between the modes. Thus the upper arm and the lower arm behave as classical Ohmic conductors. This is the reason why magnetization curves are so uniform and peak magnetization is always at  $\phi/\phi_0 = 6.2$  in Fig. 6.12. However, the sheer quantum behavior can be seen from the fact that the  $I_U.l_U + I_L.l_L \neq 0$ . For a classical Ohmic resistor doubling of length would have halved the current that helps in defining a material specific resistivity. Such a resistivity cannot be defined for evanescent modes.

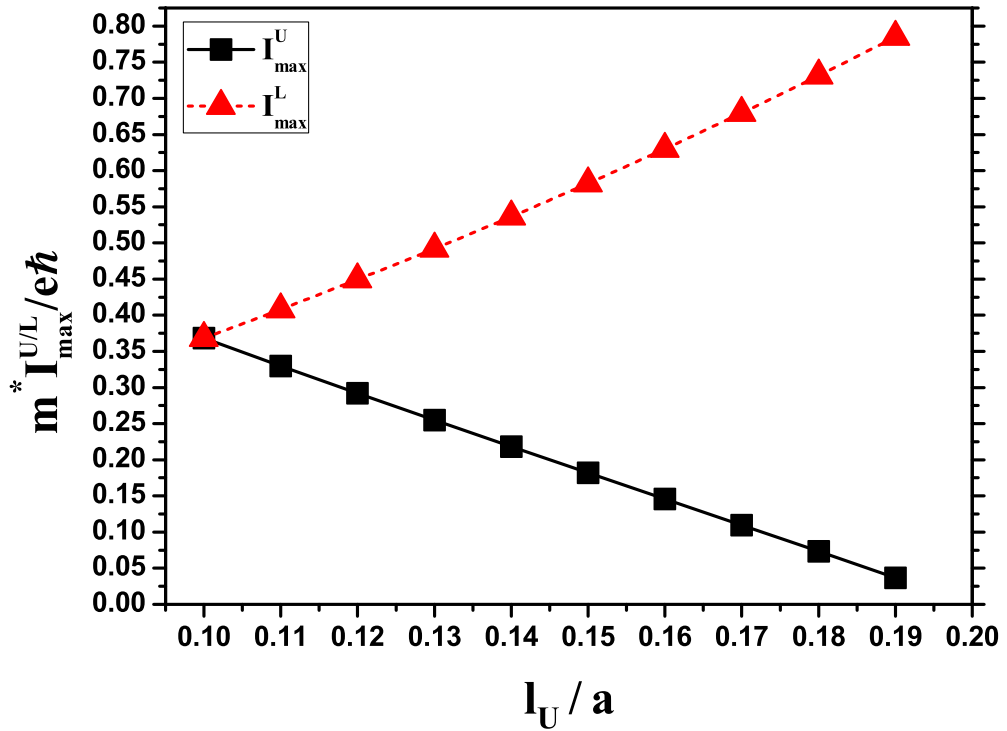


Figure 6.13: The figure shows plot of  $m^* I_{U/L}^{max} / e\hbar$  obtained at  $\phi/\phi_0 = 6.2$  (see Fig. 6.12) as a function of upper arm length ( $l_U/a$ ) of the quantum ring. The solid line indicates  $m^* I_U^{max} / e\hbar$  as a function of  $l_U/a$  and the dashed line indicates  $m^* I_L^{max} / e\hbar$  as a function of  $l_U/a$ .

The odd current is persistent current which is given by

$$I_{U,L}^{odd} = I_{U,L}(\phi) - I_{U,L}^{even}$$

and plotted as a function of  $\phi/\phi_0$  in Fig. 6.14. In Fig. 6.14 (a) and (b), we use the same convention and same parameters as in Fig. 6.12 (a) and (b), respectively. The Fig. 6.14 (a), shows the plot of persistent current as a function of  $\phi/\phi_0$  for the upper arm and Fig. 6.14 (b) shows the same for the lower arm. The nature of Fig. 6.14 (a) and (b) remains the same when we change the arm length ratio.

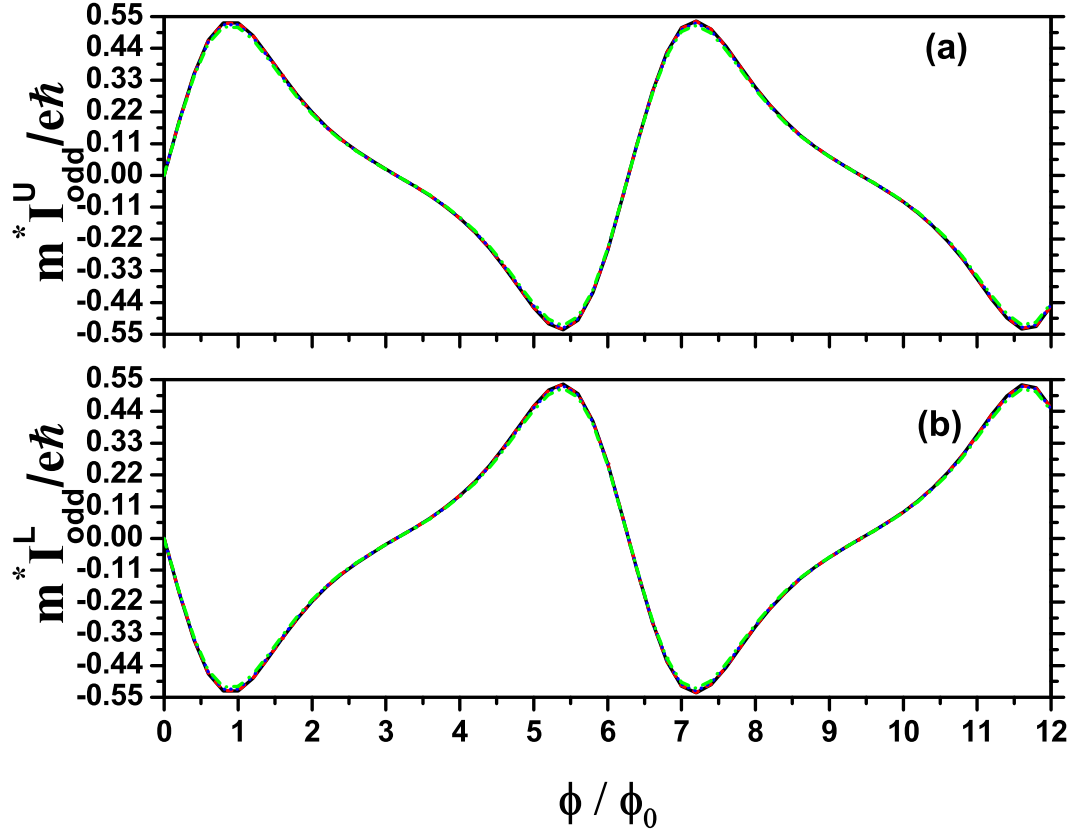


Figure 6.14: The figures (a) - (b) show plot of persistent current in dimensionless unit as a function of  $\phi/\phi_0$  for different arm lengths keeping the ring length same. In (a) and (b), we have used the same convention and same parameters as in Fig. 6.12 (a) and (b), respectively.

## 6.4 Conclusions

Although one-dimensional quantum rings coupled to reservoirs have received a lot of attention in the past, realistic multi-channel rings were never considered. We have considered such a quantum ring coupled to two reservoirs. We develop the formalism to include evanescent modes and channel mixing. A variety of quantum phenomena arise in such systems like persistent current, circulating current, Aharonov-Bohm

effect, conductance current etc. Therefore, we study all these quantum phenomena for realistic multi-channel rings. We have first calculated the conductance current taking two evanescent modes along the quantum ring. Here we have found that conductance current is qualitatively as well as quantitatively same for all variations of arm length ratio. Next we have calculated the circulating current for two different cases. First we have taken two propagating modes along the quantum ring and then we have taken one propagating mode and one evanescent mode along the quantum ring. We cannot get circulating current using evanescent modes only. Next we have calculated magnetization of the quantum ring. Magnetization in quantum ring arise due to two reasons - first is due to transport current and second is due to Aharonov-Bohm flux. We have calculated strength of magnetization for three different cases - (i) taking two propagating modes, (ii) taking one propagating mode and one evanescent mode and (iii) taking two evanescent modes. For the first two cases we have shown that magnetization behavior is not uniform for different parameters like ring length, arm length, Fermi energy etc. We have shown that for evanescent modes the strength of magnetization ( $I_U.l_U + I_L.l_L$ ) as a function of  $\phi/\phi_0$  is qualitatively as well as quantitatively same for all variations in parameters like different ratio of arm lengths, different Fermi energy, different total ring length etc. So there is possibility of robust device action based on magnetic response using only evanescent mode which contradicts earlier claims that devices based on quantum interference effects cannot be stabilized.

## Chapter 7

# CONCLUSIONS AND FUTURE PLAN

*“If I can stop one heart from breaking,  
I shall not live in vain;  
If I can ease one life the aching,  
or cool one pain,  
or help one fainting robin  
onto his nest  
I shall not live in vain.”*  
– Emily Dickinson.

Mesoscopic systems become essential to explore the transition between classical physics and quantum physics for last several decades. In the mesoscopic regime, many interesting and sometimes unexpected effects appear due to the phase coherence of the electronic wavefunctions. Some of these effects are very promising for applications in nano-electronic devices or for quantum standards in metrology.

In this thesis, the main objective was to study the thermodynamic properties of multiply connected geometries. We have studied transport property of a multi-channel Aharonov-Bohm ring. We have shown that the transport current can generate a magnetization which is seemingly a pure thermodynamic property of a system. Again we have studied quantum capacitance in terms of polarization which is a thermodynamic property of a system.

In Chapter 1, we started with the basic details of the mesoscopic systems. We have discussed the characteristic length scales, and have given the preliminary concept of two dimensional electron gas to fabricate mesoscopic samples. This section

is followed by some prominent mesoscopic effects.

In Chapter 2, we have given the detailed analysis of transport formalisms used in mesoscopic systems. We have shown that for an open mesoscopic conductor the system-environment (conductor-lead) coupling plays a very important role in its conductance phenomena. We have discussed in detail the Landauer-Büttiker formalism, landmark work by Raulf Landauer and M. Büttiker as this is very useful to calculate the conductance of a multi-channel Aharonov-Bohm ring in Chapter 5 and Chapter 6.

Aharonov-Bohm effect plays a very significant role in mesoscopic physics essentially because interference effects play a very crucial role there. The Aharonov-Bohm effect [12, 13] provides a mechanism for tuning the phase of an electron wave by means of an electric or magnetic field and controls the switching action of several proposed quantum interference devices. In Chapter 3 we have given a thorough theoretical analysis of Aharonov-Bohm effect in one-dimension for both open system as well as isolated system as this is indeed very useful to analyze the multi-channel rings in Chapter 5 and Chapter 6.

In Chapter 4, we have discussed how to define the quantum capacitance microscopically. We have shown that in the semi-classical regime there is a linear relation between polarization charge and induced potential of a mesoscopic isolated sample which are related by an effective capacitance  $C_{eff}$ . Effective capacitance can be decoupled as a linear combination of classical capacitance and quantum capacitance. The quantum capacitance is given by the Lindhard function. In this regime, we can design quantum circuits in terms of this parameter  $C_{eff}$  just as classical circuits are built in terms of parameters like resistance, capacitance and inductance. We have also shown that our analysis is independent of model and geometry in any dimension.

In Chapter 5, we have studied conductance, transport property of mesoscopic system using a two channel (transverse modes) Aharonov-Bohm ring. We have considered first both the channels to be propagating and we have shown that for different material parameters such as the total ring length, relative ratio of arm lengths, Fermi energy etc., the behavior of the conductance as a function of flux  $\phi/\phi_0$  becomes diverse in nature in different cases. We have shown that similar situation arises if we take one propagating mode and one evanescent mode. From this we have concluded that stable devices can be made neither by using two propagating modes nor by using one propagating mode and one evanescent mode. Such diverse behavior supports Landauer's claim that switch action based on quantum interference principle are not stable and practical. Finally we have considered both

the modes to be evanescent along the Aharonov-Bohm ring. Here we have found that conductance is qualitatively as well as quantitatively same for all variations in material parameters like total ring length, relative ratio of arm lengths, Fermi energy etc. Conductance being a symmetric function of flux is a function of  $\cos(n\phi/\phi_0)$ . Therefore within a period (0 to  $2\pi$ ) conductance is maximum at zero flux, then it goes through a deep minimum and rise again to a maximum value. We can assign the conductance maximum as ‘on’ state and conductance minimum as ‘off’ state of a switch signifying 1 and 0 operation in Boolean algebra. Thus we can conclude that if we employ evanescent modes only, we may be able to build stable, efficient and robust quantum switches. We can obtain appreciable changes in conductance when using evanescent modes. Different channels add up coherently and so by using larger and larger number of evanescent channels we can enhance the percentage drop in conductance and hence efficiency of the switch. In an experimental situation in a device where one has to employ many switches and can also require that one switch is ‘on’ while an adjacent switch is ‘off’ can be achieved by intelligently designing the lengths of the rings so that their areas are different and they capture different amounts of flux.

In Chapter 6, we have considered a multi-channel Aharonov - Bohm ring connected to two electron reservoirs via perfect leads. A variety of quantum phenomena can arise in such system, viz., Aharonov-Bohm effect, conductance current, circulating current, persistent current etc. We have studied all these phenomena for our multi-channel ring. We have developed a correct formalism to calculate the current in this system using two propagating modes, one propagating mode and one evanescent mode and two evanescent modes. We have studied conductance current using Landauer’s conductance formula for system having evanescent modes only. Next we have calculated circulating current for the system having propagating modes only and having one propagating mode and one evanescent mode. Circulating current can not arise for those systems having evanescent modes only. Then we have calculated the magnetization strength. This magnetization can arise due to two different reasons: firstly due to transport current inside the ring which can be present even in absence of Aharonov-Bohm flux and secondly due to Aharonov-Bohm flux which can be present even in absence of transport current. We have studied magnetization strength as a function of Fermi energy as well as flux ( $\phi/\phi_0$ ). In the regime of circulating current, both the upper arm current and the lower arm current in the multichannel ring flows either in the clockwise direction or flows in the anti-clockwise direction leading to a huge enhancement in the magnetization which we have shown. We have calculated strength of magnetization for three different cases - (i) taking two propagating modes, (ii) taking one propagating mode and one evanescent mode and (iii) taking two evanescent modes. We have plotted magnetization strength as

a function of flux,  $\phi/\phi_0$ . For the first two cases we have shown that magnetization behavior is not uniform for different parameters like ring length, arm length, Fermi energy etc. We have shown that for evanescent modes the strength of magnetization ( $I_U.l_U + I_L.l_L$ ) as a function of  $\phi/\phi_0$  is qualitatively as well as quantitatively same for all variations in parameters like different ratio of arm lengths, different Fermi energy, different total ring length etc. So there is possibility of robust device action based on magnetic response using only evanescent mode which contradicts earlier claims that devices based on quantum interference effects cannot be stabilized.

In future we will study the effect of Coulomb interactions in Aharonov-Bohm effect. We have shown how to derive quantum capacitance microscopically for a closed systems. Our next goal is to derive quantum capacitance for open systems also. We will also study quantum inductance.

# Bibliography

- [1] Feynman, R. P. *There's plenty of room at the bottom*, American Physical Society Meeting at Caltech, (<http://www.its.caltech.edu/feynman>) (1960).
- [2] Brattain, W., Schokley, W. and Bardeen, J. Nobel Lecture (1956).
- [3] Moore, Gordon E. Cramming more components onto integrated circuits. (<http://www.cs.utexas.edu/~fussel/courses/cs352h/papers/moore.pdf>) *Electronics Magazine*, 4 (1965), Retrieved 2006.
- [4] Moore, Gordon E. Excerpts from a conversation with Gordon Moore: Moore's law, (<http://large.stanford.edu/courses/2012/ph250/lee1/docs/Moore.pdf>) *Intel Corporation* 1, (2005). Retrieved 2013.
- [5] Murayama, Y. *Mesoscopic Systems: Fundamentals and Applications*. Wiley - VCH (2001).
- [6] Datta, S. *Electronic Transport in Mesoscopic Systems*. Cambridge: Cambridge University Press (1995).
- [7] Schöll, Eckehard. *Theory of Transport Properties of Semiconductor Nanostructures*. Chapman and Hall, First Edition, Springer (1998).
- [8] Drummond, T. J., Masselink, W. T. and Morkoc, H. Modulation-doped GaAs/(Al,Ga)As heterojunction field-effect transistors: MODFET's'. *Proc. IEEE* **74**, 773-822 (1986).
- [9] Melloch, M. R. Molecular beam epitaxy for high electron mobility modulation-doped two-dimensional electron gases. *Thin Solid Films* **231**, 74-85 (1993).
- [10] Ando, T., Fowler, A. B. and Stern, F. Electronic properties of two-dimensional systems. *Rev. Mod. Phys.* **54**, 437-672 (1982).
- [11] Washburn, S. and Webb, R. A. Aharonov-Bohm effect in normal metal quantum coherence and transport. *Adv. Phys.* **35**, 375-422 (1986).
- [12] Aharonov, Y. and Bohm, D. Significance of electromagnetic potentials in the quantum theory. *Phys. Rev.* **115**, 485-491 (1959).

- [13] Aharonov, Y. and Bohm, D. Further considerations on electromagnetic potentials in the quantum theory. *Phys. Rev.* **123**, 1511-1524 (1961).
- [14] Büttiker, M., Imry, Y. and Landauer, R. Josephson behavior in small normal one-dimensional rings. *Phys. Lett.* **96A**, 365-367 (1983).
- [15] Hall, E. H. On a new action of the magnet on electric currents. *Am. J. Math* **2**, 287-292 (1879).
- [16] Huang Kerson. *Statistical Mechanics*. Second Edition, Wiley-India (2003).
- [17] Ashcroft, N. W. and Mermin, N. D. *Solid State Physics*. India Edition, Brooks/Cole (2009).
- [18] Klitzing, von K., Droda, G. and Pepper, M. New method for high-accuracy determination of the fine-structure constant based on quantized Hall resistance. *Phys. Rev. Lett.* **45**, 494-497 (1980).
- [19] Tsui, D. C., Störmer, H. L. and Gossard, A. C. Two-dimensional magneto-transport in the extreme quantum limit. *Phys. Rev. Lett.* **48**, 1559-1562 (1982).
- [20] Laughlin, R. B. Anomalous quantum Hall effect: An incompressible quantum fluid with fractionally charged excitations. *Phys. Rev. Lett.* **50**, 1395-1398, (1983).
- [21] Saminadayar, L. Glattli, D. C, Jin, Y., and Etienne, B. Observation of the  $e/3$  fractionally charged Laughlin quasiparticle. *Phys. Rev. Lett.* **79**, 2526-2529, (1997).
- [22] Lee, P. A., Stone, Douglas A., and Fukuyama, H. Universal conductance fluctuations in metals: Effects of finite temperature, interactions and magnetic field. *Phys. Rev. B* **35**, 1039-1070 (1987).
- [23] Fowler, A. B., Hartstein, A., and Webb, R. A. Conductance in restricted-dimensionality accumulation layers. *Phys. Rev. Lett.* **48**, 196-199 (1982).
- [24] van Wees, B. J., van Houten, H., Beenakker, C. W. J., Williamson, J. G., Kouwenhoven, L. P., van der Marel, D., and Foxon, C. T. Quantized conductance of point contacts in a two-dimensional electron gas. *Phys. Rev. Lett.* **60**, 848-850 (1988).
- [25] Imry, Y. Active transmission channels and universal conductance fluctuations. *Europhys. Lett.* **1**, 249-256 (1986).
- [26] Houten, Henk van, and Beenakker, C. Quantum point contacts. *Phys. Today* **49**, 22-27 (1996).

- [27] Wharam, D. A., Thornton, T. J., Newbury, R., Pepper, M., Ahmed, H., Frost, J. E., Hasko, D. G., Peacock, D. C., Ritchie, D. A. and Jones, G. A. C. One-dimensional transport and the quantization of ballistic resistance. *J. Phys. C* **21**, L209-L214 (1988).
- [28] Webb, Richard A., and Wahburn, S. Quantum interference fluctuations in disordered metals. *Phys. Today* **41**, 46-53 (1988).
- [29] Onsager, L. Reciprocal relations in irreversible processes. I. *Phys. Rev.* **37**, 405-426 (1931); Reciprocal relations in irreversible processes. II. *Phys. Rev.* **38**, 2265-2279 (1931).
- [30] Büttiker, M. Four-terminal phase-coherent conductance. *Phys. Rev. Lett.* **57**, 1761-1764 (1986).
- [31] London, F. *J. Phys. (France)*, **8**, 379 (1937).
- [32] Hund, F. *Ann. Phys. (Leipzig)* **32**, 102 (1938).
- [33] Bloch, F. Off-diagonal long-range order and persistent currents in a hollow cylinder. *Phys. Rev.* **137**, A 787-A 795 (1965).
- [34] Kulik, I. O. Magnetic flux quantization in normal state. *JETP* **31**, 1172-1174 (1970).
- [35] Lévy, L. P., Dolan, G., Dunsmuir, J., and Bouchiat, H. Magnetization of a mesoscopic copper rings: Evidence for persistent currents. *Phys. Rev. Lett.* **64**, 2074-2077 (1990).
- [36] Chandrasekhar, V., Webb, R. A., Brady, M. J., Ketchen, M. B., Gallagher, W. J., and Kleinsasser, A. Magnetic response of a single isolated gold loop. *Phys. Rev. Lett.* **67**, 3578-3581 (1991).
- [37] Mailly, D., Chapelier, C., and Benoit, A. Experimental observation of persistent currents in a GaAs-AlGaAs single loop. *Phys. Rev. Lett.* **70**, 2020-2024 (1993).
- [38] Frenkel, J. On the electrical resistance of contacts between solid conductors. *Phys. Rev.* **36**, 1604-1618 (1930).
- [39] Landauer, R. Spatial variation of currents and fields due to localized scatterers in metallic conduction. *IBM J. Res. Dev.* **32**, 223-231 (1957).
- [40] Landauer, R. Conductance from transmission: common sense points. *Physica Scripta* **T42**, 110-114 (1992).

- [41] Imry, Y. *Physics of Mesoscopic Systems* in Directions in Condensed Matter Physics, eds. G. Grinstein and G. Mazenko. World Scientific Press, Singapore (1986).
- [42] Engquist, H. L. and Anderson, P. W. Definition and measurement of the electrical and thermal resistances. *Phys. Rev. B* **24**, 1151-1154 (1981).
- [43] Büttiker, M. Symmetry of electrical conduction. *IBM J. Res. Dev.* **32**, 317-334 (1988).
- [44] Büttiker, M. Voltage fluctuations in small conductors. *Phys. Rev. B* **35**, 4123-4126 (1987).
- [45] Büttiker, M. Negative resistance fluctuations at resistance minima in narrow quantum Hall conductors. *Phys. Rev. B* **38**, 12 724-12 727 (1988).
- [46] Xia, Jian-Bai. Quantum waveguide theory for mesoscopic structures. *Phys. Rev. B* **45**, 3593-3599 (1992).
- [47] Swanson, D. G. *Quantum Mechanics: Fundamentals and Applications*. Taylor and Francis, New York (2007).
- [48] Washburn, S., Schmid, H., Kern, D., and Webb, R. A. Normal-metal Aharonov-Bohm effect in the presence of a transverse electric field. *Phys. Rev. Lett.* **59**, 1791-1795 (1987).
- [49] Timp, G., Chang, A. M., Cunningham, J. E., Chang, T. Y., Mankiewich, P., Behringer, R., and Howard, R. E. Observation of the Aharonov-Bohm effect for  $\omega\tau > 1$ . *Phys. Rev. Lett.* **58**, 2814-2818 (1987).
- [50] Chang, A. M., Owusu-Sekyere, K., and Chang, T. Y. Observation of phase-shift locking of the Aharonov-Bohm effect in doubly connected  $GaAs - Al_xGa_{1-x}As$  heterostructure devices. *Solid State Comm.* **67**, 1027-1030 (1988).
- [51] Chang, A. M., Timp, G., Cunningham, J. E., Mankiewich, P. M., Behringer, R. E., Howard, R. E., and Baranger, H. U. Real-space and magnetic-field correlation of quantum resistance fluctuations in the ballistic regime in narrow  $GaAs - Al_xGa_{1-x}As$  wires. *Phys. Rev. B* **37**, 2745-2748 (1988).
- [52] Timp, G., Mankiewich, P. M., deVegvar, P., Behringer, R. E., Cunningham, J. E., Howard, R. E., and Baranger, H. U. Suppression of the Aharonov-Bohm effect in the quantized Hall regime. *Phys. Rev. B* **39**, 6227-6230 (1989).
- [53] Ford, C. J. B., Thornton, T. J., Newbury, R., Pepper, M., Ahmed, H., Foxon, C. T., Harris, J. J., and Roberts, C. The Aharonov-Bohm effect in electrostatically defined heterojunction rings. *J. Phys. C* **21**, L325-L331 (1988).

- [54] Cheung, H. F., Gefen, Y. and Reidel, E. Isolated rings of mesoscopic dimensions. Quantum coherence and persistent currents. *IBM J. Res. Dev.* **32**, 359-371 (1988).
- [55] Byers, N., and Yang, C. N. Theoretical considerations concerning quantized magnetic flux in superconducting cylinders. *Phys. Rev. Lett.* **7**, 46-49 (1961).
- [56] Bloch, F., Flux quantization and dimensionality. *Phys. Rev.* **166**, 415-423 (1968).
- [57] Das, M. P. and Green, F. Mesoscopic transport revisited. *J. Phys.: Cond. Matt.* **21**, 1-5 (2009).
- [58] Gabelli, J., Berroir, J. M., Fève, G., Placais, B., Jin, Y., Etienne, B. and Glattli, D. C. Violation of Kirchhoff's laws for a coherent RC circuit. *Science* **313**, 499-502 (2006).
- [59] Fève, G., Berroir, J. M., Kontos, T., Placais, B., Glattli, D. C., Cavanna, A., Etienne, B., Jin, Y. An on-demand coherent single electron source. *Science* **316**, 1169-1172 (2007).
- [60] Kataoka, M., Schneble, R. J., Thorn, A. L., Barnes, C. H. W., Ford, C. J. B., Anderson, D., G. A. C. Jones, I. Farrer, Ritchie, D. A. and Pepper, M. Single-electron population and depopulation of an isolated quantum dot using a surface-acoustic-wave pulse. *Phys. Rev. Lett.* **98**, 046801, 1-4 (2007).
- [61] Blumenthal, M. D., Kaestner, B., Li, L., Giblin, S., Janssen, T. J. B. M., Pepper, M., Anderson, D., Jones, G., and Ritchie, D. A. Gigahertz quantized charge pumping. *Nature Phys.* **3**, 343-347 (2007).
- [62] Kaestner, B., Kashcheyevs, V., Amakawa, S., Li, L., Blumenthal, M. D., Janssen, T. J. B. M., Hein, G., Pierz, K., Weimann, T., Siegner, U. and Schumacher, H. W. Single-parameter non-adiabatic quantized charge pumping. arXiv:0707.0993 [cond-mat.mes-hall]/ 1-4 (2007).
- [63] Nigg, S. E. and Büttiker, M. Quantum to classical transition of the charge relaxation resistance of a mesoscopic capacitor. *Phys. Rev. B* **77**, 085312, 1-4 (2008).
- [64] Moskalets, M., Samuelsson, P. and Büttiker, M. Quantized dynamics of a coherent capacitor. *Phys. Rev. Lett.* **100**, 086601, 1-4 (2008).
- [65] Moskalets, M. and Büttiker, M. Heat production and current noise for single- and double-cavity quantum capacitors. *Phys. Rev. B* **80**, 081302, 1-4 (2009).

- [66] Nigg, S. E. and Büttiker, M. Universal detector efficiency of a mesoscopic capacitor. *Phys. Rev. Lett.* **102**, 236801, 1-4 (2009).
- [67] Nigg, S. E., Lopez, R. and Büttiker, M. Mesoscopic charge relaxation. *Phys. Rev. Lett.* **97**, 206804, 1-4 (2006).
- [68] Büttiker, M. and Nigg, S. E. Mesoscopic capacitance oscillations. *Nanotechnology* **18**, 044029, 1-5 (2007).
- [69] Büttiker, M. Characteristic potentials for mesoscopic rings threaded by an Aharonov-Bohm flux. *Physica Scripta* **T54**, 104-110 (1994).
- [70] Büttiker, M. Capacitance, admittance, and rectification properties of small conductors. *J. Phys.: Cond. Matt.* **5**, 9361-9377 (1993).
- [71] Shylau, A. A., Klos, J. W., and Zozoulenko, I. V. Capacitance of graphene nanoribbons. *Phys. Rev. B* **80**, 205402, 1-9 (2009).
- [72] Büttiker, M., Polianski, M. L. Charge fluctuations in open chaotic cavities. *J. Phys. A* **38**, 10559-10585 (2005).
- [73] Büttiker, M. Small normal-metal loop coupled to an electron reservoir. *Phys. Rev. B* **32**, 1846-1849 (1985).
- [74] Hohenberg, P. and Kohn, W. Inhomogeneous electron gas. *Phys. Rev.* **136**, B864-B871 (1964).
- [75] See for example Eq. (5) in Büttiker, M. Time in quantum mechanics. Muga, J. G., Sala Mayato, R., Egusquiza, I. L. (Eds.), Lecture Note in Physics, Springer, Berlin (2002).
- [76] Büttiker, M., Charge densities and charge noise in mesoscopic conductors. *Pramana Journal of Physics* **58**, 241-257 (2002).
- [77] Reimann, S. M., Koskinen, M., Manninen, M., Mottelson, B. R. Quantum dots in magnetic fields: phase diagram and broken symmetry at the maximum-density-droplet edge. *Phys. Rev. Lett.* **83**, 3270-3273 (1999).
- [78] Chakraborty, T., Pietilainen, P. Persistent currents in quantum ring: Effects of impurities and interactions. *Phys. Rev. B* **52**, 1932-1935 (1995).
- [79] Wu, H., Sprung, D. W. L. and Martorell, J. Effective one-dimensional square well for two dimensional quantum wires. *Phys. Rev. B* **45**, 11960-11967 (1992).
- [80] Guinea, F. and Verges, J. A. Localization and topological disorder. *Phys. Rev. B* **35**, 979-986 (1987).

- [81] Luryi, S. Quantum capacitance devices. *Appl. Phys. Lett.* **52**, 501-503 (1988).
- [82] Datta, S., Melloch, M. R., Bandyopadhyay, S., Noren, R., Vaziri, M., Miller, M. and Reifenberger, R. Novel interference effects between parallel quantum wells. *Phys. Rev. Lett.* **55**, 2344-2347 (1985).
- [83] Datta, S., Melloch, M. R., Bandyopadhyay, S. and Lundstrom, M. S. Proposed structure for large quantum interference effects. *Appl. Phys. Lett.* **48**, 487-489 (1986).
- [84] Datta, S. and Das, B. Electronic analog of the electrooptic modulator. *Appl. Phys. Lett.* **56**, 665-667 (1990).
- [85] Datta, S. and McLennan, M. J. Quantum transport in ultra small electronic devices. *Rep. Prog. Phys.* **53**, 1003-1048 (1990).
- [86] Sols, F., Macucci, M., Ravoili, V. and Hess, K. On the possibility of transistor action based on quantum interference phenomena. *Appl. Phys. Lett.* **54**, 350-352 (1989); also *Proceedings of the International Symposium on Nanostructure Physics and Fabrication*, College Station, Texas, March 13-15, 1989, edited by Reed, M. A. and Kirk, W. P. (Academic, New York, 1989), p.157; Fowler, A. B. Workshop on Quantum Interference, Atlanta (1988).
- [87] Sols, F., Macucci, M., Ravoili, V. and Hess, K. Theory for a quantum modulated transistor. *J. Appl. Phys.* **66**, 3892-3906 (1989).
- [88] Subramaniam, S., Bandyopadhyay, S., and Porod, W. Analysis of the device performance of quantum interference transistors utilizing ultrasmall semiconductor T structures. *J. Appl. Phys.* **68**, 4861-4870 (1990).
- [89] Landauer, R. Can we switch by control of quantum mechanical transmission? *Physics Today* **42**, 119-121 (1989).
- [90] Gupta, B. C., Deo, P. S. and Jayannavar, A. M. Aharonov-Bohm effect in the presence of evanescent modes. *Int. J. Mod. Phys. B* **10**, 3595-3608 (1996).
- [91] Jayannavar, A. M. and Deo, P. S. Novel interference effects in multiply connected normal metal rings, *Mod. Phys. Lett. B* **8**, 301-310 (1994).
- [92] Molnár, B., Peeters, F. M., and Vasilopoulos, P. Spin dependent magnetotransport through a ring due to spin-orbit interaction. *Phys. Rev. B* **69**, 155335, 1-11 (2004).
- [93] Molnár, B., Vasilopoulos, P., and Peeters, F. M. Spin-dependent transmission through a chain of rings: Influence of a periodically modulated spin-orbit interaction strength or ring radius. *Appl. Phys. Lett.* **85**, 4 (2004).

- [94] Földi, P., Molnár, O., Benedict, M. G., and Peeters, F. M. Spintronic single-qubit gate based on a quantum ring with spin-orbit interaction. *Phys. Rev. B* **71**, 033309, 1-4 (2005).
- [95] Molnár, B., Vasilopoulos, P. and Peeters, F. M. Magnetoconductance through a chain of rings with or without periodically modulated spin-orbit interaction strength and magnetic field. *Phys. Rev. B* **72**, 075330, 1-7 (2005).
- [96] Földi, P., Kálmán, O., Benedict, M. G., and Peeters, F. M., Quantum rings as electron spin beam splitters, *Phys. Rev. B* **73**, 155325, 1-5 (2006).
- [97] Vasilopoulos, P., Kálmán, O., Peeters, F. M., and Benedict, M. G. Aharonov-Bohm oscillations in mesoscopic ring with asymmetric arm-dependent injection. *Phys. Rev. B* **75**, 035304, 1-7 (2007).
- [98] Kálmán, O., Földi, P., Benedict, M. G. and Peeters, F. M. Spatial interference induced spin polarization in a three-terminal quantum ring. *Physica E* **40**, 567-573 (2008).
- [99] Joshi, S. K., Sahoo, D. and Jayannavar, A. M. Aharonov-Bohm oscillations and spin-polarized transport in a mesoscopic ring with a magnetic impurity. *Phys. Rev. B* **64**, 075320, 1-6 (2001).
- [100] Benjamin, C. and Jayannavar, A. M. Study of quantum current enhancement, eigenenergy spectra and magnetic moments in a multiply connected system at equilibrium. *Int. J. Mod. Phys. B* **16**, 1787-1805 (2002).
- [101] Chowdhury, Sengupta. S., Deo, P. S., Roy, A. K. and Manninen, M. Large diamagnetic persistent currents. *New Journal of Physics* **10**, 083014, 1-12 (2008).
- [102] Sharvin, D. Yu. and Sharvin, Yu. V. Magnetic-flux quantization in a cylindrical film of a normal metal. *JETP Lett.* **34**, 272-275 (1981).
- [103] Büttiker, M., Imry, Y., Landauer, R. and Pinhas, S. Generalized many-channel conductance formula with application to small rings. *Phys. Rev. B* **31**, 6207-6215 (1985).
- [104] Griffith, J. S., A free-electron theory of conjugated molecules. *Trans. Faraday Soc.* **49**, 345-351 (1953).
- [105] Bagwell, Philip F. Evanescent modes and scattering in quasi-one-dimensional wires. *Phys. Rev. B* **41**, 10 354-10 371 (1990).
- [106] Merzbacher, E. *Quantum Mechanics*. Third Edition., Wiley, New York (1997).

- [107] Pastawski, H. M., Rojo, A. and Balseiro, C. Quantum origin of half-flux oscillations in the magnetoresistance of metal cylinders. *Phys. Rev. B* **37**, 6246-6250 (1988).
- [108] *Mesoscopic Phenomena in Solids*, edited by Al'tshuler, B. L., Webb, R. A. and Lee, P. A. , Elsevier, Amsterdam (1991).
- [109] Popovic, R. S., Flanagan, J. A., Besse, P. A. The future of magnetic sensors. *Sensors and Actuators A* **56**, 39-55 (1995).
- [110] Lenz, James E. A review of magnetic sensors. *Proc. IEEE* **78**, 973-989 (1990).
- [111] Akkermans, E., Aurbach, A., Avron, J. E., and Shapiro, B. Relation between persistent currents and the scattering matrix. *Phys. Rev. Lett* **66**, 76-79 (1991).
- [112] Mukherjee, S., Yadav, A. and Deo, P. S. Stable switch action based on quantum interference effect. *Physica E* **47**, 86-94 (2013).
- [113] Mukherjee, S. and Deo, P. S. Evanescent mode transport and its application to nanoelectronics. *AIP Conf. Proc.* **1512**, 944-945 (2013).
- [114] J. D. Jackson, *Classical Electrodynamics*. Third Edition, Wiley, New York (1997).
- [115] Büttiker M., in *Squid '85 - Superconducting Quantum Interference Devices and Their Application*, edited by H. D. Hahlbohm and H. Lüebbig, de Gruyter, Berlin (1985).
- [116] Jayannavar, A. M., and Deo, P. S. Persistent currents in presence of transport current. *Phys. Rev. B* **51**, 10 175-10 178 (1995).
- [117] Shaw, D. F, *An Introduction to Electronics*. Second Edition, Longman, London (1970), p.51.
- [118] Jayannavar, A. M., Deo, P. S., and Pareek, T. P. Current magnification and circulating current in mesoscopic rings. *Physica B* **212**, 261-266 (1995).
- [119] Cho, S. Y., Choi, T. and Ryu, C-M. Quantum transport in mesoscopic rings with stubs. *Int. J. Mod. Phys. B* **10**, 3569-3581 (1996).
- [120] Pareek, T. P., Deo, P. S. and Jayannavar, A. M. Effect of impurities on the current magnification in mesoscopic open rings. *Phys. Rev. B* **52**, 14 657 - 14 663 (1995).

- [121] Vargiamidis, V. and Polatoglou, H. M. Fano resonance and persistent current in mesoscopic open rings: Influence of coupling and Aharonov-Bohm flux. *Phys. Rev. B* **74**, 235323, 1-14 (2006).
- [122] Benjamin, C. and Jayannavar, A. M. Features in evanescent Aharonov-Bohm interferometry. *Phys. Rev. B* **68**, 085325, 1-6 (2003).
- [123] Bandopadhyay, S., Deo, P. S and Jayannavar, A. M. Quantum current magnification in a multichannel mesoscopic ring. *Phys. Rev. B* **70**, 075315, 1-9 (2004).
- [124] Yi, J., Wei, J. H., Hong, J., and Lee, S-I. Giant persistent currents in the open Aharonov-Bohm rings. *Phys. Rev. B* **65**, 033305, 1-4 (2001).
- [125] Park, W. and Hong, J. Analysis of coherent current flows in the multiply connected open Aharonov-Bohm rings. *Phys. Rev. B* **69**, 035319, 1-7 (2004).
- [126] Cho, S. Y., McKenzie, R. H., Kang, K., and Kim, C. K. Magnetic polarization currents in double quantum dot devices. *J. Phys.: Cond. Matt.* **15**, 1147-1154 (2003).
- [127] Cho, S. Y., and McKenzie, R. H. Thermal and electrical currents in nanoscale electronic interferometers. *Phys. Rev. B* **71**, 045317, 1-6 (2005).
- [128] Wu, H.-C., Guo, Y., Chen, X.-Y. and Gu, B.-L. Giant persistent current in a quantum ring with multiple arms. *Phys. Rev. B* **68**, 125330, 1-5 (2003).
- [129] Zhang, Y.-T., Guo, Y. and Li, Y.-C. Persistent spin currents in a quantum ring with multiple arms in the presence of spin-orbit interaction. *Phys. Rev. B* **72**, 125334, 1-6 (2005).
- [130] Choi, T., Ryu, C-M., and Jayannavar, A. M. Directional dependence of spin currents induced by Aharonov-Casher phase. *Int. J. Mod. Phys. B* **12**, 2091-2102 (1998).
- [131] Citro, R. and Romeo, F. Persistent spin and charge currents and magnification effects in open ring conductors subject to Rashba coupling. *Phys. Rev. B* **75** 073306, 1-4 (2007).
- [132] Su, Y. H., Cho, S. Y., Chen, A. M., and Choi, T. Is the Fano antiresonance a necessary requirement for circulating currents in mesoscopic interferometers? *J. Korean Phys. Soc.* **57**, 138-143 (2010).
- [133] Takai, D. and Ohta, K. Quantum oscillation in multiply connected mesoscopic rings at finite temperature. *Phys. Rev. B* **50**, 2685-2688 (1994).

- [134] Gefen, Y., Imry, Y. and Azbel, M. Ya. Quantum oscillations and the Aharonov-Bohm effect for parallel resistors. *Phys. Rev. Lett.* **52**, 129-132 (1984).